ABSTRACT

Title of Document: THE ROLE OF MECHANICAL MIXING IN THE FORMATION OF REACTION ZONES IN SUBDUCTION-RELATED MÉLANGE

Julia K. Gorman, Master of Science, 2013

Directed By: Assistant Professor Sarah Penniston-Dorland, Geology

Traverses across metamorphic reaction zones at contacts between mafic rocks and ultramafic mélange matrix were analyzed in two mélange zones (Catalina Schist, Santa Catalina Island, CA, and Attic-Cycladic Complex, Syros, Greece) in order to investigate a mechanically mixed contribution to subduction-related reaction zones. Elements enriched in peridotite relative to mafic crust such as Os, Ir, Ru, Ni and Cr were used to assess the addition of a peridotitic component to reaction zones. Results showed co-varying concentrations of Ni, Cr, Os, Ir, and Ru in reaction zones, suggesting these components were added via mixing with mantle peridotite. $^{187}Os/^{188}Os$ ratios were lower in reaction zones relative to block cores, consistent with the addition of peridotite to mafic rock. Reaction zone samples plot along mixing trends between peridotite and basalt, indicating that mechanical mixing, along with fluid-mediated mass transfer of fluid-mobile elements, contributes to reaction zone formation in the Catalina Schist mélange zone.

THE ROLE OF MECHANICAL MIXING IN THE FORMATION OF REACTION ZONES IN SUBDUCTION-RELATED MÉLANGE

By

Julia K. Gorman

Thesis submitted to the Faculty of the Graduate School of the
University of Maryland, College Park, in partial fulfillment
of the requirements for the degree of
Master of Science
2013

Advisory Committee:
Assistant Professor Sarah Penniston-Dorland, Chair
Professor Richard J. Walker
Senior Research Scientist Philip M. Piccoli

Acknowledgments

I would first and foremost like to thank my committee, Drs., Sarah Penniston-Dorland, Rich Walker, and Phil Piccoli. I would especially like to thank Dr. Penniston-Dorland for her continued support and guidance. I would like to thank Dr. Igor Puchtel for his assistance with clean lab chemistry. I would like to thank Richard Ash for his help with ICP-MS analysis. I thank Gray Bebout for his assistance in locating and collecting samples and his overall Santa Catalina expertise. Many thanks go to Horst Marschall for providing samples as well as sage advice. This study was funded by NSF grant Ear-1119111.

I would like to express my sincere gratitude to my fellow graduate students for their advice and for keeping me sane. I am also especially grateful to Natalie Sievers for her help collecting samples, as well as her invaluable insights. Last but not least, I would like to thank my family for their continued encouragement.

Table of Contents

List of Tables

List of Figures

Chapter 1: Introduction

1.1 Description of mélange zones

In subduction zones, crustal material is both recycled into the mantle by subduction of the down-going crustal slab as well as created at the Earth's surface through eruption of arc volcanoes. As an oceanic plate subducts, the suite of oceanic mantle lithosphere, gabbroic-basaltic oceanic crust, and crustal sediment is conveyed below the overlying plate. Material located at the contact of the two juxtaposed plates is heated and sheared. This intense shearing is thought to create mélange zones, i.e., zones of mixing between lithologies along the slab-mantle interface (Bebout and Barton, 2002). When these mélange zones are exhumed by faulting and exposed at the surface, they provide clues to the varied processes of metamorphism occurring at depth in subduction zones. Consequently, a number of studies have targeted mélange zones for direct examination of subduction processes.

Mélange zones have been well documented in subduction-related metamorphic complexes worldwide, e.g., Attic-Cycladic Complex, Syros Island, Greece (Okrusch and Bröcker,1990); Catalina Schist, Santa Catalina Island, CA, USA (Bebout and Barton, 1989; 2002); Franciscan Complex, CA (Moore, 1984); Samana Metamorphic Complex, Dominican Republic (Giaramita and Sorensen, 1994); Osayama Mélange, SW Japan (Tsujimori and Itaya, 1999); Chara Zone, NE Kazakhstan (Volkova et al., 2004); and the

Maksyutov Complex (upper unit), Russia (Beane and Liou, 2005). Lithologies in these mélange zones record temperatures of 400 to 800°C and 0.8 to 2.4 GPa. The mélange zones consist of blocks of metamorphosed mantle peridotite, basaltic crust, or sediment. These blocks are then often surrounded by cm- to m- scale chemically distinct reaction zones. The blocks and associated reaction zones are interspersed in a fine-grained matrix lithology, and exhibit varying metamorphic grades: eclogite, blueschist, lawsonite-eclogite, lawsonite-blueschist, lawsonite-albite, amphibolite, and greenschist. Blocks range in size from approximately 0.5 m to ~km-long Reaction zones commonly contain hydrated mineral assemblages. These include: chlorite (Chl) + actinolite (Act) + phengite (Phe), Chl + talc (Tlc), Act + Chl+ Tlc, Chl + tourmaline (Tur) + Na-rich omphacite (Omp), ± carbonate (mineral abbreviations from Kretz, 1983). The mélange matrix is serpentinite or metasediment.

In order to explore the complete subduction zone cycle, many studies have also investigated arc volcanic rocks. Arc volcanic rocks are thought to be related geochemically to both subducting material and the overlying mantle wedge. A recent geochemical review (Marschall and Schumacher, 2012) compared arc volcanic geochemistry to the geochemistry of rocks within mélange zones to show that mélange processes can produce variability in arc lavas. The authors suggest a three-component mixing model involving subducted sediments, subducting basaltic slab, and the ultramafic mantle wedge to explain geochemical signatures in arc lavas and mélange zone lithologies. However, the extent to which these three components mix, and the types and locations of mixing are still debated. Moreover, different elements may mix via

different or multiple processes. Through focused examination of reaction zones, this study investigates specifically the processes that may account for varying inputs of mantle peridotite to subduction-related reaction zones.

1.2 Proposed mechanisms for mass transfer in mélange zones

Three main mechanisms are thought to contribute to the formation of mélange-related metasomatic reaction zones. The first is mass transfer by infiltration of externally derived fluids. The second mechanism is mass transfer by diffusion through an intergranular fluid. The third mechanism proposed for reaction zone formation is the mechanical mixing of juxtaposed lithologies (e.g., mantle peridotite and basaltic slab).

Mass transfer of fluid-mobile elements by externally derived fluids may result in higher concentrations of fluid-mobile elements in reaction zones relative to adjacent serpentinites and metabasalts. Documented elevated contents of fluid-mobile elements such as Ba and K in reaction zones in the Catalina Schist suggest that metasomatizing fluids originated from a sedimentary source, as crustal sediments generally have much higher Ba and K contents (Sorensen and Grossman, 1989). Volcanic arc lavas are also enriched in elements such as Ba and K (e.g., Morris and Ryan, 2003; Plank and Langmuir, 1993), and therefore, are thought to be related to subducted slab material.

Secondly, elements may be transported by diffusion through an intergranular fluid at lithologic contacts, which can have steep concentration gradients across the contact. This has been documented on a small scale by δ^7Li trends across lithologic contacts in the Catalina Schist and Franciscan Complex (Penniston-Dorland et al., 2012a).

The mechanical mixing mechanism was first proposed to explain the formation of mélange matrix (Bebout and Barton, 2002), then subsequently to explain reaction zone formation in the Catalina Schist, Franciscan Complex, and Samana Metamorphic Complex (Penniston-Dorland et al., 2012b). Reaction zones analyzed in Penniston-Dorland et al. (2012b) have elevated HSE concentrations relative to adjacent block cores. Most previous studies on reaction zones have focused on studying fluid-mobile elements to assess the first and second mechanism discussed. This study utilizes the highly siderophile elements (HSE; Os, Ir, Ru, Pt, Pd, Re) to examine in greater detail the mechanical mixing components of reaction zones in two subduction-related mélange zones.

1.3 HSE and osmium isotopic studies

Osmium, Ir and Ru are strongly compatible during low extents of mantle melting. Therefore, mantle peridotites and serpentinites are enriched in these elements relative to bulk continental crust. Rhenium, and to a certain extent Pt and Pd, are incompatible during melting and, thus, have higher concentrations in crustal material relative to mantle material. Due to the order of magnitude concentration differences between HSE in subducted crust and mantle (e.g., Os concentrations in: basalt ~0.001 to 0.05 ppb, peridotite ~1 to 4 ppb; Shirey and Walker, 1998), concentrations of these elements should be useful for tracing mantle vs. crustal input in reaction zones. Additionally, the decay of ^{187}Re to ^{187}Os via β^- decay ($\lambda = 1.666 \times 10^{-11}$ yr^{-1}) causes considerable divergence in $^{187}Os/^{188}Os$ ratios in mantle vs. crustal rocks. Therefore, this ratio can be used as an additional tool to determine peridotitic additions to reaction zones.

Just as elevated Ba and K concentrations in arc lavas can be related to elevated Ba and K concentrations in reaction zones, multiple studies have used HSE concentrations and Os isotopic data in order to determine the extent of mantle metasomatism above subduction zones. For example, a study of Kamchatka arc mantle xenoliths by Widom et al. (2003) reports $^{187}Os/^{188}Os$ ratios from 0.1226 to 0.1566 compared to 0.1221 to 0.1276 for unaltered oceanic abyssal peridotites. Elevated ratios (relative to continental peridotites) are attributed to the influence of radiogenic, slab-derived fluids, thus, invoking mobility of Os by fluids. Alves et al. (1999) reports highly radiogenic arc lavas from Java ($^{187}Os/^{188}Os$ = 0.241 to 3.704) and low Os concentrations (0.00010 ppb to 0.017 ppb). Moreover, Alves et al. (2002) reports radiogenic arc lavas ($^{187}Os/^{188}Os$ = 0.130 to 1.524) from 10 subduction zones around the world. The authors suggest that these compositions are the result of mixing of the mantle with two distinct contaminating components from subducted materials with different Os isotopic compositions. In a study of calc-alkaline arc volcanic rocks from the Lassen region of the Cascade arc, Borg et al. (2000) reports Os isotopic ratios of 0.1285 to 0.2829. This study attributes these Os isotopic ratios to slab- component-enriched source magmas and to the retention of Os and Re in the mantle in sulfide phases.

Shirey and Walker (1998) and Brandon et al. (1996) suggest Os may be slightly incompatible during slab dehydration reactions causing the destabilization of Os-bearing sulfides. Currently there is little consensus on the mobility of Os and the stability of Os bearing phases at temperatures and pressures thought to exist at depth in subduction zones. However, previously reported HSE concentrations in reaction zones from three

subduction zone metamorphic complex localities (Penniston-Dorland et al., 2012b) suggests that transfer of HSE into reaction zones by a fluid would have to be pervasive and highly mobilizing. A more likely explanation may be a mechanically added component which alters the HSE content of the reaction zone followed by late-stage fluid infiltration. Comparing the results of previous HSE studies of mantle xenoliths and arc lavas to results from this study may help link reaction zone-forming processes at depth to arc lavas and xenoliths seen on Earth's surface.

Chapter 2: Geologic background

2.1 Catalina Schist, Santa Catalina Island, CA

The Catalina Schist is a subduction-related metamorphic complex exposed on Santa Catalina Island off the coast of Southern California (Fig. 1). The Catalina Schist is composed of lithologies representing a range of fault-bounded metamorphic facies, including, from structurally lowest to highest: lawsonite-albite, lawsonite-blueschist, epidote-blueschist, epidote-amphibolite and amphibolite facies. The metamorphism is thought to have occurred as the Farallon Plate subducted under the North American Plate. The age of peak amphibolite facies metamorphism is 114.5 ± 0.6 Ma (Anczkiewicz et. al., 2004) as determined using Lu-Hf dating techniques on garnets in garnet amphibolites. Results from Grove and Bebout (1995) and Grove et al. (2008) indicate that there were differences in the age of metamorphism of the amphibolite, epidote-amphibolite and epidote-blueschist rocks, compared to the lower grade units. The maximum depositional age (dated with detrital zircon U-Pb ages) for the amphibolite unit is 122 ± 3 Ma, which subsequently experienced peak metamorphism at 114.5 Ma. The maximum depositional age for the lawsonite-blueschist and lawsonite-albite units is 97 ± 3 Ma, suggesting that the rocks of these facies were still on the Earth's surface when the higher-grade units were metamorphosed (Grove et al., 2008).

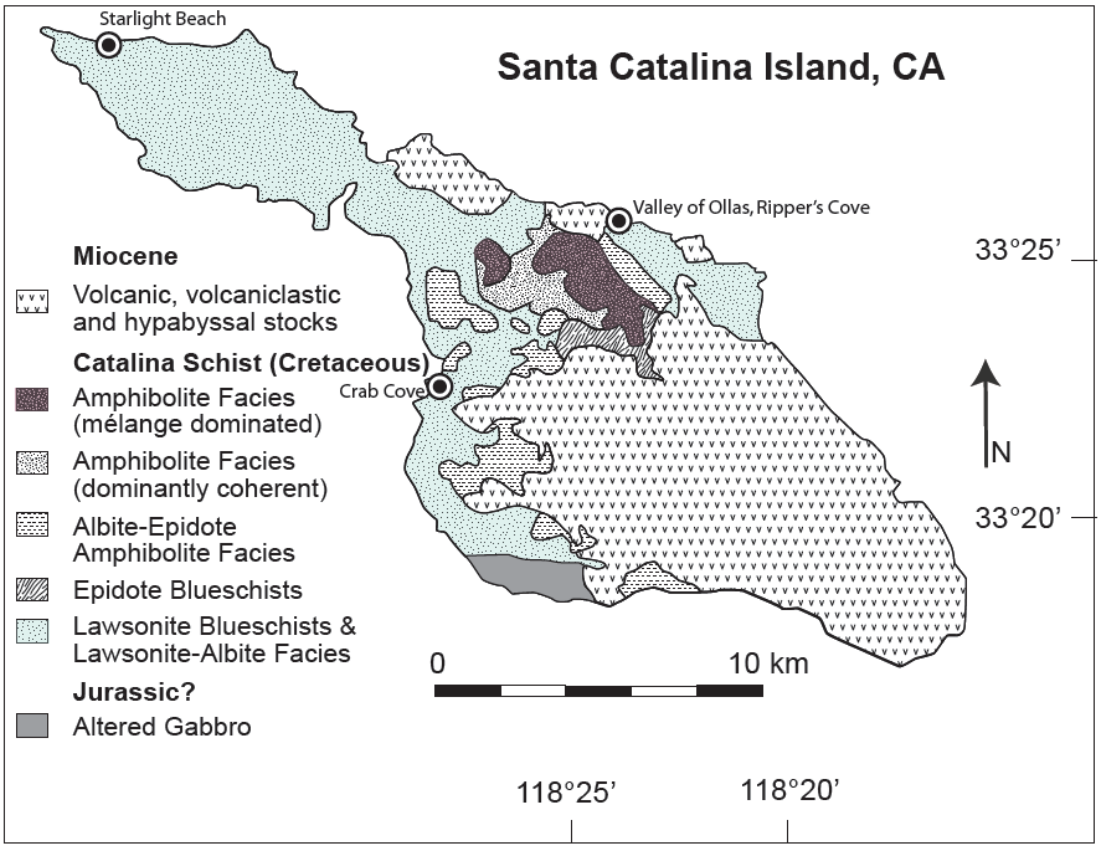

Figure 1: Geologic map of Santa Catalina Island, CA. Sampling localities are labeled with circles. The amphibolite samples collected are from the Valley of Ollas/Ripper's Cove locality. The lawsonite-albite facies blocks were sampled from Starlight Beach; and the lawsonite-blueschist samples were collected from Crab Cove.

The lower part of the amphibolite unit consists of relatively coherent metagabbroic rocks regionally overlain by migmatitic, kyanite-bearing semipelitic schists (Sorensen and Barton 1987). The upper part of the unit consists of mélange with amphibolitized eclogite blocks in a metasomatized ultramafic matrix (Sorensen and Barton 1987). Peak temperatures and pressures in the Catalina Schist amphibolite unit are constrained by mineral stabilities, i.e., limits from: garnet-clinopyroxene geothermometry, fluid inclusion data, anorthite-orthoclase-quartz melt equilibration curve, and CATSH (CaO-Al_2O_3-TiO_2-SiO_2-H_2O) reaction curves, to be between 640 and

750°C and between 0.8 to 1.1 GPa (Sorensen and Barton, 1987).

The blocks of garnet amphibolite (hornblende (Hbl) + garnet (Grt) + opaques; Sorensen, 1988) studied here are meter-scale boulders found along valleys, beaches and hillsides on the central-eastern coast of Santa Catalina Island; the ultramafic-rich matrix has been worn away by weathering. Non-migmatitic clinopyroxene bearing blocks; non-migmatitic blocks with reaction rinds; and migmatites, with or without rinds (Sorensen and Grossman 1989) are the most prevalent block types. All blocks are interpreted to have mid-ocean ridge basalt (MORB) or altered oceanic basalt (AOB) protoliths, based on major-, minor- and trace-element geochemical signatures (Sorensen, 1986). Amphibolite-grade reaction rinds are dominantly composed of amphibole and phengite, with minor Chl, ± rutile (Rt) ± epidote (Ep) ± quartz (Qtz) ± titanite (Ttn).

Lawsonite-albite and lawsonite-blueschist facies samples were collected from Starlight Beach and Crab Cove, respectively. Blocks sampled from these facies are larger in scale (several meters in diameter) relative to amphibolite-grade blocks sampled. The lawsonite-albite mafic blocks contain albite (Ab) + Chl + lawsonite (Lws) + Qtz ± carbonates (Carb) ± Act (Bebout and Barton 1989). The lawsonite-blueschist mafic blocks contain Ab + Chl + Na-amp + Lws ± Qtz ± Carb (Bebout and Barton 1989).

Work by Bebout and Barton (2002) indicates that the Catalina Schist mélange in all metamorphic facies equilibrated isotopically with an aqueous fluid that had a $\delta^{18}O$ signature indicative of a lower-temperature sedimentary source (i.e., elevated $\delta^{18}O$). Whole-rock O and B isotopic and major-element chemical compositions of blocks and

matrix in mélange of the Catalina Schist indicate addition of O, B, and Si by fluids during subduction zone metamorphism (Bebout and Barton, 1989; 2002; King et. al., 2007).

2.2 Attic-Cycladic Complex, Syros Island, Greece

The island of Syros, Greece is part of the Attic-Cycladic Complex and displays evidence for blueschist to eclogite facies metamorphism. The Attic-Cycladic Complex covers approximately 230 km x 190 km, though most lies covered by the Aegean Sea (Okrusch and Bröcker, 1990). The complex is composed of two major structural units juxtaposed by low-angle normal faults and thrust faults (Dürr et al., 1978; Okrusch and Bröcker, 1990; Seck et al., 1996; Philippon et al., 2011). The various lithologies present on the island of Syros include eclogites, metagabbros, serpentinites, metaplagiogranites, metasedimentary rocks and glaucophane-rich schists within a mélange matrix (Fig. 2). The protoliths of the metamorphic rocks seen on Syros range from MORB to sedimentary to volcaniclastic (basaltic to intermediate) lithologies. The blueschists are composed of glaucophane (Gln) + Ep +Rt + Ttn ± Phe ± paragonite (Pg) ± Chl ± Grt ±Qtz (Okrusch and Bröcker, 1990). The mélange is composed of a talc-chlorite schist and serpentinite matrix, with metasedimentary and meta-igneous blocks of varying sizes and geometries. All protoliths underwent metamorphism in the Eocene (45 ± 5 Ma) based on K-Ar and Rb-Sr analyses of paragonites, phengitic muscovites, and muscovites (Andriessen et al., 1979). Peak P-T for the high-pressure metamorphosed blueschist to eclogite facies rocks are 1.3 to 2.0 GPa and 470 to 520°C, and were determined using the presence of metamorphic mineral assemblages of jadeite (Jd) + Qtz, zoisite (Zo) + Pg + Qtz + Lws, coupled with the absence of a Lws + Jd assemblage (Dixon, 1968; Ridley, 1984; Okrusch

and Bröcker, 1990; Trotet et al., 2001; Rosenbaum et al., 2002; Keiter et.al., 2004). The high-pressure metamorphism is thought to be a result of continental collision following subduction of the Apulian microplate below Eurasia (Altherr et al., 1979; Blake et al., 1981). Hydrous minerals (e.g., chlorite, clinozoisite, and phengite) are present in reaction zones that likely formed at a time of exhumation and fluid infiltration (Okrusch and Bröcker, 1990; Seck et al., 1996; Marschall et al., 2006). A lower-pressure greenschist overprint is thought to be partly from isothermal decompression during uplift (Wijbrans et al., 1990).

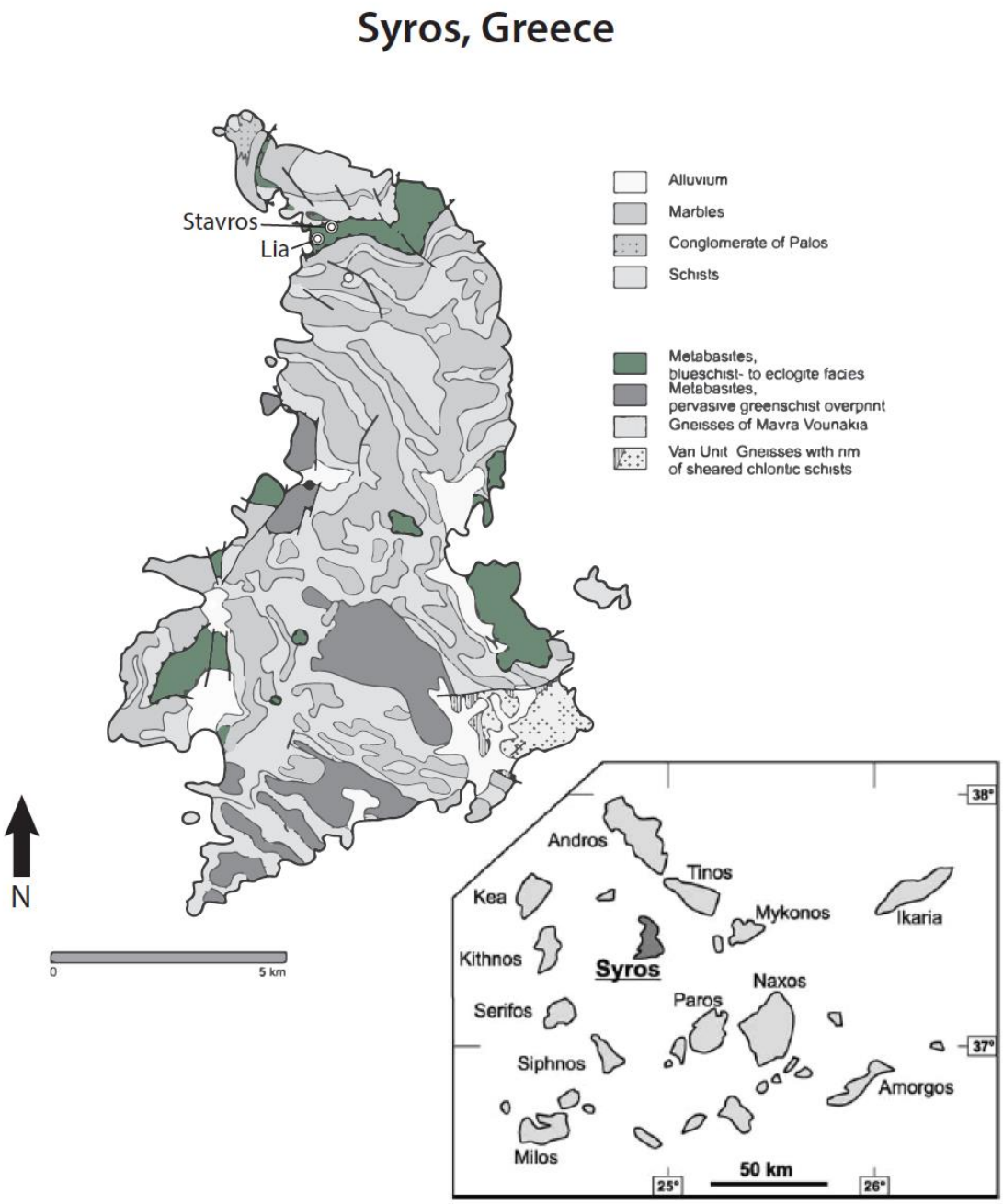

Figure 2: Geologic map of the Attic-Cycladic Complex and Syros Island after Keiter et al. (2004). The blueschist- to eclogite facies metabasites are shaded green. The Lia Beach and Stavros traverse localities are marked with a circle.

Chapter 3: Sampling Approach

3.1 Catalina Schist

This study focuses on constructing a detailed comparison of the petrology, bulk-rock chemistry, and whole-rock HSE concentrations and Os isotopic compositions of high *P-T* lithologies and reaction zones from both the Santa Catalina Island and Syros localities. These two localities were explicitly chosen due to documented differences in environment, i.e., reaction zones from the Catalina Schist locality have physical evidence for mechanical mixing processes (e.g., Penniston-Dorland et al., 2012b), whereas the reaction features in the Syros locality display evidence for static recrystallization (Miller et al., 2009). Two amphibolite-grade traverses across reaction zones were collected from the Catalina Schist. These traverses are compared to two blueschist to eclogite facies traverses across reaction zones from the Attic–Cycladic Complex. In addition to a general comparison of the two localities, samples from low-grade reaction zones in the lawsonite-blueschist and lawsonite-albite metamorphic grades of the Catalina Schist were analyzed to determine whether the extent of mechanical mixing differed as a function of various metamorphic grades within the same subduction complex.

For the Catalina Schist amphibolite-grade samples, one or two adjacent large samples (10-20 cm in diameter) were collected. These large samples were then cut with a rock saw parallel to the core-rind contact in approximately 1 cm slices, extending perpendicular to the contact in both directions (Fig. 3). Lower grade blocks were larger

(many meters in diameter); therefore, sampling the block core, rind, and matrix was not done continuously at 1cm increments. Samples were taken from core, rind, and matrix separately on the scale of tens-of-cm to a few meters sampling intervals.

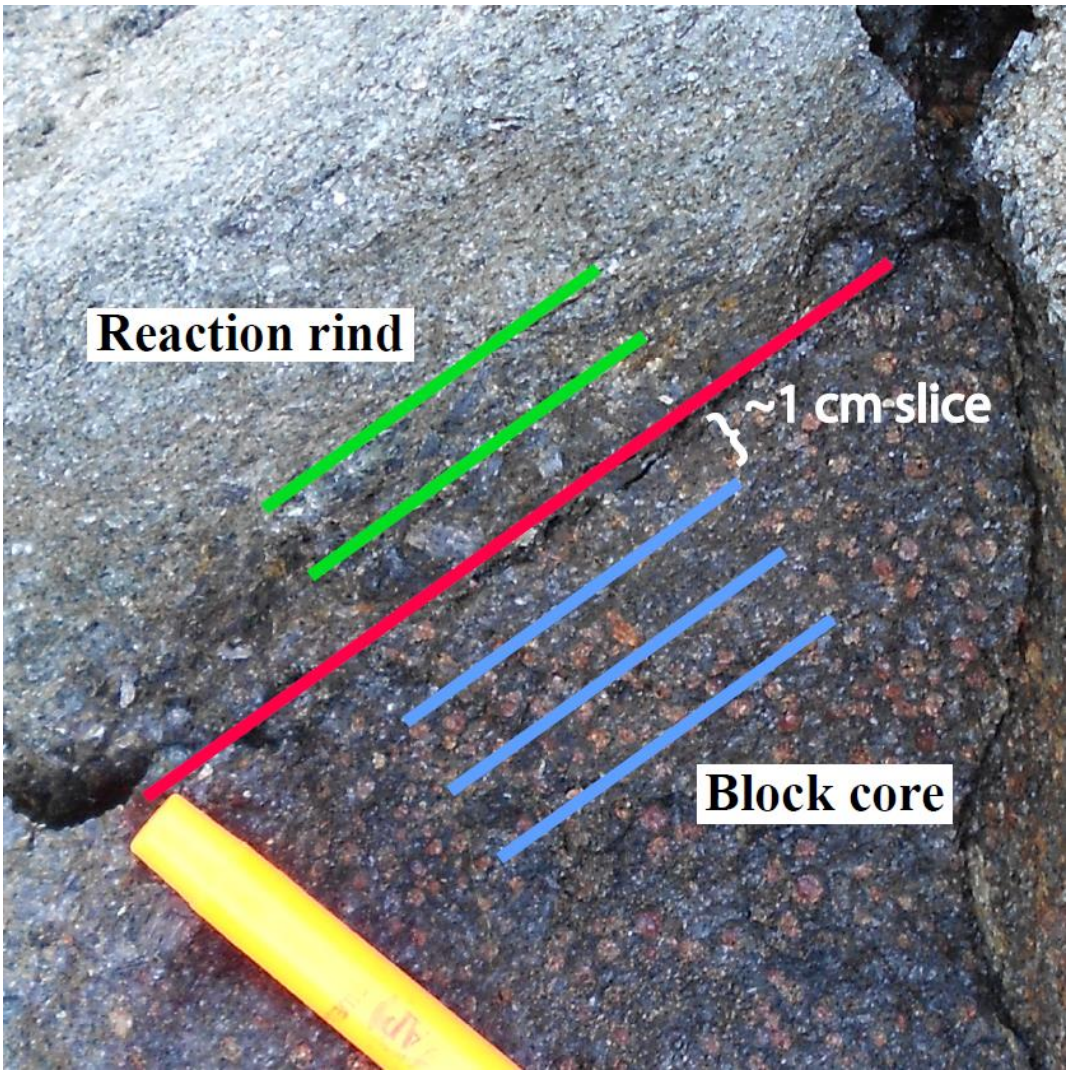

Figure 3: Field photo of a garnet amphibolite block core and reaction rind. The red line shows the contact. Green and blue lines illustrate the sample-cutting strategy. Slices were cut parallel to the core-rind contact.

3.2 Attic-Cycladic Complex

All Syros samples were collected by Horst Marschall (currently at WHOI) and colleagues. Samples were collected perpendicular to chlorite-schist/serpentinite contacts for both traverses (Lia Beach traverse and Stavros traverse). The Lia Beach samples were collected as two separate smaller traverses approximately 2 meters apart (Fig. 4) and then combined to make a detailed single traverse spanning all 5 zones.

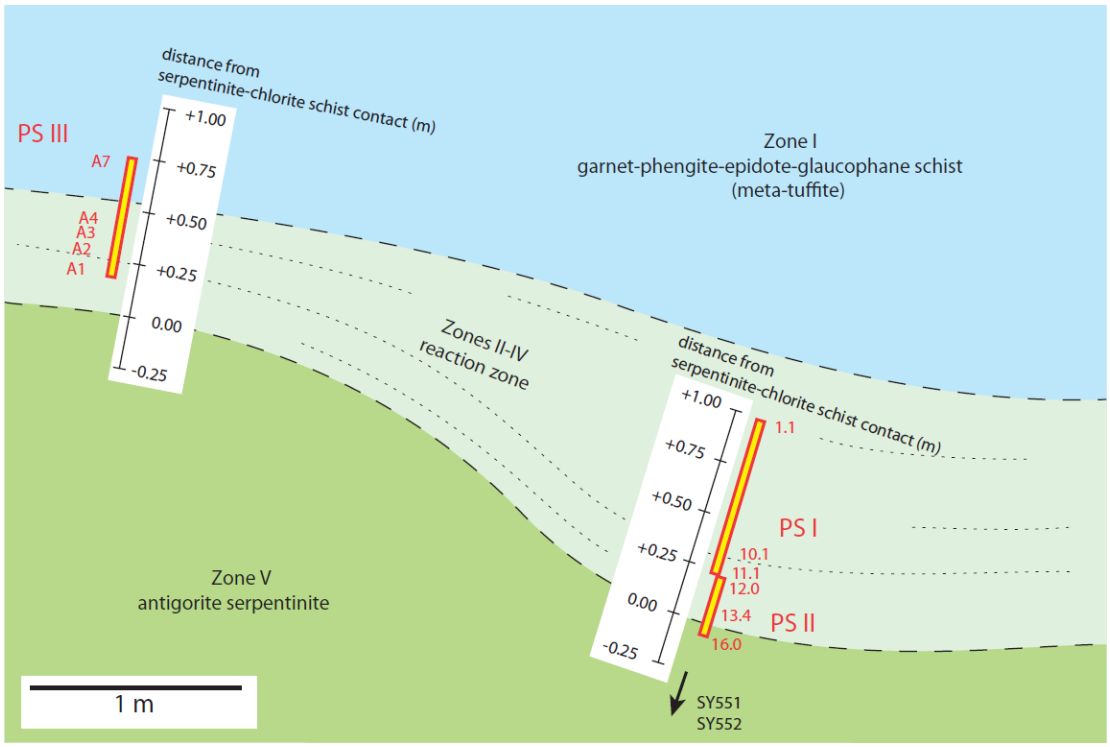

Figure 4: Diagram from Marschall (unpublished) showing sample locations for the Lia Beach traverse. Distances are measured relative to contact between the serpentinite (Zone V) and the chlorite schist reaction zone (Zone IV).

Chapter 4: Analytical Methods

4.1 X-Ray Fluorescence (XRF)

Major and trace element concentrations for samples were obtained from the X-ray Laboratory at Franklin and Marshall College under the supervision of Dr. Stan Mertzman, using a Philips 2404 XRF spectrometer. Duplicate sample analyses for one Catalina Schist amphibolite grade rind sample are in good agreement (≤1% deviation) for SiO_2, Fe_2O_3, MnO, and MgO). Larger deviations are as follows: TiO_2 (7.2%), Al_2O_3 (5.3%), Na_2O (2.9%), K_2O (5.7%), and P_2O_5 (16. 7%). The large deviations are associated with low total wt% compositions. The accuracy of the analyses reported from the XRF laboratory at Franklin and Marshall college is ~1% relative uncertainty for major elements present in concentrations >0.5 wt% and ~3% for major elements <0.5 wt% and ~5% for trace elements greater than 20 ppm in concentration.

4.2 Electron Probe Microanalyzer (EPMA)

All EPMA data were obtained using the JEOL 8900 Electron Probe Microanalyzer (EPMA) at the University of Maryland. Garnet analyses were performed using Wavelength Dispersive Spectroscopy (WDS). The conditions were as follows: 15 kV accelerating voltage, 50 nA cup current, and a 3 μm beam diameter. Standards used were as follows: Garnet–12442 for MgO, FeO, Al_2O_3, CaO and SiO_2, Ilmenite for MnO

and Kakanui Hornblende for TiO_2. Operating conditions for garnet x-ray maps were as follows: 15 kV accelerating voltage, 250nA cup current, 200 ms dwell time, 2μm beam diameter with 2 μm step size for garnets in reaction zones, and an 8μm beam diameter with an 11 μm step size for garnets in block cores.

Mineral abundances were determined via detailed point counting using the JEOL 8900 Electron Probe Microanalyzer (EPMA) at the University of Maryland. A grid of equally-spaced steps ~600 μm in both x and y directions was programmed for all thin sections counted. Mineral modes for the A10-3 and A12-A4 traverses were measured via counting >2000 points (with the exception of the A10-3C rind sample with only 1847 points counted) in thin section. Point counting was also conducted on one lawsonite-albite core-rind pair (731 and 694 points counted, respectively) and one lawsonite-blueschist core-rind pair (659 and 2232 points counted, respectively; data from Penniston-Dorland et al., in prep). The energy-dispersive spectrometer (EDS) was used to identify the phases based on the relative proportions of peak heights. Error for point counting modes was assessed using figures from Howarth (1998) displaying upper and lower 95% confidence intervals, and are a function of the relative proportions of points counted.

4.3 HSE analyses

Concentrations of Os, Ir, Pt, Pd, Re, and Ru were determined via isotope dilution using multiple spikes enriched in ^{185}Re, ^{190}Os, ^{191}Ir, ^{194}Pt, ^{105}Pd and ^{99}Ru. Details of the technique have been published elsewhere (Becker et al., 2006; Rehkämper et al., 1997;

Schulte et al., 2009; Shirey and Walker, 1995). Samples were sanded and crushed in an alumina mortar and pestle to avoid contamination from the metal rock saw. To achieve sample digestion, samples were ground to a fine powder using a SPEX 8000M small shatterbox at the University of Maryland. Samples were then sealed in 8 in. Pyrex Carius tubes with 6mL conc. Teflon distillled HNO_3 and 4mL conc. Teflon distilled HCl, then heated for a minimum of 3 days at 240 °C. The amount of sample digested ranged from 1.5 to 2 g. After digestion, Os was separated by solvent extraction from the acid phase into CCl_4 and back extracted into conc. HBr using the methods described in Cohen and Waters (1996), followed by microdistillation using chromic acid and HBr (Birck, 1997). Ruthenium, Ir, Pt, Pd and Re were separated and purified by anion exchange chromatography (Rehkämper and Halliday, 1997).

Osmium isotopic ratios were measured by negative thermal ionization mass spectrometry (N-TIMS) using an electron multiplier on the VG Sector 54 multi collector instrument at the University of Maryland. Some samples were run on the University of Maryland NBS 68° sector instrument using an electron multiplier. Samples were loaded onto a Pt filament and $Ba(OH)_2$ was applied to the dried sample to reduce the work function and increase ion production. Osmium blanks averaged 6.2 pg (n=5) for the first groups of samples analyzed. After switching to purged and Teflon distilled nitric acid for digestion, Os blanks dropped to an average of 1.1 pg (n=5). $^{187}Os/^{188}Os$ blank ratios averaged 0.1695 ± 0.04 (n=9). For Catalina rind samples, Os blank comprised <0.5% of sample Os. For cores, Os blank comprised between 0.2 to 9% of the total sample Os. For

the Syros samples, the Os blank was as much as 23% of the total Os for the lowest concentrations of Os.

Samples with high Re/Os ratios have a considerable radiogenic Os component in the calculated Os concentrations. Therefore, common Os concentrations are more useful when comparing Os concentrations in highly radiogenic samples, as they exclude radiogenic Os from Os concentration comparisons. Common Os was calculated by subtracting radiogenic Os from calculated Os concentrations, assuming a mantle Os isotopic composition of 0.1270. The most radiogenic samples (i.e., Stavros traverse eclogite block and metasomatic reaction zone samples) have common Os concentrations as much as 69% less than the original calculated Os concentrations. Samples that do not have high Re/Os ratios have common Os concentrations equal within error of calculated Os concentrations, and are therefore not reported.

Ruthenium, Ir, Pt, Pd and Re were measured via *Nu Plasma* MC-ICP-MS at the University of Maryland. Total chemistry average blanks were: Re 7.4 +11.4/-7.4 pg (n=9), Pd 37 ± 27 pg (n=8), Pt 90 +156/-90 pg (n=9), Ru 9.0 ± 7.7 pg (n=9), Ir 0.75 ± 0.6 pg (n=9). Accuracy of the ICP-MS measurements was monitored via standards. The blank contribution to the total mass of Re, Ir, Ru, Pt, and Pd varied considerably over the span of concentration ranges and was also affected by a few anomalously high (>100 pg) blanks. Samples with less than 0.1 ppb Re had blanks contribute as much as 57% of the total Re measured. Uncertainties in blanks were propagated into errors reported for concentrations. Duplicate analyses of A12-A4-C1 have good agreement in Os concentrations, giving concentrations for the original and duplicate analyses of 0.005 ppb

and 0.006 ppb, respectively. Duplicate analyses of A12-A4-R3 have concentrations of 2.96 and 1.57, showing variability of Os concentrations in the rind. For block core samples A12-A4-C3 and A12-A4-C5, Pt blanks exceed the calculated concentrations and are thus considered below the detection limit. Ruthenium blanks account for up to 64% of the total mass of Ru measured in samples with concentrations lower than ~0.01 ppb. Iridium blanks consist of no more than 17% of the total Ir measured for core samples and generally consist of less than 1% of the total Ir measured for rind samples. Pd blanks are under 37% of the total Pd measured for core samples and generally consist of less than 1% of the total Pd measured for rind samples.

The ages used for calculation of initial $^{187}Os/^{188}Os$ ratios from measured $^{187}Re/^{188}Os$ are the oldest reported metamorphic ages for each of the different subduction zone complexes. The age corrections for block rinds are negligible due to the low Re/Os of these samples. Use of the maximum ages of metamorphism results in the largest age correction for block core samples, thus, minimizing the difference in initial $^{187}Os/^{188}Os$ between block cores and rinds. For the Catalina Schist amphibolite facies samples a correction age of 114.5 Ma (Anczkiewicz et al., 2004) was used and for lawsonite-albite and lawsonite-blueschist samples a correction age of 97 Ma (Anczkiewicz et al., 2004) was used. Syros samples were corrected to an age of 45 Ma (Andriessen et al., 1979). Due to the moderate to high Re/Os contents of some of the block core samples, age corrections of as much as 43% (A10-3C-C5) were made to $^{187}Os/^{188}Os$ ratios.

The UB-N rock standard was analyzed and compared to previous HSE concentration results from the Isotope Geochemistry Laboratory (IGL) at the University

of Maryland and other previous results from the literature. UB-N values (n=2) were within 4% of reported values in Meisel and Moser, (2004) and Puchtel and Humayun, (2005) for Re, Os, Ir, Ru, Pt, and Pd. Overall, HSE uncertainties varied greatly and are reported in Table 12 and Table 13.

Chapter 5: Traverse overviews – mineralogy and mineral textures

5.1 Catalina Schist

5.1.1 Traverse A10-3, amphibolite grade

Traverse A10-3 comes from a meter-size amphibolite-grade block found as float in Ripper's Cove, Santa Catalina Island (Fig. 5). The traverse consists of 32 samples spanning 30cm between an amphibolite-grade block and its reaction rind. Mineral modes for the core and rind were determined by point counting. One thin section from the rind (A10-3A), one from the core (A10-3D), and one containing both core and rind and the contact between the two (A10-3C) (Table 1) were counted. Scans of the thin sections for both core and rind are shown in Figure 6. The block core is predominantly amphibole with garnet porphyroblasts (Fig. 6; accessory minerals include Phe + Chl + Rt + Ap + Ttn + Ep +Fe-sulfides + Qtz). The rind is composed predominantly of amphibole, phengite, and chlorite, and also contains a few smaller garnets partially replaced by chlorite and phengite (Fig. 7a; 7c). The rind is concentrically foliated and wraps around the block core (Fig. 5). Core garnets contain abundant inclusions of Phe + Chl +Ap + Ttn + Rt + Qtz +Ab + Ep. There are also instances of rind amphibole being replaced by chlorite and phengite (Fig. 7b). Some garnets in both rind and core show needle-like rutile inclusions, suggesting formation due to exsolution of Ti from garnet during cooling (Zack et al., 2004; Fig. 7c).

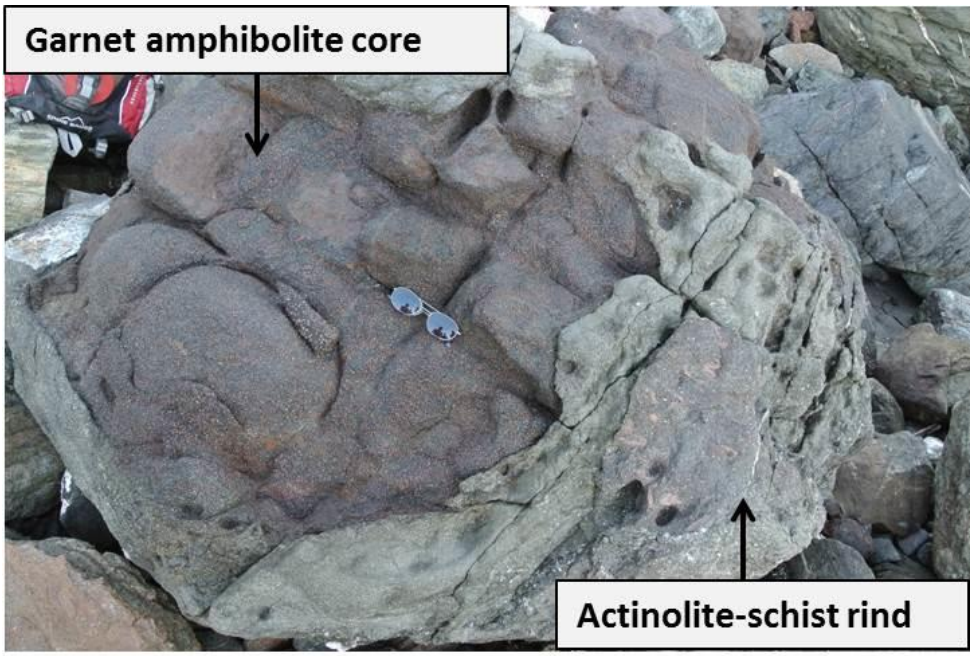

Figure 5: A10-3 Garnet amphibolite core surrounded by actinolite-schist rind. Sunglasses on the core illustrate scale.

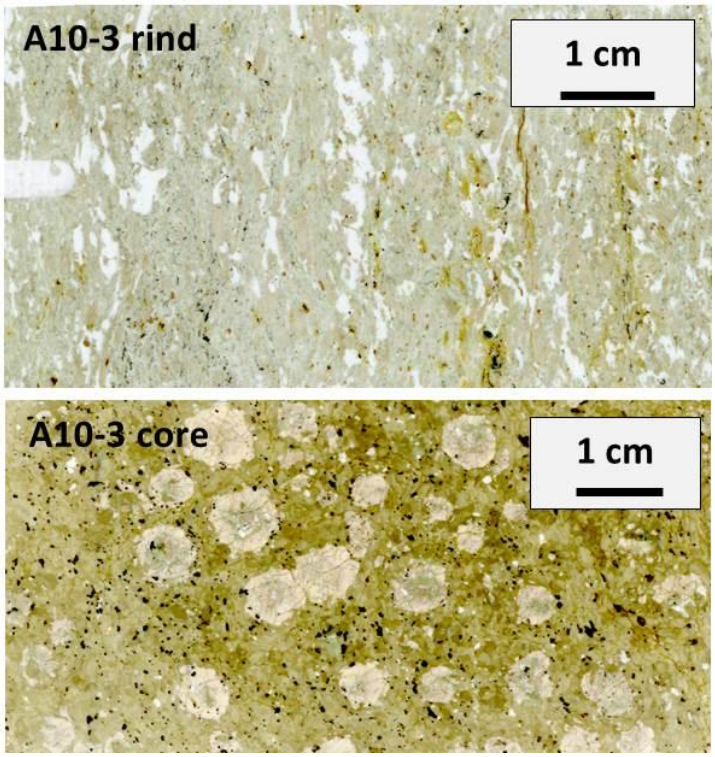

Figure 6: Representative thin section scans of A10-3 rind and core. The core is composed of predominantly amphibole and garnet porphyroblast. The rind consists predominantly of amphibole, phengite, and chlorite.

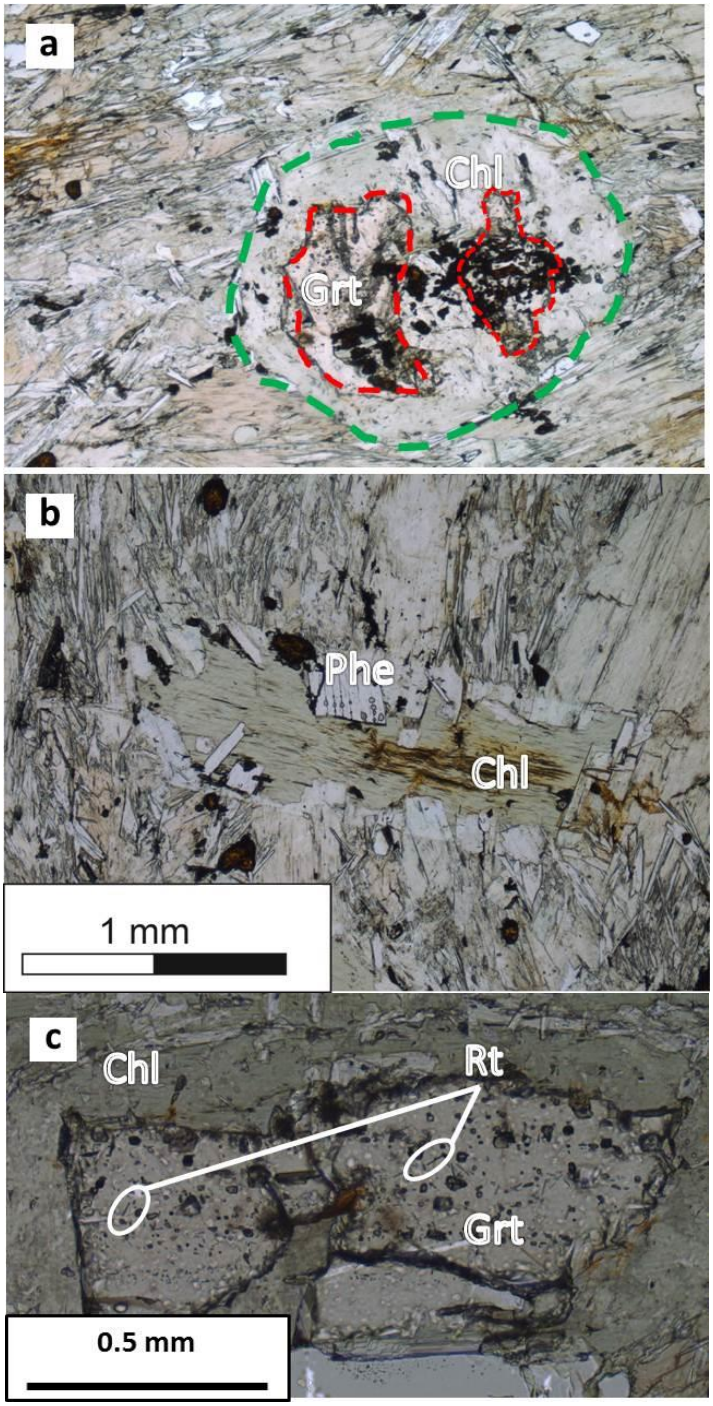

Figure 7: Photomicrographs of the A10-3 traverse. a) A10-3 rind garnet (outlined in red) being replaced by chlorite. The interpreted original garnet is outlined in green (image to same scale as image b). b) A10-3 amphibole replaced by chlorite and phengite. c) A10-3 rind garnet being replaced by chlorite and showing needle-like rutile inclusions indicative of Ti exsolution from garnet during cooling.

Table 1: Mineral modes (volume %) and associated counting uncertainties for the A10-3 core and rind.

Phase	A10-3D-core		A10-3C-core		A10-3C-rind		A10-3A-rind	
	vol %	2σ (%)[1]	vol %	2σ (%)[1]	vol %	2σ (%)[1]	vol%	2σ (%)[1]
Amphibole	72.6	±1.9	76.4	±1.7	85.3	± 1.7	55.2	± 2.1
Phengite	1.3	-0.5/+0.7	3.4	-0.7/+0.8	7.5	-1.2/+1.4	24.2	±1.9
Chlorite	1.5	-0.5/+0.7	4.8	-0.8/+1.0	6.4	-1.1/+1.3	5.4	-0.9/+1.1
Garnet	18.6	±1.8	11.2	±1.4	-		0.3	-0.2/+0.4
Grt Inclusions[3]	2.5	-0.6/+0.9	2.5	-0.6/+0.9	-		-	
Rutile	2.0	-0.6/+0.9	1.3	-0.4/+0.6	0.7	-0.3/+0.5	0.6	-0.3/+0.5
Apatite	0.9	-0.4/+0.6	0.2	-0.1/+0.3	trace[2]		0.3	-0.2/+0.4
Titanite	0.1	-0.1/+0.3	-		0.1	-0.1/+0.3	0.3	-0.2/+0.4
Epidote	0.1	-0.1/+0.3 -0.2/+0.3	0.1	-0.1/+0.2	-		- trace[2]	
Fe Sulfide	0.3		-		-			
Quartz	0.1	-0.1/+0.3	-		trace[2]		13.7	± 1.5
Zircon	0.1	-0.1/+0.3	trace[2]		trace[2]		trace[2]	
Total # points counted	2067		2674		1861		2123	

[1]Uncertainties reported are % 2σ using figures from Howarth (1998).
[2]"trace" indicates the minerals with <0.05% abundance.
[3]"Grt inclusions" encompasses all inclusions counted in garnets.

5.1.2 Traverse A12-A4, amphibolite grade

Traverse A12-4 comes from an amphibolite-grade block found as float in the Valley of Ollas, Santa Catalina Island. The traverse consists of 13 samples spanning ~27 cm across an amphibolite-grade block and its reaction rind. Mineral modes were determined via point counting (Table 2). The block core consists predominantly of amphibole and garnet porphyroblasts with minor Qtz + Rt + Chl + Phe + Ap + Lws + Ttn. The amphibole in the core has undergone some alteration to phengite, chlorite, and trace lawsonite (Fig. 8a). In contrast to the A10-3 traverse core garnets, A12-A4 garnets have minimal inclusions (Fig. 8b). An ~1 cm thick lens of mm-diameter garnets is

present in part of the block core (Fig. 8c). Core garnets contain dominantly quartz and rutile inclusions (Fig. 8d). The rind is composed predominantly of amphibole, phengite, quartz, and chlorite. The rind is foliated and wraps around the concentric block core. No garnets have been found in the rind thin sections analyzed.

Table 2: Mineral modes (volume %) and associated counting uncertainties for A12-A4 core and rind.

Phase	**A12-A4 core**		**A12-A4 rind**	
	vol %	2σ (%)[1]	vol %	2σ (%)[1]
Amphibole	79.0	-1.2/+1.5	83.7	±1.5
Phengite	0.9	-0.3/+0.5	1.8	-0.5/+0.6
Chlorite	1.5	-0.4/+0.6	7.9	-1.0/+1.1
Garnet	14.9	-1.3/+1.4	-	
Grt Inclusions	0.4	-0.2/+0.3	-	
Rutile	1.5	-0.4/+0.6	0.2	-0.2/+0.3
Apatite	0.7	-0.3/+0.4	-	
Titanite	trace[2]		-	
Lawsonite	trace[2]		trace[2]	
Fe Sulfide	-		0.2	-0.2/+0.3
Quartz	2.2	-0.5/+0.6	7.9	-1.0/+1.1
Zircon	-		trace	
Total # points counted	2297		2128	

[1]Uncertainties reported are % 2σ using figures from Howarth (1998).
[2]"trace" indicates the minerals with <0.05% abundance.
[3]"Grt inclusions" encompasses all inclusions counted in garnets.

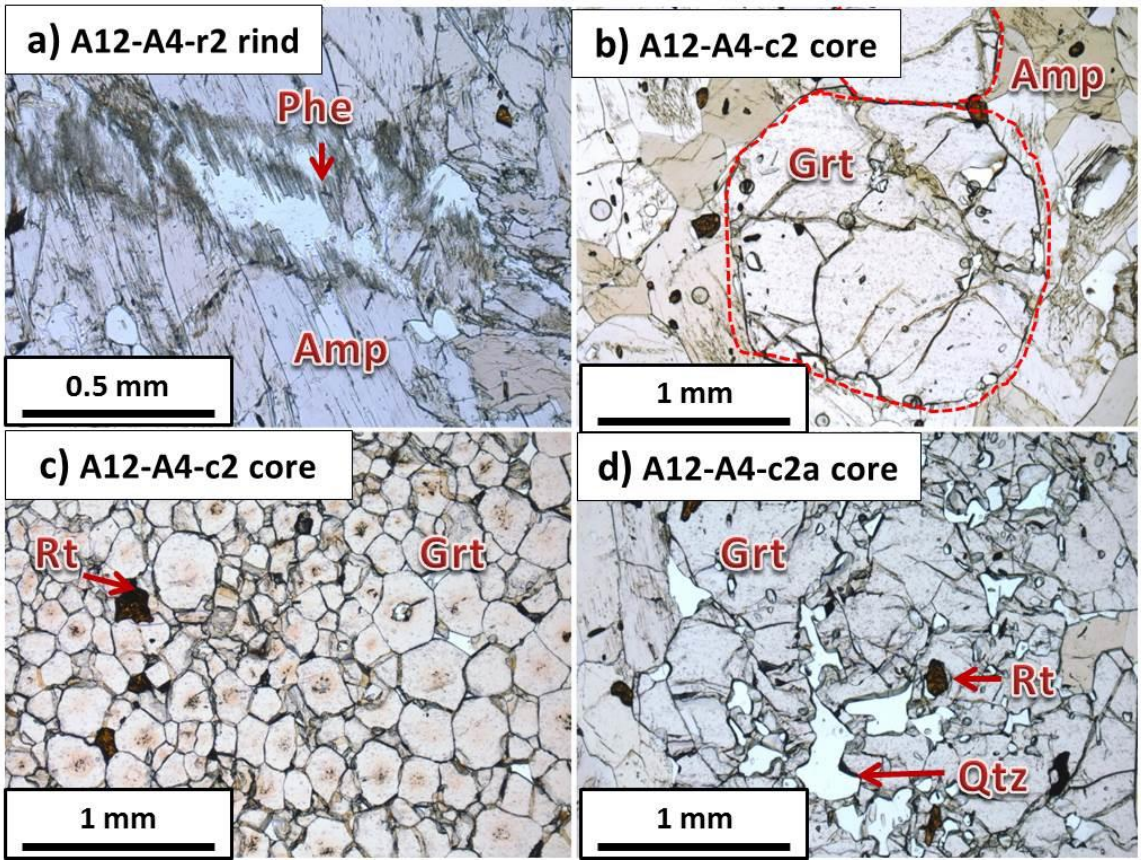

Figure 8: Photomicrographs of the A12-A4 traverse. a) Replacement of amphibole by phengite. b) Euhedral core garnets (outlined in red) with minimal inclusions. c) Garnet lens in A12-A4 core with rutile grains. d) Large garnet showing multiple rutile and quartz inclusions.

5.1.3 Lawsonite-blueschist and lawsonite-albite grade traverses

LA10-3 samples come from a decameter-scale lawsonite-albite grade block and rind found at Starlight Beach, Santa Catalina Island (Fig. 1). Mineral modes were determined via point counting (Table 3). Lawsonite-albite facies core sample LA10-3B contains Chl + Ab + Lws + Phe with minor Ttn + calcite (Cal) + Ap. The lawsonite-albite rind sample is predominantly chlorite and amphibole, with minor titanite and apatite.

Lawsonite-albite facies samples have been found to have pieces of mafic block breaking off into mélange matrix (Fig. 9).

Table 3: Mineral modes (volume %) and associated counting uncertainties for the lawsonite-albite facies.

Phase	**LA10-3B core**		**LA10-3F rind**	
	vol %	2σ (%)[1]	vol %	2σ (%)[1]
Amphibole	-		30.1	-3.1/+3.4
Phengite	16.6	-2.2/+2.6	-	
Chlorite	27.6	-3.1/+3.2	66.0	-3.6/+3.2
Calcite	1.4	-0.7/+1.1	-	
Albite	24.9	-3.0/+3.2	-	
Apatite	0.4	-0.3/+0.8	0.86	-0.5/+1.0
Titanite	3.7	-1.2/+1.6	3.0	-1.1/+1.5
Lawsonite	25.4	-3.0/+3.2	-	
Total # of points counted	731		694	

Data from Penniston-Dorland et al. (in prep).
[1]Uncertainties reported are % 2σ using figures from Howarth (1998).

Figure 9: Sample of drill core from the lawsonite-albite facies showing mafic block (green) and matrix (black). Part of the block has broken off and was surrounded by matrix.

LB10-1 samples are from a decameter-scale lawsonite-blueschist block located in Crab Cove, Santa Catalina Island. The mafic block is surrounded by a reaction rind, and both block and rind are surrounded by matrix (Fig. 10). Mineral modes were determined by point counting (Table 4). Lawsonite-blueschist facies block core sample LB10-1A

contains Chl + Ab + Cal + Ttn + Phe, with minor Lws + Amp + Ap. The lawsonite-blueschist rind sample (LB10-1B) contains predominantly Ab + Amp + Chl + Phe + Cal + Qtz ± Ap ± Ttn ± Fe-sulfides.

Table 4: Mineral modes (volume %) and associated counting uncertainties for the lawsonite-blueschist facies.

Phase	**LB10-1A core**		**LB10-1B rind**	
	vol %	2σ (%)[1]	vol %	2σ (%)[1]
Amphibole	0.61	-0.6/+0.9	17	-1.6/+1.7
Phengite	4.4	-1.4/+1.8	8.1[3]	-1.1/+1.2
Chlorite	55	±3.8	28[3]	±1.9
Albite	26	-3.2/+3.4	39	±2.1
Fe Sulfide	-		trace[2]	
Apatite	0.30	-0.3/+0.8	0.13	-0.1/+0.3
Titanite	4.9	-1.5/+1.9	-	
Lawsonite	0.91	-0.6/+1.0	0.09	-0.08/+0.2
Calcite	8.0	-1.9/+2.2	5.1	-0.9/+1.0
Quartz	-		1.2	-0.4/+0.6
Total # points counted	659		2232	

Data from Penniston-Dorland et al., in prep.
[1]Uncertainties reported are % 2σ using figures from Howarth (1998).
[2]"trace" indicates the minerals with <0.05% abundance.
[3]Phengite and chlorite are interlayered on a fine-scale.

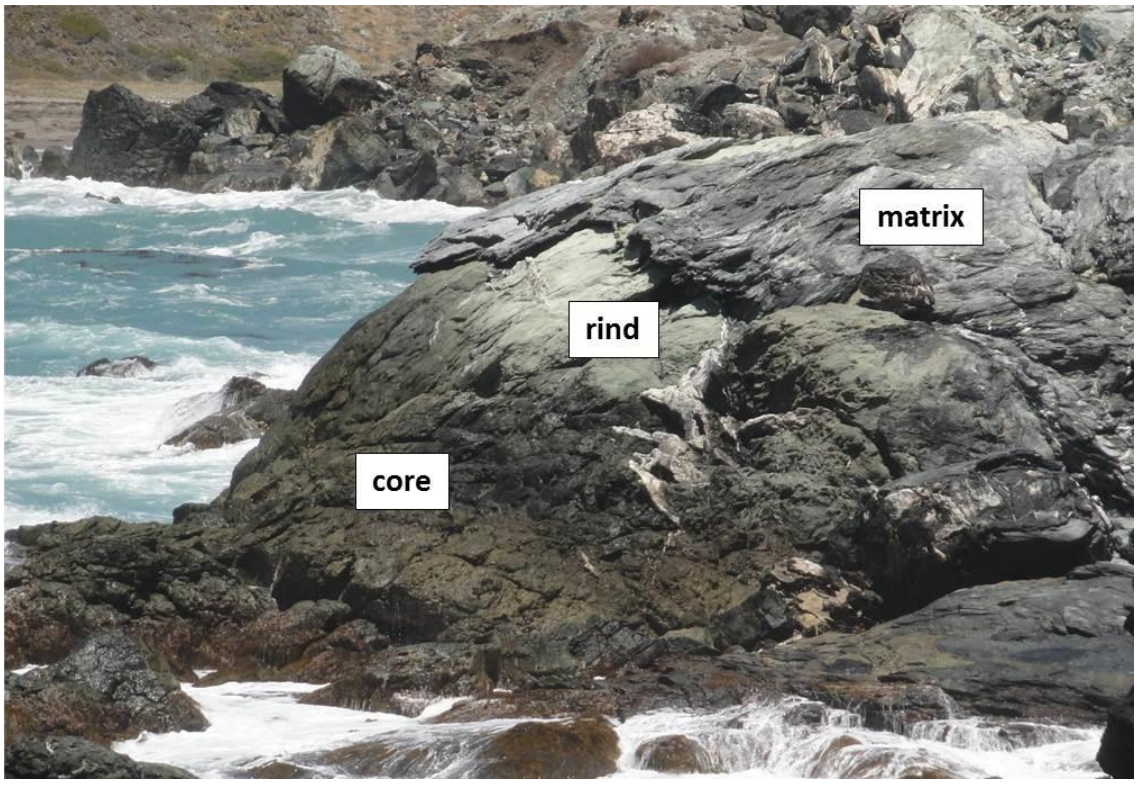

Figure 10: Lawsonite-blueschist core, rind, and matrix in Crab Cove, Santa Catalina Island. The mélange matrix concentrically wraps around the rind and block core.

Both lawsonite-albite and lawsonite-blueschist facies rinds are concentrically foliated. The interface between block, rind, and matrix in these lower-grade blocks is complex (Fig. 11). Though not analyzed in this study, many localities also have a complex sedimentary component in the mélange matrix.

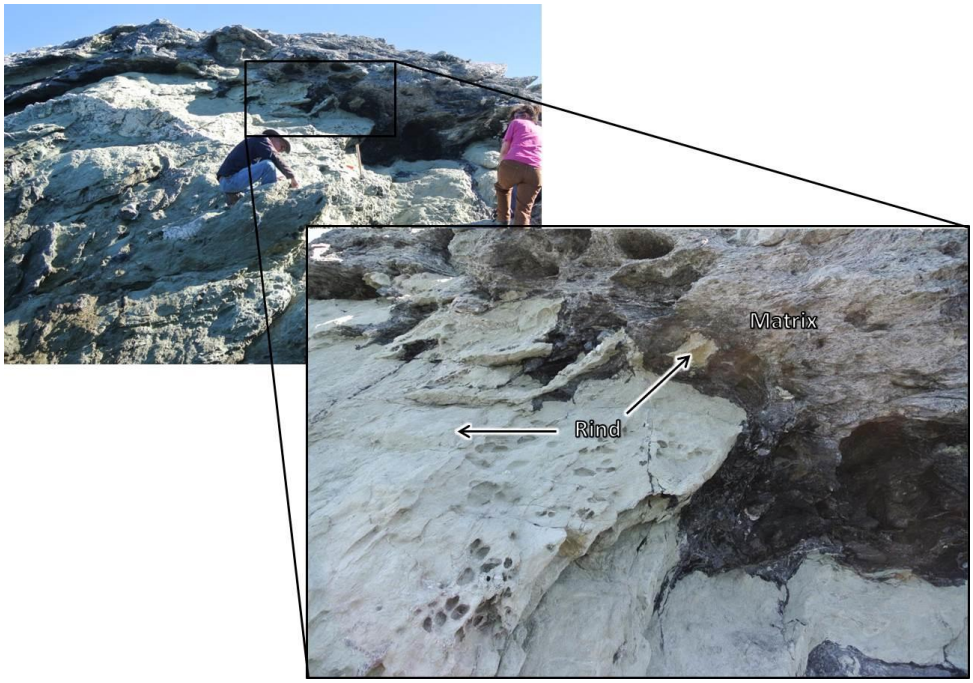

Figure 11: Lawsonite-blueschist rind and matrix. Pieces of rind float in the matrix/sedimentary material.

5.2 Attic-Cycladic Complex

5.2.1 Lia Beach traverse

The Lia Beach traverse consists of samples spanning 165 cm between blueschist-grade metamorphosed volcaniclastic (basaltic to andesitic) tuffs and a >50 m serpentinite lens, between which there is a 1-2m thick reaction blackwall zone that consists predominantly of chlorite schist (Miller et al., 2009). Samples were collected along two separate contact parallel traverses (Fig. 4). The reaction zone from the PSI and PSII samples is almost double the thickness of the PSIII traverse section. The combined traverse is divided into 5 zones: Zone I is relatively unaltered meta-tuffite, Zones II and

III are metasomatically altered meta-tuffite, Zone IV is the blackwall reaction zone and Zone V is the serpentinite lens. The mineral assemblages in each zone are: Zone I (Gln + Ep + Grt + Phe), Zone II (Gln + Ep + Chl), Zone III (Omp + Ep + Chl + Ab), Zone IV (Chl + Ttn + Rt ± Ap), Zone V (serpentine (Srp) + chromite (Chr)) (Miller et al., 2009). For simplicity, Zones II and III will be referred to as the "metasomatic reaction zone", and Zone IV will be referred to as the "chlorite-schist blackwall". Zone I will be referred to as the "meta-tuffite", and Zone V as "serpentinite". There is evidence in the metasomatic reaction zone for static recrystallization in the form of preserved decussate chlorite after garnet pseudomorphs (Miller et al., 2009). However, there is also lineation present in the serpentinite, chlorite-schist blackwall and metasomatic reaction zone samples rich in glaucophane. Miller et al. (2009) described that the lineation increases in intensity as proximity to the chlorite-schist blackwall increases, and that there is also a reaction contact-parallel micro-foliation.

5.2.2 Stavros traverse

The Stavros samples include serpentinite matrix and a traverse consisting of samples spanning 5 meters across an eclogite block with reaction rind approximately 5 m in diameter. The traverse is divided into 5 zones based on mineral abundance. Zone A consists of the samples collected closest to the center of the glaucophane-rich eclogite block core (~75 cm). Zone B consists of Gln + Grt + Omp, and spans ~60cm. Zone C consists of Gln + Jd + Grt and spans ~20cm. Zone D includes the reaction zone which consists of Chl +Act +Tlc and spans ~10cm. Zone E is serpentinite matrix. The contact

between the serpentinite and the chlorite schist reaction zone is thought to represent the original serpentinite-eclogite contact prior to metasomatism.

Zones A, B, and C, all consist of fine grained matrix of varying proportions of glaucophane and omphacite surrounding garnet porphyroblasts ranging up to ~0.5 cm. Zone A garnets are euhedral and some show multiple episodes of growth, defined by mineral inclusions outlining euhedral growth zones (Fig. 12d). Zone B has significant replacement of garnet by omphacite (Fig. 12c). Zone C has garnet being replaced at the grain boundaries with white mica (Fig. 12b). The chlorite schist reaction zone (Zone D) is foliated with large actinolite porphyroblasts (Fig 12a). For simplicity, Zones B and C will be grouped together under "metasomatic reaction zone", and Zone D will be referred to as the "chlorite-schist reaction zone". Zone A will be referred to as the "eclogite block", and Zone E as "serpentinite".

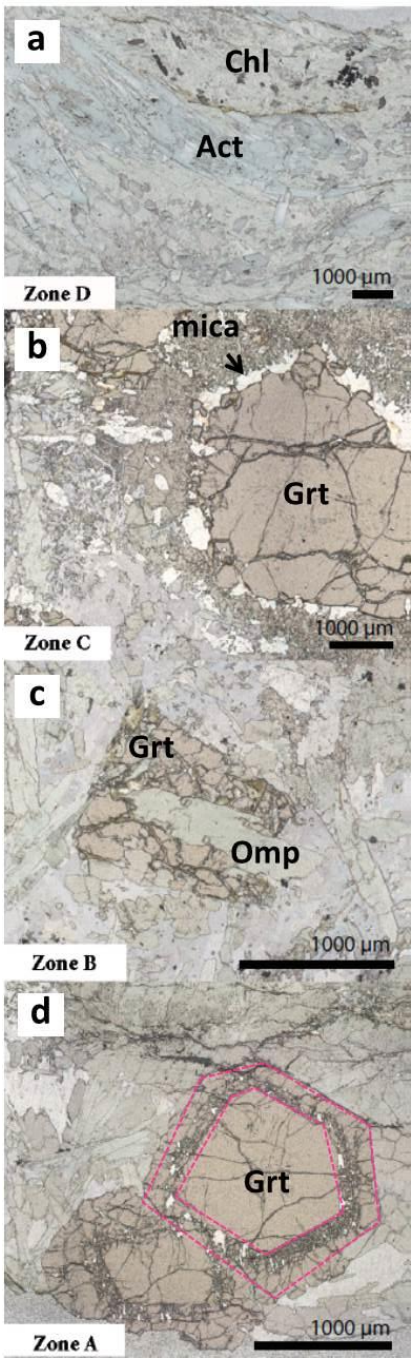

Figure 12: Photomicrographs in PPL showing mineral textures across the Stavros traverse. a) Chlorite-schist reaction zone (Zone D; SY522-000): major minerals include Chl + Act + Tlc; b) Metasomatic reaction zone (Zone C; SY522-030): major minerals include Gln +Jd+ Grt. Some garnet rims display replacement of garnet grain boundaries by white mica; c) Metasomatic reaction zone (Zone B; SY522-040) major minerals include Gln + Grt + Omp. The photomicrograph shows replacement of garnet by omphacite; d) Eclogite block (Zone A; SY522-175). It has up to ~0.5 cm garnet porphyoblasts, some showing multiple stages of garnet growth (outlined in pink).

Chapter 6: Garnet Mineral Chemistry

In order to determine the chemical compositions of different zones within the garnets, the centers and rims of two garnets from the core, and three garnets from the rind, all from the A10-3 traverse, were analyzed via wavelength dispersive spectroscopy (WDS). In addition, both quantitative (WDS) spot analysis traverses across garnets (Fig. 13) as well as x-ray maps (Figs. 14; 15) were obtained for Fe, Mn, Mg, Ca, and Cr in order to characterize chemical zoning of the garnets. Spacing of points along traverses ranged from approximately 30 to 100 microns. Analyses with wt% totals below 98% and above 102% were discarded. Analyses with wt% compositions not characteristic of garnet were also discarded (i.e., analyses with >3% TiO_2), as these analyses represent garnet inclusions.

Core garnets display concentric zoning of Ca, Mg, and Mn (Fig. 13; 15; appendix). Calcium oxide and MnO contents are highest in the garnet centers and lowest in the garnet rims. Magnesium oxide contents are lowest in the garnet centers and highest in the garnet rims (see appendix for all garnet chemical composition data). Iron oxide compositions vary from garnet to garnet and do not display significant zoning. Chromium compositions, where measured, are uniform within uncertainty from garnet center to rim.

The compositions of the centers of these core garnets can also be compared to the compositions of rind garnets (Table 5). Certain chemical distinctions are evident when comparing the center of core garnets to rind garnets. Rind garnets generally contain higher MnO concentrations compared to core garnet centers (Fig. 13). Rind garnets

contain lower CaO concentrations; the lowest average core garnet center contains 7.58 wt% CaO while the highest average rind garnet contains 5.69 wt% CaO. Rind garnets are more MgO-rich than core garnets; the highest average MgO composition in the center of core garnets is 5.81%; whereas, the lowest average MgO composition in the rind garnets is 6.50%. Iron oxide compositions of the center of core and rind garnets are similar, with compositions cluster just above 25 wt%. The rind garnets and core garnets have similar Al_2O_3 concentrations; all are just above 21 wt%.

Table 5: Garnet chemical compositions. Average chemical composition in wt% and atoms per formula unit of the centers of garnets from rind and core samples.

	Rind			**Core**			
	Garnet 1	Garnet 2	Garnet 3	Garnet 8		Garnet 9	
				center*	rim	center*	rim
Oxide wt.%							
SiO_2	38.03	37.60	37.98	37.51	37.91	37.69	38.07
TiO_2	0.07	0.04	0.07	0.06	0.13	0.14	0.14
Al_2O_3	21.26	21.22	21.28	21.33	21.51	21.16	21.42
FeO	25.21	27.21	25.44	25.94	25.91	25.17	25.06
MgO	6.91	6.50	7.22	4.56	5.68	3.81	5.71
CaO	5.69	3.27	5.10	8.05	7.58	10.26	8.57
MnO	1.70	3.11	1.97	1.58	0.71	1.15	0.43
Total	98.88	98.96	99.07	99.05	99.42	99.38	99.40
atoms per formula unit							
Si	2.989	2.981	2.981	2.975	2.975	2.981	2.981
Ti	0.004	0.003	0.004	0.004	0.007	0.008	0.008
Al	1.969	1.983	1.969	1.994	1.990	1.973	1.977
Fe	1.657	1.804	1.670	1.721	1.701	1.665	1.641
Mg	0.810	0.768	0.845	0.540	0.664	0.449	0.666
Ca	0.479	0.278	0.429	0.684	0.637	0.869	0.720
Mn	0.113	0.209	0.131	0.106	0.047	0.077	0.029
Sum	8.022	8.025	8.030	8.024	8.022	8.024	8.022
No. analyses	10	7	7	4	11	5	15

*Analyses were taken at the center of core garnets to allow comparison of the same area at the center of every garnet.

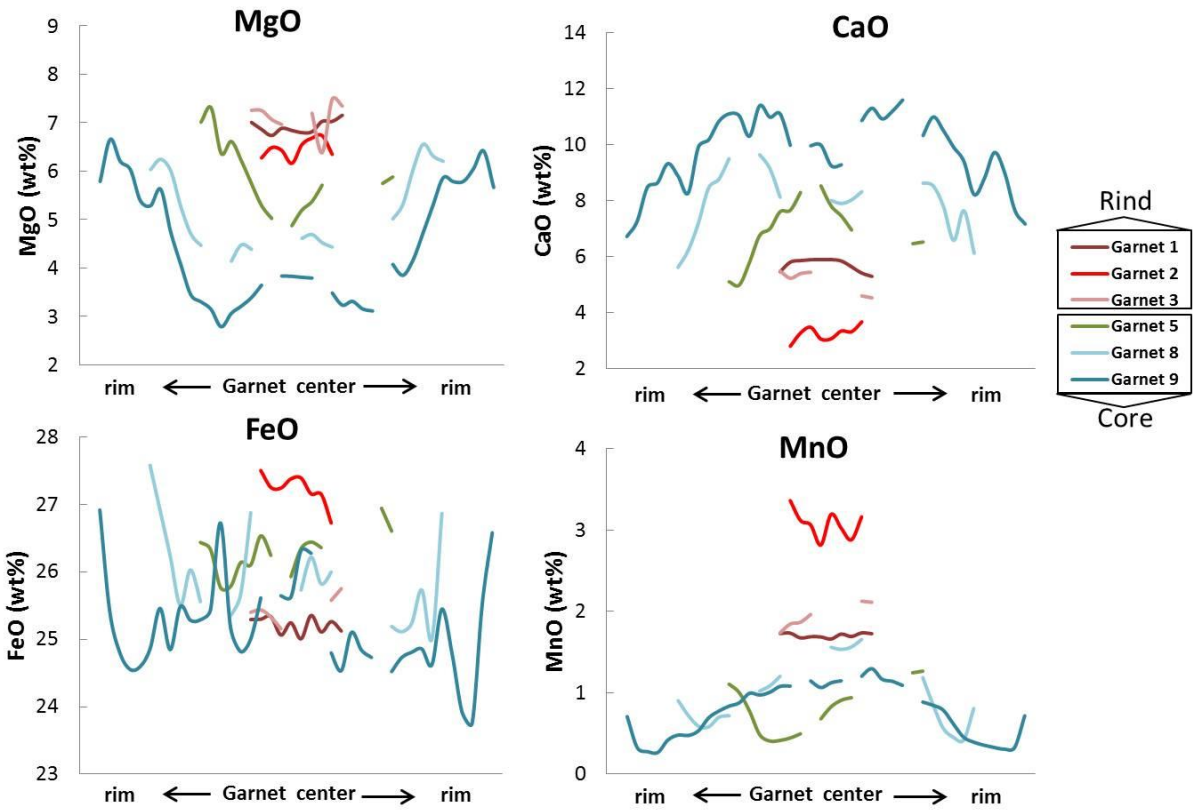

Figure 13: Compositions of MgO, CaO, FeO, and MnO vs. distance across garnet. Graphs were made by plotting all garnet centers at 0, with space increments varying for each garnet (distance is not to scale on x axis in order to see variability in rind garnet compositions). All core garnets contain higher contents of MnO and CaO in the garnet center than their rims. Magnesium oxide compositions increase towards the outer edges of the core garnets. Iron oxide compositions remain relatively constant, with a slight increase in compositions at the core garnet edges. Overall, rind garnets are enriched in MnO and MgO and depleted in CaO relative to core garnets. Large variations in compositions along a single garnet traverse may reflect points adjacent to garnet inclusions. Points with total wt% averages below 98% and above 102% were removed, as well as points with >3.5wt% TiO_2.

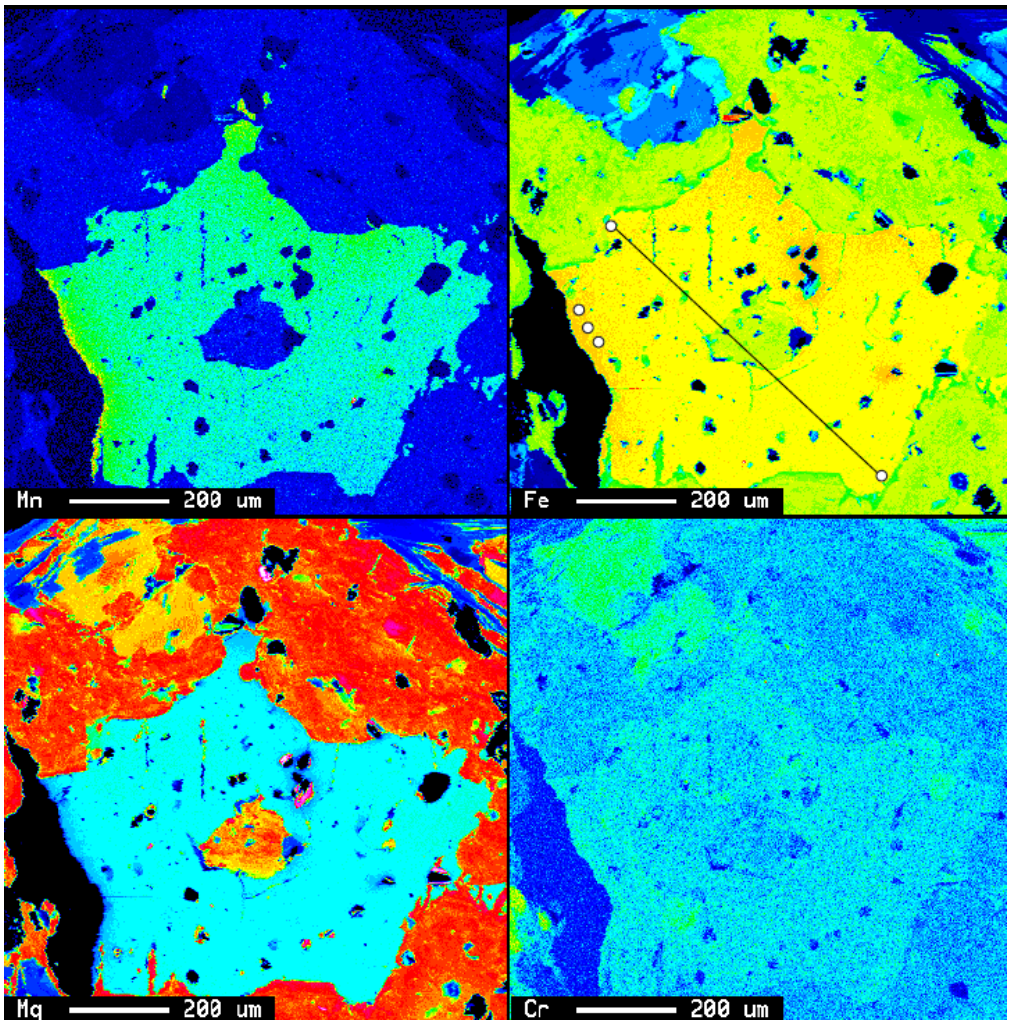

Figure 14: X-ray map of rind garnet #3 (A10-3 traverse). Black line and points on Fe map show EPMA data points.

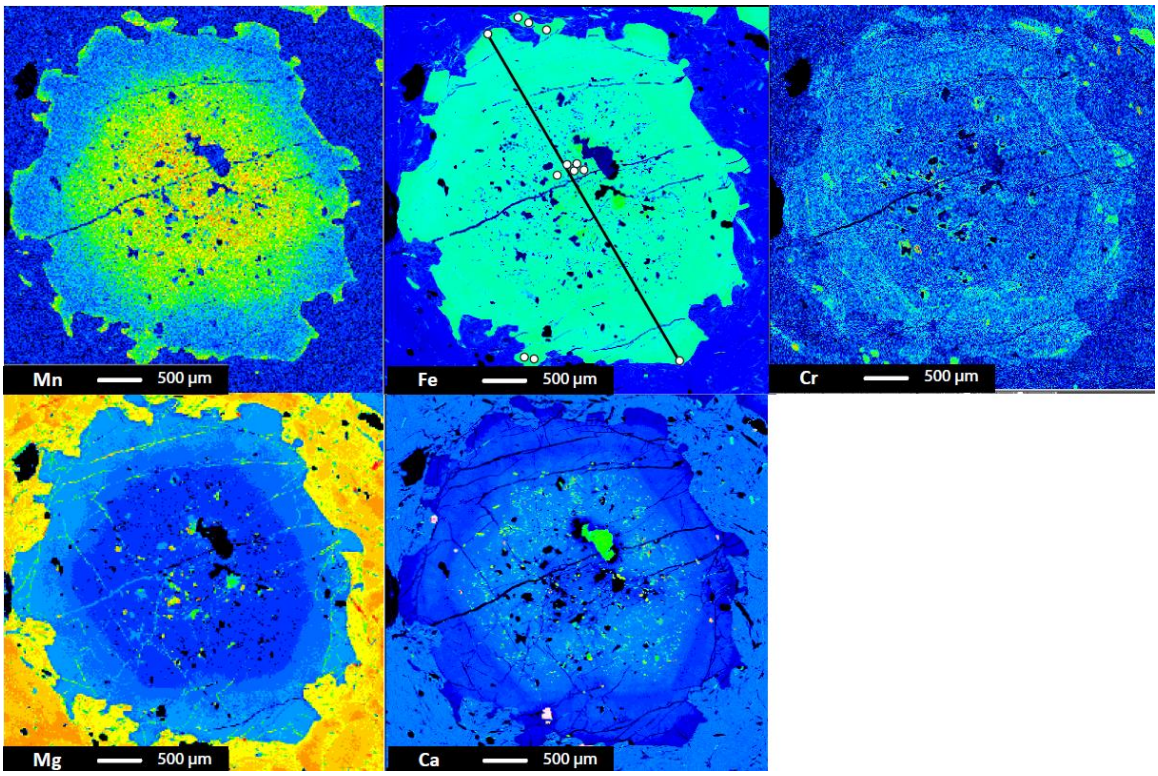

Figure 15: X-ray map of core garnet #9 (A10-3 traverse). Black line and points on Fe map show EPMA data points.

Chapter 7: Major- and minor-element bulk-rock concentrations

7.1 Catalina Schist

7.1.1 Traverse A10-3, amphibolite grade

Whole-rock major and trace element compositions of block core and rind measured by XRF for the A10-3 traverse can be found in Table 6. Though this particular traverse does not include adjacent matrix, amphibolite grade matrix XRF data from Bebout and Barton (2002) are included for comparison in Table 7. The rind contains higher concentrations of SiO_2, K_2O, MgO, Ba, Ni, and Cr, relative to the block core, and is depleted in FeO, Fe_2O_3, Al_2O_3, TiO_2, CaO, Na_2O, Zr and Sr. The ultramafic matrix contains greater contents of SiO_2, Cr, Ni, and MgO, but lower Ba and K_2O, compared to both core and rind (Figures 16a, b). The patterns of most major and minor element data as a function of distance from the contact are irregular. Concentrations of Cr, MgO and Ni are highest at ~2.5cm and decrease towards the edge of the rind, with a slight increase in concentration at 11.1cm.

Table 6: Bulk-rock compositions for the A10-3 traverse.

	Block rind							Block core			
Sample	**r15**	**r13**	**r11**	**r9**	**r7**	**r5**	**r3**	**c1**	**c3**	**c5**	**c7**
Distance (cm)	15.1	13.1	11.1	8.2	6.2	4.2	2.5	-0.5	-2.5	-4.5	-6.5
SiO_2	52.73	59.03	52.35	50.54	55.82	53.45	50.63	42.84	42.86	42.38	41.60
TiO_2	1.27	1.15	1.25	1.38	0.97	0.70	0.52	2.58	2.52	2.92	2.60
Al_2O_3	11.53	10.13	12.07	11.86	10.53	10.61	8.93	14.55	13.98	14.04	14.88
Fe_2O_3	1.10	1.25	1.02	1.26	1.14	1.20	0.92	2.59	2.37	1.71	3.44
FeO	8.85	7.92	8.17	9.06	8.09	8.05	7.57	11.91	12.39	13.11	13.17
MnO	0.31	0.31	0.24	0.28	0.24	0.23	0.13	0.31	0.27	0.25	0.27
MgO	11.45	9.53	11.82	11.94	10.71	12.70	17.30	11.89	11.55	11.20	10.93
CaO	7.15	5.79	6.09	7.55	6.85	7.86	10.12	8.66	9.35	9.73	9.19
Na_2O	0.97	0.73	0.55	1.00	0.84	0.95	1.02	1.42	1.41	1.31	1.17
K_2O	1.97	1.74	2.68	2.01	2.01	1.86	0.75	0.53	0.32	0.23	0.20
P_2O_5	0.14	0.16	0.15	0.16	0.09	0.02	0.02	0.23	0.37	0.38	0.11
Cr (ppm)	523	475	555	533	606	718	1145	139	78	67	120
Ni (ppm)	261	260	377	288	279	356	650	146	69	36	56
Sr (ppm)	26	25	28	33	35	25	33	40	41	46	31
Zr (ppm)	92	85	91	98	82	83	48	120	99	124	118
Ba (ppm)	878	745	1258	831	1067	803	342	185	57	31	32
LOI	2.98	2.76	3.81	2.97	2.63	2.61	2.26	2.75	2.40	2.77	2.49
Total	100.45	100.50	100.20	100.01	99.92	100.24	100.17	100.26	99.79	100.03	100.05

Results are reported in wt% except where indicated otherwise. Distance is reported in cm from the core-rind contact. Samples labeled as “r” are rind samples, and samples labeled as “c” are core samples.

Table 7: Amphibolite-grade mélange matrix bulk-rock compositions (Bebout and Barton, 2002; King, unpublished data).

Sample	6-4-6*	6-4-11*	6-3-7	6-3-9	6-3-21	6-3-22	6-3-31c	6-3-32	6-3-33	6-3-35a	6-3-60	6-4-3
SiO_2	33.17	54.43	55.17	40.24	53.04	50.3	55.95	56.01	47.97	60.18	48.37	60.31
TiO_2	0.05	0.05	0.2	0.07	0.56	0.37	0.03	0.05	0.09	0.05	0.04	0.07
Al_2O_3	14.03	2.84	5.59	7.57	7.97	8.89	2.58	2.89	6.55	1.15	3.37	1.18
Fe_2O_3T	6.60	5.95	6.37	5.62	7.64	6.07	5.74	7.33	8.36	6.07	8.81	2.33
MnO	0.05	0.07	0.1	0.07	0.13	0.13	0.16	0.23	0.19	0.14	0.15	0.08
MgO	32.64	28.28	22.3	35.82	19.74	20.72	32.22	29.28	27.95	27.89	32.52	25.39
CaO	0.27	1.96	7.17	0.53	3.97	7.40	1.10	0.32	3.82	0.06	0.09	9.38
Na_2O	0.04	0.13	0.89	0.03	0.33	0.96	0.02	0.01	b.d.	0.01	0.07	0.03
K_2O	0.01	0.02	0.15	0.01	0.44	0.52	0.02	0.03	0.04	0.01	0.02	0.07
Cr (ppm)	3244	2884	1324	5672	1259	817	2356	2559	1603	939	2626	584
Ni (ppm)	2659	2608	893	1498	800	513	1769	1621	1213	1116	1525	872
Sr (ppm)	4	7	n.d.	10	n.d.	b.d.	16	10	n.d.	n.d.	12	93
Zr (ppm)	13	5	n.d.	5	n.d.	b.d.	5	5	n.d.	90	5	34
Ba (ppm)	5	81	n.d.	4	n.d.	b.d.	131	58	n.d.	n.d.	180	17
LOI	13	6	1.4	9.5	5.9	2.9	2.1	4.1	4.4	3.9	5.9	0.6
Total	99.48	99.15	99.56	100.17	99.89	98.41	100.34	100.66	99.68	99.69	99.75	99.56

Samples were taken from the mélange dominated amphibolite facies (highlighted in Fig. 1).
*Sample data are from King, unpublished. All other data are from Bebout and Barton (2002).
n.d. = no data. b.d. = below detection limit. Results are in wt% except where otherwise noted.

7.1.2 Traverse A12-A4, amphibolite grade

Whole-rock major and trace element compositions measured by XRF of block core and rind for the A12-4 traverse can be found in Table 8. The rind contains, on average, higher contents of SiO_2, K_2O, Ba, MgO, Ni, and Cr, relative to the block core, and has lower contents of FeO, Fe_2O_3, Al_2O_3, TiO_2, CaO, and Sr. The ultramafic matrix contains greater contents of Cr, Ni, and MgO, but generally lower Sr, Ba and K_2O, compared to both core and rind. When comparing concentration vs. distance along the core-rind contact, some elements appear to co-vary (Fig. 17). Sample r3 has the highest Cr and Ni concentrations at ~3.75cm from the core-rind contact. Magnesium oxide compositions also increase slightly at ~3.75cm.

Table 8: Bulk-rock compositions for the A12-A4 traverse.

	Block rind							Block core					
Sample	**r7**	**r6**	**r5**	**r4**	**r3**	**r2**	**r1**	**c1**	**c2**	**c3**	**c4**	**c5**	**c6**
Distance (cm)	11	9	7.5	6	4.5	3	1.5	-0.75	-2.25	-5.75	-7.25	-8.75	-10.25
SiO_2	58.35	54.40	57.48	51.38	49.34	50.33	45.97	43.61	44.43	43.89	43.35	45.69	44.43
TiO_2	0.56	0.69	0.65	0.63	0.62	0.82	2.28	2.58	2.44	2.67	2.19	2.20	2.84
Al_2O_3	10.17	11.27	10.26	11.66	11.92	11.70	13.27	15.03	15.15	14.70	15.63	14.17	14.03
Fe_2O_3T	9.58	10.40	9.83	11.27	12.01	11.92	12.77	16.38	16.85	16.23	16.84	14.65	14.55
MnO	0.16	0.17	0.17	0.18	0.20	0.19	0.21	0.29	0.33	0.29	0.47	0.36	0.25
MgO	11.72	12.86	12.07	13.24	14.71	14.10	13.47	11.02	10.38	10.23	11.11	11.45	11.48
CaO	7.79	8.64	7.96	9.13	9.47	9.16	9.71	9.14	8.86	9.48	9.11	9.58	9.74
Na_2O	1.40	1.57	1.43	1.65	1.58	1.53	1.78	1.49	1.32	1.35	1.35	1.46	1.64
K_2O	0.48	0.36	0.39	0.34	0.37	0.39	0.36	0.32	0.28	0.24	0.21	0.22	0.26
P_2O_5	0.02	0.02	0.02	0.02	0.02	0.02	0.04	0.23	0.24	0.27	0.23	0.47	0.17
Cr (ppm)	843	888	905	923	1068	910	501	718	606	533	555	475	523
Ni (ppm)	352	350	335	350	389	325	246	100	92	84	90	119	90
Sr (ppm)	42	46	43	50	47	46	51	53	54	64	50	62	58
Zr (ppm)	112	180	135	221	90	125	225	114	106	108	128	110	114
Ba (ppm)	386	87	115	64	103	139	99	90	92	55	41	63	53
LOI	1.91	2.03	2.01	2.17	2.45	2.42	2.04	2.06	1.68	1.72	1.65	1.66	1.83
Total	100.23	100.38	100.26	99.50	100.24	100.16	99.86	100.09	100.28	99.35	100.49	100.25	99.39

Results are reported in wt% except where indicated otherwise. Distance is reported in cm from the core-rind contact. Samples labeled as “r” are rind samples, and samples labeled as “c” are core samples.

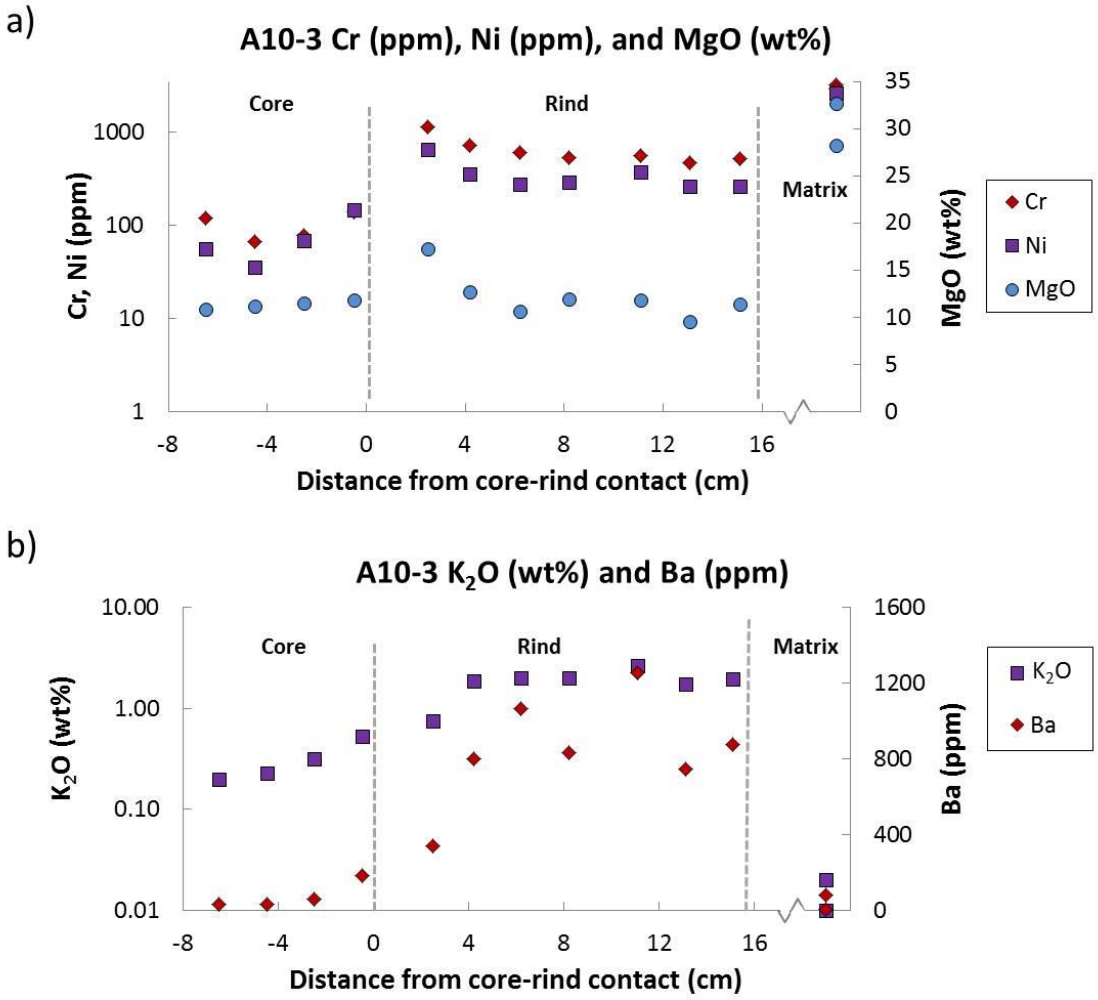

Figure 16: A10-3 bulk-rock and trace element chemistry vs. distance. a) Concentrations of Ni, Cr, (plotted on a logarithmic scale) and MgO vs. distance from the core-rind contact for the A10-3 traverse. Nickel and Cr have elevated concentrations in the rind relative to the core with the highest concentrations near the core-rind contact. b) Compositions of K_2O (plotted on a logarithmic scale) and Ba vs. distance from the core-rind contact for the A10-3 traverse. Compositions of K_2O and Ba are elevated in the rind relative to both core and matrix.

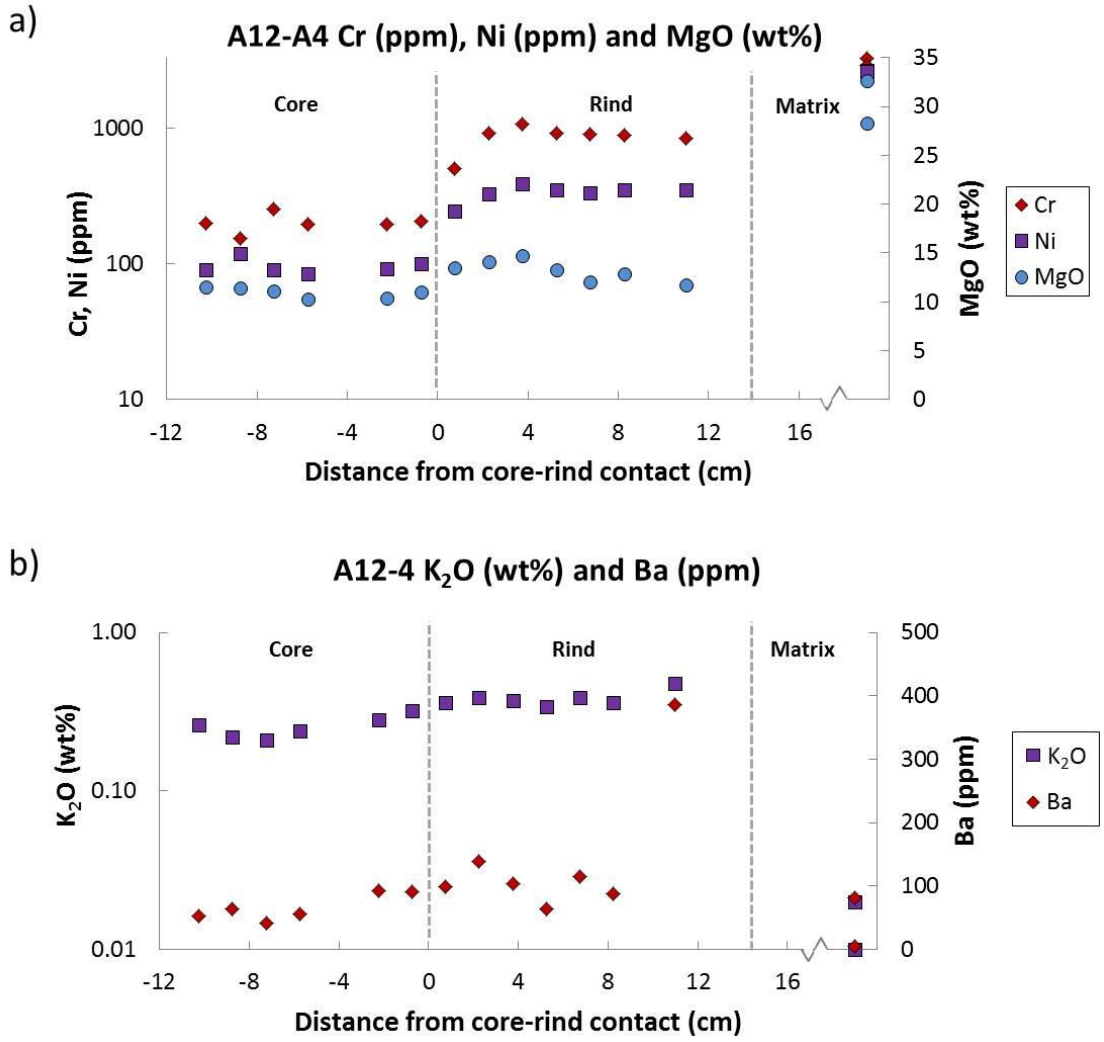

Figure 17: A12-A4 bulk-rock and trace element chemistry vs. distance. a) Concentrations of Ni, Cr, (plotted on a logarithmic scale) and MgO vs. distance from the core-rind contact for the A12-4 traverse. Ni and Cr concentrations are elevated in the rind relative to the core with the highest concentrations at 3.75 cm. b) Concentrations of Ba and K_2O (plotted on a logarithmic scale) vs. distance from the core-rind contact for the A10-3 traverse. Barium and K_2O have elevated concentrations in the rind relative to the core and mélange matrix.

7.1.3 Lawsonite-albite and lawsonite-blueschist traverses

Bulk-rock major and trace element concentrations measured by XRF for representative lawsonite-albite and lawsonite-blueschist facies are shown in Table 9. Nickel and Cr concentrations for the lawsonite-albite facies samples are elevated in the reaction rind relative to the core. Nickel and Cr concentrations in the rind for the lawsonite-blueschist traverse fall between mélange matrix and core sample concentrations (Fig. 18). Barium and K_2O contents in the rind are lower than core and matrix compositions for the lawsonite-albite samples (Fig. 18). The lawsonite-blueschist samples have decreasing Ba and K_2O from the core to the mélange matrix.

Table 9: Bulk-rock compositions for lawsonite-albite and lawsonite-blueschist samples.

Sample	LA10-2A core	LA10-3B core	LA10-3F rind	LA10-2C rind	LB10-1A core	LB10-1B core	LB10-1C matrix
SiO_2	45.13	45.39	40.12	56.35	38.07	51.78	51.59
TiO_2	3.48	2.14	1.77	0.03	1.41	1.03	0.54
Al_2O_3	17.62	24.01	12.81	2.43	17.61	14.81	7.22
Fe_2O_3T	13.83	11.54	13.49	7.03	11.86	7.44	8.54
MnO	0.18	0.17	0.27	0.12	0.16	0.13	0.15
MgO	9.14	4.61	25.40	25.48	9.08	12.32	22.01
CaO	3.90	6.75	5.37	7.58	16.50	6.93	8.04
Na_2O	4.66	2.49	0.25	0.22	2.68	4.24	1.13
K_2O	0.41	2.47	0.02	0.01	1.97	1.02	0.45
P_2O_5	0.57	0.33	0.29	0.01	0.27	0.20	0.07
Cr (ppm)	193	225	1381	2592	237	410	1318
Ni (ppm)	90	106	769	1418	95	304	980
Sr (ppm)	106	290	27	39	662	268	22
Zr (ppm)	218	150	31	15	92	54	55
Ba (ppm)	116	827	21	8	691	337	99
LOI	6.26	7.21	9.17	4.13	13.08	6.52	5.46
Total	98.92	99.90	99.79	99.26	99.61	99.90	99.74

Results are reported in wt% except where indicated otherwise. (LA = lawsonite-albite; LB = lawsonite-blueschist).

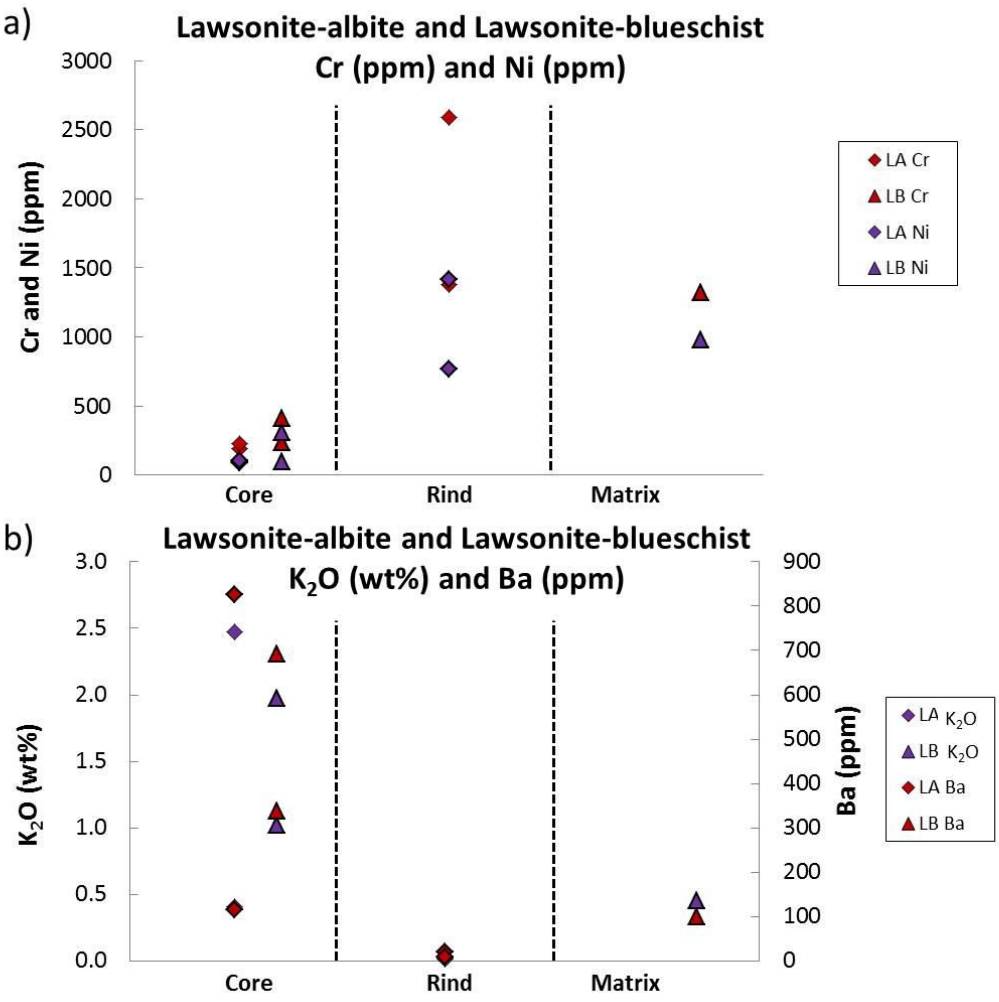

Figure 18: Lawsonite-albite and lawsonite-blueschist bulk-rock and trace element chemistry. a) Concentrations of Cr and Ni, and b) contents of Ba and K_2O for core, rind and matrix lawsonite-albite (LA) and lawsonite-blueschist (LB) representative samples.

7.2 Attic-Cycladic Complex, Syros

7.2.1 Lia Beach traverse

Bulk-rock major and trace element compositions for the Lia Beach traverse are taken from Miller et al. (2009) (Table 10). The meta-tuffite (Zone I) contains the highest contents of SiO_2 relative to the other zones. The metasomatic reaction zone has significantly higher CaO contents than the other 3 zones. The chlorite-schist blackwall zone has elevated Al_2O_3, MgO, Cr, and Ni compared to the meta-tuffite (Fig. 19a). The serpentinite contains the highest MgO, Cr and Ni contents. Contents of Ba and K_2O in the chlorite-schist blackwall are considerably lower than in the meta-tuffite, and slightly higher than in the serpentinite (Fig. 20a).

7.2.2 Stavros traverse

Bulk-rock major and trace element compositions for the Stavros traverse are from Marschall (unpublished; Table 11). The chlorite-schist blackwall (Zone D) has lower contents of SiO_2, CaO, Na_2O, and Ni. Zone C ("metasomatic reaction zone") has the highest contents of SiO_2, Ba, and Sr. Zone B ("metasomatic reaction zone") has the highest composition of Fe_2O_3 and Cr. The eclogite block has the highest Al_2O_3, CaO, and MnO contents, and the lowest MgO contents. Nickel concentrations are highest in the serpentinites and vary in the intermediate zones, with concentrations below the detection limit in the eclogite block (Fig. 19b). Chromium concentrations decrease from the chlorite-schist blackwall zone to the eclogite block (Fig. 19b). Magnesium oxide compositions in the serpentinite and chlorite-schist blackwall are more than double the

MgO contents in the glaucophane-, garnet-, and omphacite-rich zones (Fig. 19b). Potassium oxide contents remain relatively constant across the serpentinite, chlorite-schist blackwall, and metasomatic reaction zones, with concentrations more than doubling in the eclogite block. Barium concentrations also remain relatively constant across the entire length of the traverse with no salient compositional trend (Fig. 20b).

Table 10: Lia Beach traverse bulk-rock compositions. Data are from Miller et al. (2009), and Marschall (unpublished)

	Meta-tuffite		Metasomatic reaction zone						Chlorite-schist blackwall					Serpentinite			
Zone	Zone I		Zone II			Zone III			Zone IV					Zone V			
	PSIII	PSIII	PSIII	PSIII	PSIII	PSIII	PSI	PSIII	PSI	PSII	PSII	PSII	PSII	PSII	PSII	SY551	SY552
Sample	A7	A6	A4.2	A3	A2.2	A2.1	10.1	A2.0	11.1	12.0	13.2	13.4	14.0	15.2	16.0		
Distance from serp./blackwall contact (cm)	-693	-447	-393	-339	-312	-285	-280	-258	-226	-199	-74	-37	-10	44	71	5000	10000
SiO_2	50.17	49.33	46.03	48.26	48.00	43.06	46.49	38.54	27.17	28.14	30.09	31.01	31.38	40.23	40.38	40.94	40.58
TiO_2	1.29	1.52	1.39	1.71	1.30	1.04	1.34	1.30	2.08	1.84	1.50	1.25	1.08	0.02	0.06	0.07	0.03
Al_2O_3	14.87	13.60	14.70	13.56	14.07	15.02	14.12	16.19	18.35	18.42	17.84	15.12	14.30	1.39	2.15	2.71	2.87
Fe_2O_3T	11.88	15.05	13.59	13.32	12.93	13.21	8.66	14.41	17.40	11.64	9.59	8.47	8.26	10.31	7.62	7.69	8.33
MnO	0.17	0.22	0.15	0.16	0.15	0.17	0.15	0.18	0.21	0.14	0.10	0.07	0.06	0.13	0.09	0.10	0.09
MgO	6.93	7.15	7.47	7.88	7.51	7.75	10.01	10.71	20.94	26.76	30.79	31.35	32.80	34.54	36.95	36.71	36.63
CaO	5.80	5.60	8.15	7.30	8.01	12.17	10.80	10.52	2.19	0.34	0.17	0.18	0.04	0.04	0.05	0.04	0.04
Na_2O	4.65	4.82	3.91	4.60	4.42	3.70	4.79	2.36	b.d.	0.03	b.d.	0.04	b.d.	0.01	b.d.	0.01	b.d.
K_2O	1.11	0.25	0.04	0.03	0.03	0.02	0.05	0.01	b.d.	b.d.	0.01	0.01	0.01	0.01	0.01	0.01	0.01
P_2O_5	0.15	0.11	0.11	0.10	0.09	0.05	0.03	0.03	0.03	0.26	0.12	0.13	0.01	0.01	0.01	0.01	0.01
Cr (ppm)	12.2	10.9	22.4	9.1	48.8	54.1	244.7	45.7	42.8	345.6	275.7	233.3	222.2	5208	2939	2463	2737
Ni (ppm)	10.8	10.2	18.3	14.5	19.9	32	119.6	42.9	42	193.8	166.7	194.4	657.9	2770	2319	2436	2593
Sr (ppm)	205	233	390	339	427	491	298	492	69	b.d.	5	2	4	b.d.	7	n.d.	n.d.
Zr (ppm)	98	43.2	44.9	46	101.4	121.9	122.8	87.5	84	163.9	137.2	109.4	108	5.6	6.2	n.d.	n.d.
Ba (ppm)	85.8	35.3	20	15.1	8.2	19.6	28.9	22	20	8.2	7.2	b.d.	2.3	0.5	7	n.d.	n.d.
LOI	2.03	1.69	2.72	2.32	2.29	3.21	2.79	4.95	11.61	11.18	9.68	11.90	11.93	11.27	11.80	11.36	11.29
Total	99.05	99.34	98.26	99.25	98.80	99.41	99.26	99.23	99.99	98.82	99.95	99.57	99.97	98.94	99.75	100.57	100.60

b.d. = below detection limit; n.d. = no data.

Table 11: Stavros traverse bulk-rock compositions. Data are from Marschall (unpublished).

	Serpentinite	Chlorite-schist blackwall	Metasomatic reaction zone										Eclogite block			
Zone	Zone E	Zone D	Zone C			Zone B							Zone A			
Sample	SY530	SY522-0	SY522-10	SY522-20	SY522-30	SY522-40	SY522-50	SY522-60	SY522-70	SY522-80	SY522-90	SY522-100	SY522-125	SY522-160	SY522-175	SY522-200
Distance from serp./blackwall contact (cm)	-300	0	10	20	30	40	50	60	70	80	90	100	125	160	175	200
SiO_2	45.71	38.10	47.72	47.95	47.41	45.19	44.07	46.39	45.69	46.28	44.28	46.18	45.31	48.91	46.76	48.54
TiO_2	0.01	3.32	5.72	5.08	3.55	6.83	7.41	4.91	6.18	6.50	6.24	6.04	6.91	4.82	5.00	2.09
Al_2O_3	3.17	12.57	12.47	13.43	14.57	11.39	10.27	12.12	11.10	10.73	11.19	11.60	15.63	13.81	15.44	21.17
Fe_2O_3T	9.39	14.78	15.75	15.28	15.64	18.00	19.14	18.05	18.42	17.73	19.87	17.00	14.71	14.24	14.76	10.37
MnO	0.14	0.25	0.27	0.22	0.22	0.25	0.27	0.33	0.24	0.22	0.27	0.25	0.35	0.21	0.28	0.18
MgO	32.17	21.22	6.90	6.07	5.43	6.48	7.08	5.59	6.14	6.41	6.76	6.22	4.17	5.65	4.38	3.82
CaO	0.03	4.42	6.32	7.54	8.89	8.67	8.21	8.76	8.52	8.12	8.57	8.88	9.15	7.31	8.01	6.89
Na_2O	0.00	0.67	4.54	4.56	4.15	3.35	2.88	3.75	3.56	3.63	2.67	3.54	3.55	4.31	3.88	4.49
K_2O	0.01	0.04	0.11	0.12	0.24	0.06	0.09	0.04	0.06	0.06	0.09	0.04	0.40	0.35	0.41	0.70
P_2O_5	0.01	0.12	0.09	0.08	0.47	0.12	0.05	0.37	0.08	0.11	0.06	0.04	0.04	0.05	0.07	0.13
Cr (ppm)	1935	b.d.	b.d.	b.d.	b.d.	8	28	3	8	6	18	8	b.d.	1	b.d.	b.d.
Ni (ppm)	1909	51	25	b.d.	1	2	15	b.d.	11	16	b.d.	b.d.	b.d.	b.d.	b.d.	b.d.
Sr (ppm)	n.d.	14	130	283	457	173	50	93	70	102	53	79	371	197	245	426
Zr (ppm)	n.d.	134	142	115	122	128	124	276	122	139	76	85	125	168	151	106
Ba (ppm)	n.d.	50	93	73	58	51	56	46	29	59	59	58	69	70	52	76
LOI	8.80	6.65	0.95	0.81	0.76	0.64	0.95	0.33	0.47	0.58	0.68	0.44	0.61	0.78	0.84	1.81
Total	100.13	102.14	100.89	101.19	101.41	101.02	100.46	100.68	100.49	100.40	100.70	100.26	100.90	100.48	99.87	100.25

b.d. = delow detection limit; n.d. = no data.

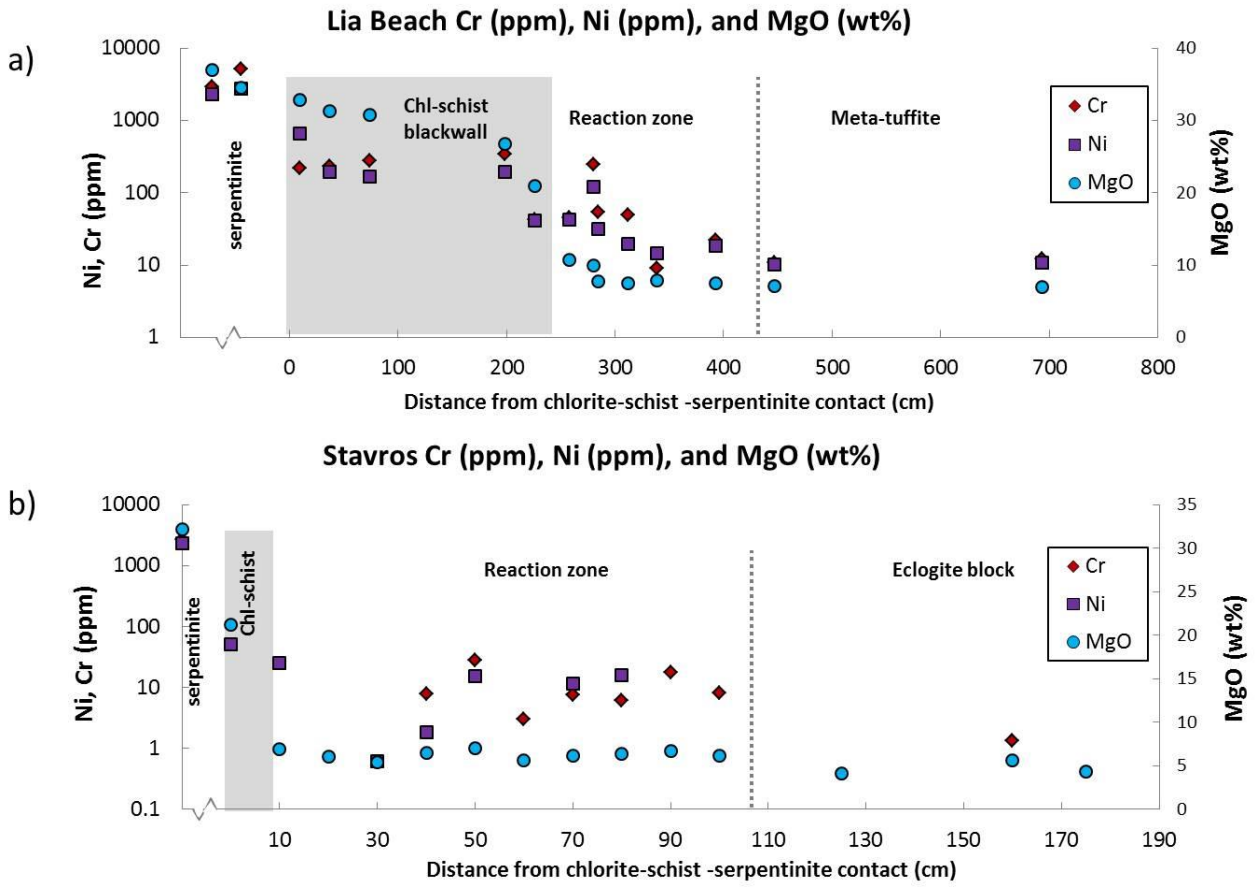

Figure 19: Lia Beach and Stavros Cr, Ni, and MgO compositions vs. distance. a) Concentrations of Ni, Cr (plotted on a logarithmic scale), and MgO vs. distance from the serpentinite-chlorite schist contact in the Lia Beach traverse. b) Concentration of Ni, Cr, (plotted on a logarithmic scale), and MgO vs. distance from the serpentinite-chlorite schist contact in the Stavros traverse. Concentrations increase from the meta-tuffite and eclogite block cores to the serpentinite.

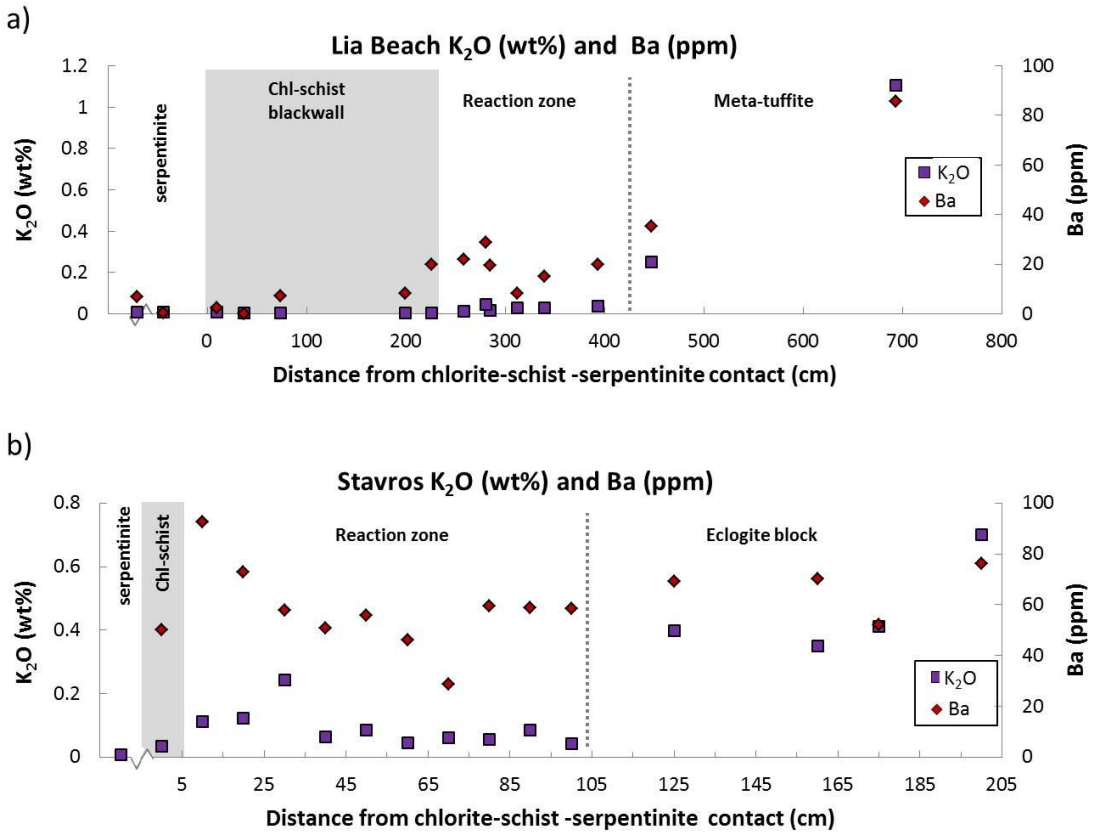

Figure 20: Lia Beach and Stavros Ba and K_2O compositions vs. distance. a) Contents of K_2O and Ba vs. distance from the chlorite-schist –serpentinite contact for the Lia Beach traverse. Contents of K_2O and Ba decrease from meta-tuffite to serpentinite. b) Contents of K_2O and Ba vs. distance from the chlorite-schist –serpentinite contact for the Stavros traverse. The content of K_2O decreases steadily from eclogite block to serpentinite. Barium concentrations fluctuate along the traverse, with the highest concentration in the metasomatic reaction zone (Zone C).

Chapter 8: Highly siderophile element data

8.1 Catalina Schist

8.1.1 Traverse A10-3

Highly siderophile element data for the Catalina Schist traverses can be found in Table 12. Osmium, Ir, and Ru concentrations of A10-3 rind samples plot in between Os, Ir, and Ru concentrations of core and matrix samples (Table 12; Fig. 21a). Osmium concentrations range from 0.025 to 0.106 ppb in the block core and from 0.512 to 1.66 ppb in the reaction rind. Iridium concentrations range from 0.002 to 0.013 ppb in the block core and from 0.325 to 1.15 ppb in the reaction rind. Ruthenium concentrations range from 0.039 to 0.205 ppb in the block core and from 0.656 to 2.11 ppb in the reaction rind. The maximum Os and Ir concentrations and second highest Ru concentration in the rind occur in sample A10-3B-R3, at ~2.5 cm distance from the core-rind contact (Fig. 21a). Two mélange samples analyzed have Os concentrations of 2.47 and 2.58 ppb, Ir concentrations of 2.13 to 2.15 ppb, and Ru concentrations of 5.09 to 5.12 ppb. Initial $^{187}Os/^{188}Os$ ratios in the core range from 0.3676 to 1.270. Initial $^{187}Os/^{188}Os$ ratios in the reaction rind range from 0.1400 to 0.1847 (Fig. 22). Initial $^{187}Os/^{188}Os$ ratios in two mélange samples analyzed are the same within error, averaging 0.1201. The minimum initial $^{187}Os/^{188}Os$ ratio also occurs at ~2.5cm distance from the core-rind contact. Rhenium concentrations are highest in the core and lowest in the rind, with matrix concentrations overlapping with core samples (Table 12, Fig. 23).

8.1.2 Traverse A12-4

Osmium, Ir, and Ru concentrations of A12-A4 rind samples plot in between Os, Ir, and Ru concentrations of core and matrix samples (Table 12; Fig. 21b). Osmium concentrations in the block core range from 0.005 to 0.118 ppb (Fig. 21b), and from 0.356 to 2.96 ppb in the reaction rind. Iridium concentrations in the block core range from 0.001 to 0.028 ppb (Fig. 21b), and from 0.221 to 1.78 ppb in the reaction rind. Ruthenium concentrations in the block core range from 0.005 to 0.086 ppb (Fig. 21b), and from 0.500 to 4.57 ppb in the reaction rind. The maximum Os, Ir, and Ru concentrations in the reaction rind all occur in sample A12-A4-R3, at ~3.75 cm from the core-rind contact. Initial $^{187}Os/^{188}Os$ ratios in the core range from 0.4943 to 0.2512. Initial $^{187}Os/^{188}Os$ ratios in the reaction rind range from 0.1301 to 0.2512, with the minimum initial $^{187}Os/^{188}Os$ ratio also occurring in sample A12-A4-R3. Rhenium, Pd, and Pt concentrations of rind samples fall between core and matrix values, with the exception of some variation in Pd concentrations (Table 12; Fig. 24).

Table 12: HSE concentrations, $^{187}Os/^{188}Os$, $^{187}Re/^{188}Os$, and $^{187}Os/^{188}Os_i$ for Catalina Schist samples.

Sample	type	Sample wt (g)	Re (ppb)	Os (ppb)	$^{187}Os/^{188}Os$	2σ	$^{187}Re/^{188}Os$	$^{187}Os/^{188}Os_i$*	2σ	Pd (ppb)	Pt (ppb)	Ru (ppb)	Ir (ppb)
Amphibolite grade traverse: A10-3													
A10-3C C1	core	2.46	0.664	0.106	0.4276	0.0012	31.43	0.3676	0.0013	0.267	0.363	0.057	0.013
A10-3C C5	core	2.47	2.033	0.025	2.227	0.0060	501.4	1.270	0.0086	0.090	0.019	0.205	0.002
A10-3C C7	core	2.52	0.739	0.062	0.6491	0.0020	61.59	0.5315	0.0025	0.125	0.018	0.039	0.007
A10-3C-R1	rind	1.87	0.236	0.912	0.1445	0.0001	1.250	0.1421	0.0002	0.627	1.06	2.11	0.750
A10-3C-R2	rind	1.89	0.088	1.16	0.1408	0.0001	0.3681	0.1400	0.0001	0.506	1.95	1.46	0.991
A10-3B-R3	rind	1.99	0.158	1.66	0.1336	0.0001	0.4603	0.1327	0.0001	0.420	1.82	1.91	1.15
A10-3B-R5	rind	2.04	0.230	1.00	0.1517	0.0002	1.112	0.1496	0.0002	0.761	1.85	1.44	0.738
A10-3B-R7	rind	2.01	0.254	0.871	0.1596	0.0001	1.409	0.1569	0.0001	1.27	1.14	1.02	0.406
A10-3A-R9	rind	1.98	0.235	0.543	0.1708	0.0003	2.097	0.1668	0.0004	0.878	1.31	0.798	0.378
A10-3A-R11	rind	2.00	0.091	0.636	0.1458	0.0001	0.6907	0.1445	0.0002	0.423	0.853	0.834	0.379
A10-3A-R13	rind	1.96	0.103	0.512	0.1866	0.0005	0.9798	0.1847	0.0006	1.17	1.56	0.656	0.325
A10-3A-R15	rind	1.94	0.066	0.559	0.1760	0.0002	0.5709	0.1749	0.0002	0.685	1.32	0.751	0.505
Amphibolite grade traverse: A12-A4													
A12-A4-C1	core	2.05	0.017	0.005	0.9109	0.2395	18.95	0.8747	0.2406	0.083	0.033	0.022	0.001
C1 duplicate		2.06	0.016	0.006	0.7694	0.2103	14.21	0.7423	0.2113	0.182	0.210	0.005	0.003
A12-A4-C3	core	1.98	0.008	0.006	0.9013	0.1981	8.081	0.8859	0.1986	0.101	b.d.❖	0.008	0.003
A12-A4-C5	core	2.05	0.037	0.118	0.4973	0.0012	1.571	0.4943	0.0013	11.6	b.d.❖	0.086	0.028
A12-A4-R1	rind	1/52	0.622	0.356	0.2676	0.0006	8.580	0.2512	0.0007	1.42	1.93	0.500	0.221
A13-A4-R2	rind	1.53	0.833	1.22	0.1570	0.0001	3.316	0.1506	0.0001	5.39	0.720	2.045	0.923
A12-A4-R3	rind	1.63	1.30	2.96	0.1341	0.0001	2.108	0.1301	0.0000	2.04	2.70	4.57	1.78
R3 duplicate		2.28	0.692	1.57	0.1409	0.0001	2.089	0.1369	0.0001	1.71	1.63	2.71	1.15
A12-A4-R4	rind	1.46	0.412	1.18	0.1505	0.0001	1.693	0.1473	0.0001	1.64	0.400	1.93	1.01
A12-A4-R5	rind	1.71	0.279	0.945	0.1472	0.0001	1.427	0.1445	0.0001	1.74	2.24	1.71	0.944
A12-A4-R6	rind	1.52	0.405	1.58	0.1447	0.0001	1.242	0.1423	0.0001	1.40	0.545	2.49	1.17
A12-A4-R7	rind	1.73	0.204	0.785	0.1459	0.0002	1.254	0.1435	0.0003	0.801	1.46	1.52	0.953
Amphibolite grade mélange matrix													
6-4-6	matrix	2.04	1.18	2.47	0.1244	0.0001	2.298	0.1200	0.0001	1.17	3.01	5.09	2.15
6-4-11	matrix	2.02	1.22	2.69	0.1244	0.0001	2.182	0.1202	0.0001	1.50	3.73	5.12	2.13

Sample	type	Sample wt (g)	Re (ppb)	Os (ppb)	$^{187}Os/^{188}Os$	2σ	$^{187}Re/^{188}Os$	$^{187}Os/^{188}Os_i$*	2σ	Pd (ppb)	Pt (ppb)	Ru (ppb)	Ir (ppb)
Lawsonite-albite grade													
LA10-2A	core	2.20	0.066	0.017	0.2686	0.0335	19.29	0.2428	0.0353	0.073	0.145	0.057	0.010
LA10-2C	rind	1.92	0.038	1.541	0.1244	0.0001	0.1177	0.1242	0.0001	1.258	1.68	3.21	2.295
LA10-3B	core	1.99	0.009	0.012	0.3352	0.0552	3.685	0.3303	0.0555	0.109	0.103	0.035	0.011
LA10-3F	rind	1.73	0.014	0.250	0.1322	0.0004	0.2665	0.1317	0.0004	6.468	1.79	0.331	0.171
Lawsonite-blueschist grade													
LB10-1A	core	1.99	0.014	0.017	0.3374	0.0379	4.002	0.3320	0.0382	0.359	0.184	0.055	0.018
LB10-1B	core	1.72	0.134	0.045	0.3407	0.0064	14.93	0.3208	0.0069	0.380	0.337	0.083	0.038

*Ages used for initial $^{187}Os/^{188}Os$ calculations were 114.5 Ma for amphibolite grade samples and 97 Ma for lawsonite-albite and lawsonite-blueschist grade samples. External reproducibility for meteorite standards were within the following: Pt <1.4%, Ru < 0.8%, Re <5.0%, Ir <3.0%, Pd <7.0%.

⋆b.d. = below detection limit. Samples A12-A4-C3 and A12-A4-C5 had high Pt blanks, resulting in data being below the detection limit.

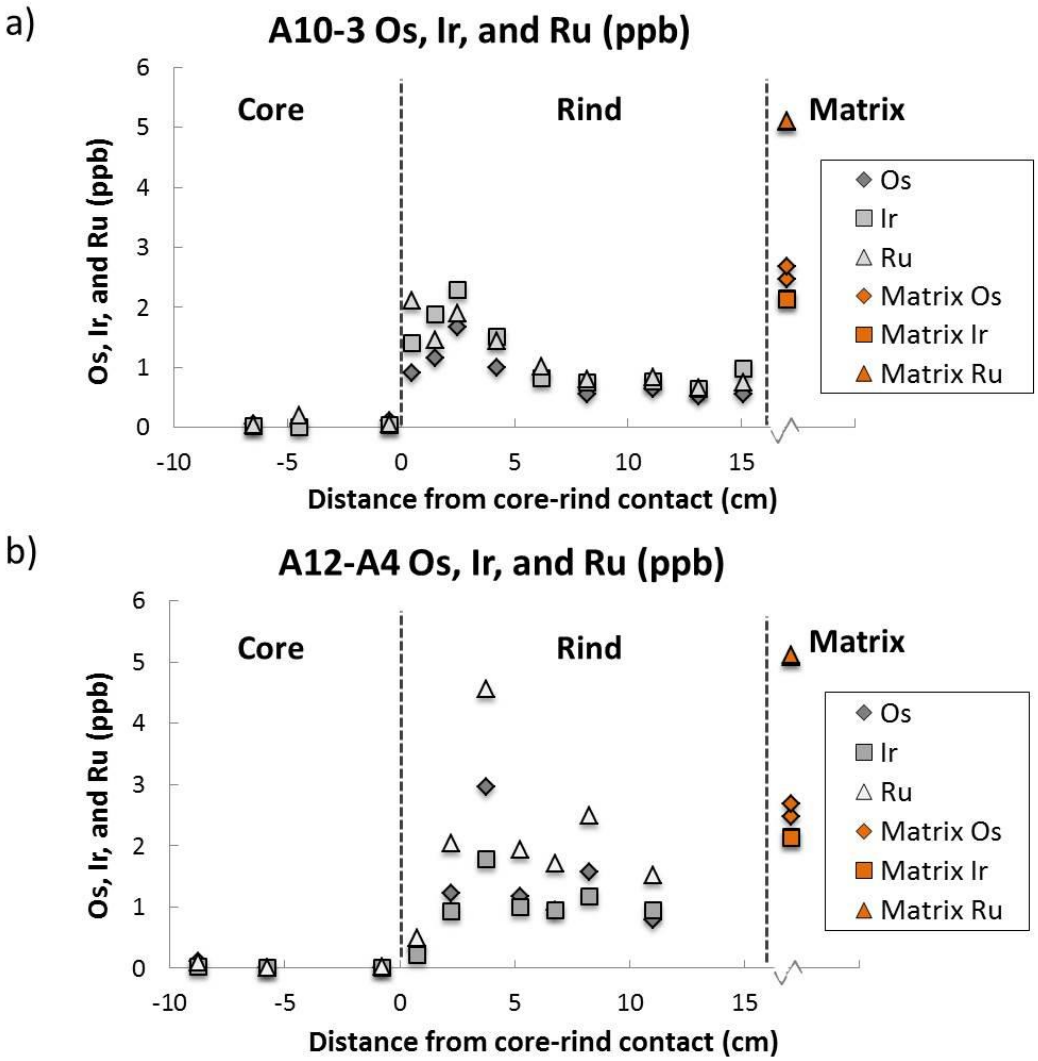

Figure 21: A10-3 and A12-A4 Os, Ir, and Ru vs. distance. a) Osmium, Ir, and Ru (ppb) vs. distance from the core-rind contact for the A10-3 traverse. b) Osmium, Ir, and Ru (ppb) vs. distance from the core-rind contact for the A12-A4 traverse. Matrix values are plotted at an arbitrary distance from the core-rind contact.

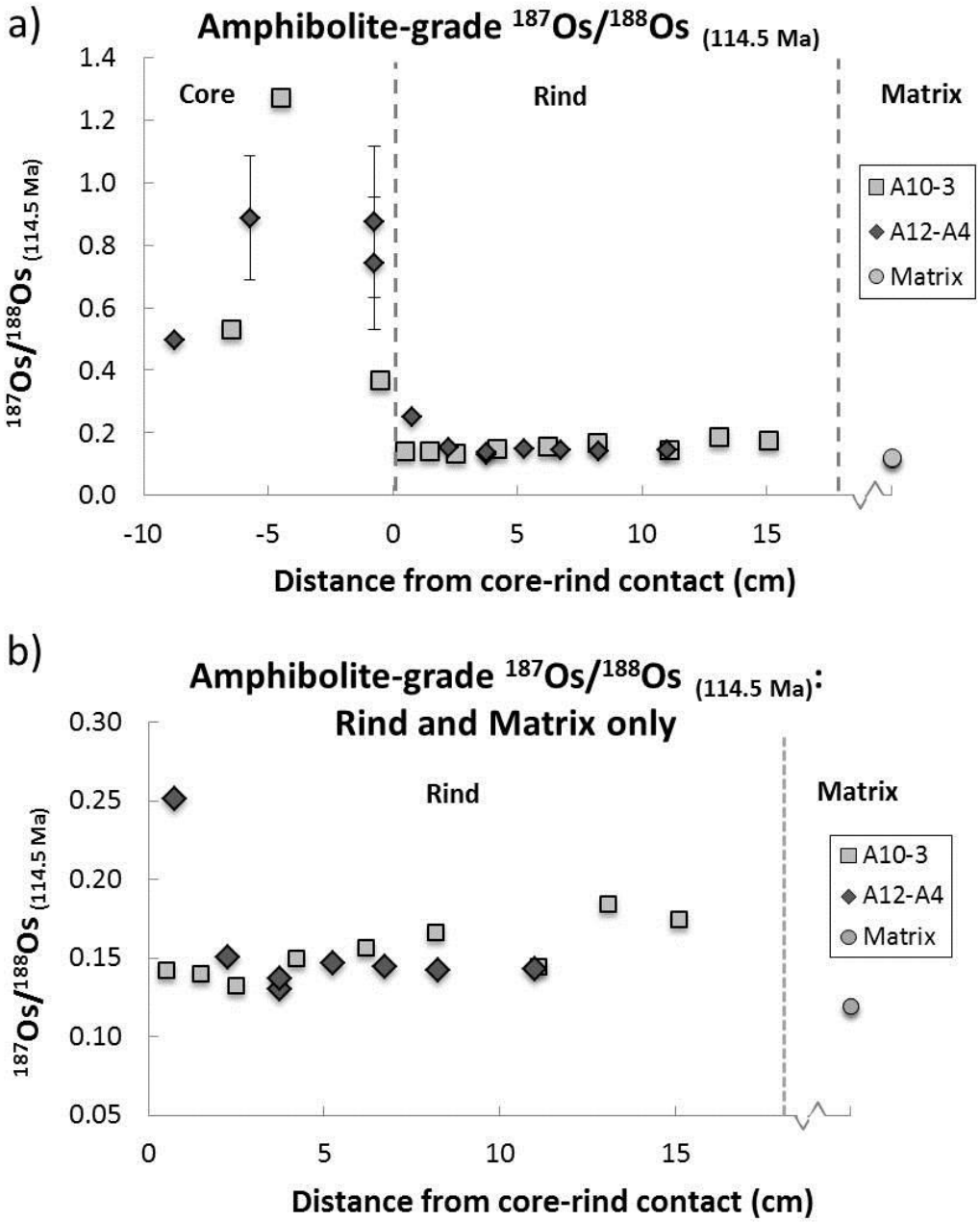

Figure 22: A10-3 and A12-A4 initial $^{187}Os/^{188}Os$ vs. distance. a) Initial $^{187}Os/^{188}Os$ vs. distance from the core-rind contact. b) Initial $^{187}Os/^{188}Os$ vs. distance from the core-rind contact showing rind and matrix values only. Matrix values are plotted at an arbitrary distance from the core-rind contact.

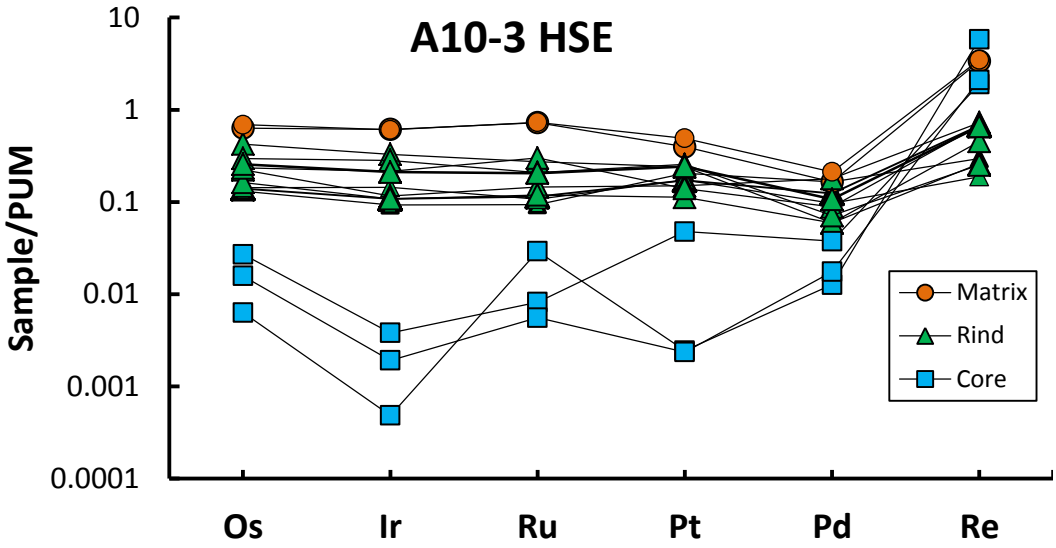

Figure 23: HSE concentrations for the A10-3 traverse normalized to Primitive Upper Mantle (PUM; values from Becker et al., 2006).

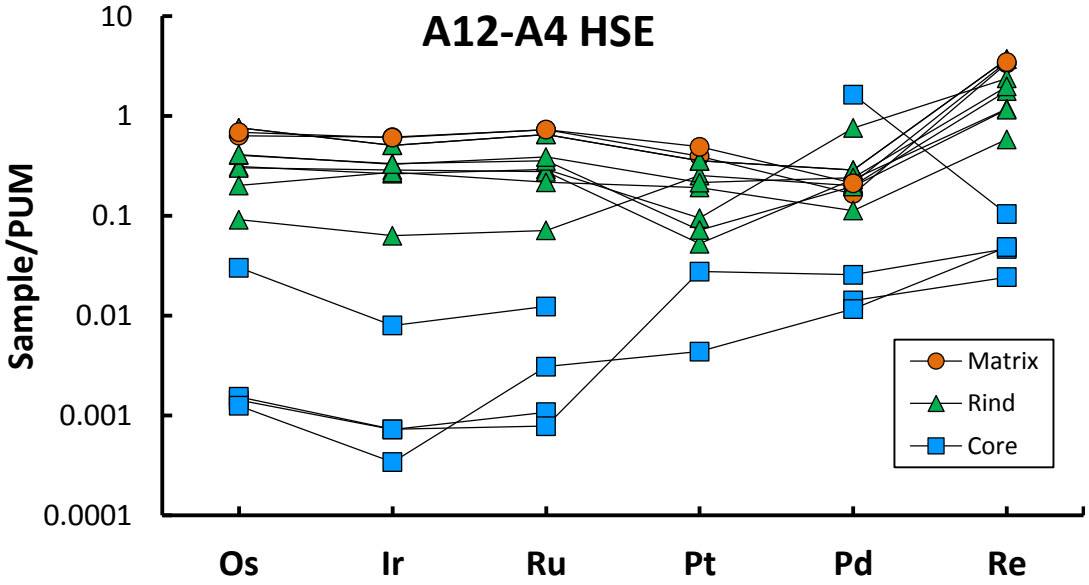

Figure 24: HSE concentrations for the A12-4 traverse normalized to PUM (values from Becker et al., 2006).

8.1.3 Lawsonite-albite and lawsonite-blueschist traverses

Osmium concentrations for the lawsonite-albite and lawsonite-blueschist cores range from 0.012 to 0.045 ppb with higher rind concentrations of 0.250 and 1.54 ppb (Fig. 25). Initial $^{187}Os/^{188}Os$ ratios for the cores were between 0.3320 and

0.2428 with lower rind ratios of 0.1317 and 0.1242 (Fig. 25). Iridium, Ru, Pt, and Pd are also enriched in rind samples relative to core and matrix samples (Fig. 26). Rhenium concentrations in the lawsonite-albite and lawsonite-blueschist samples do not show any distinct trends.

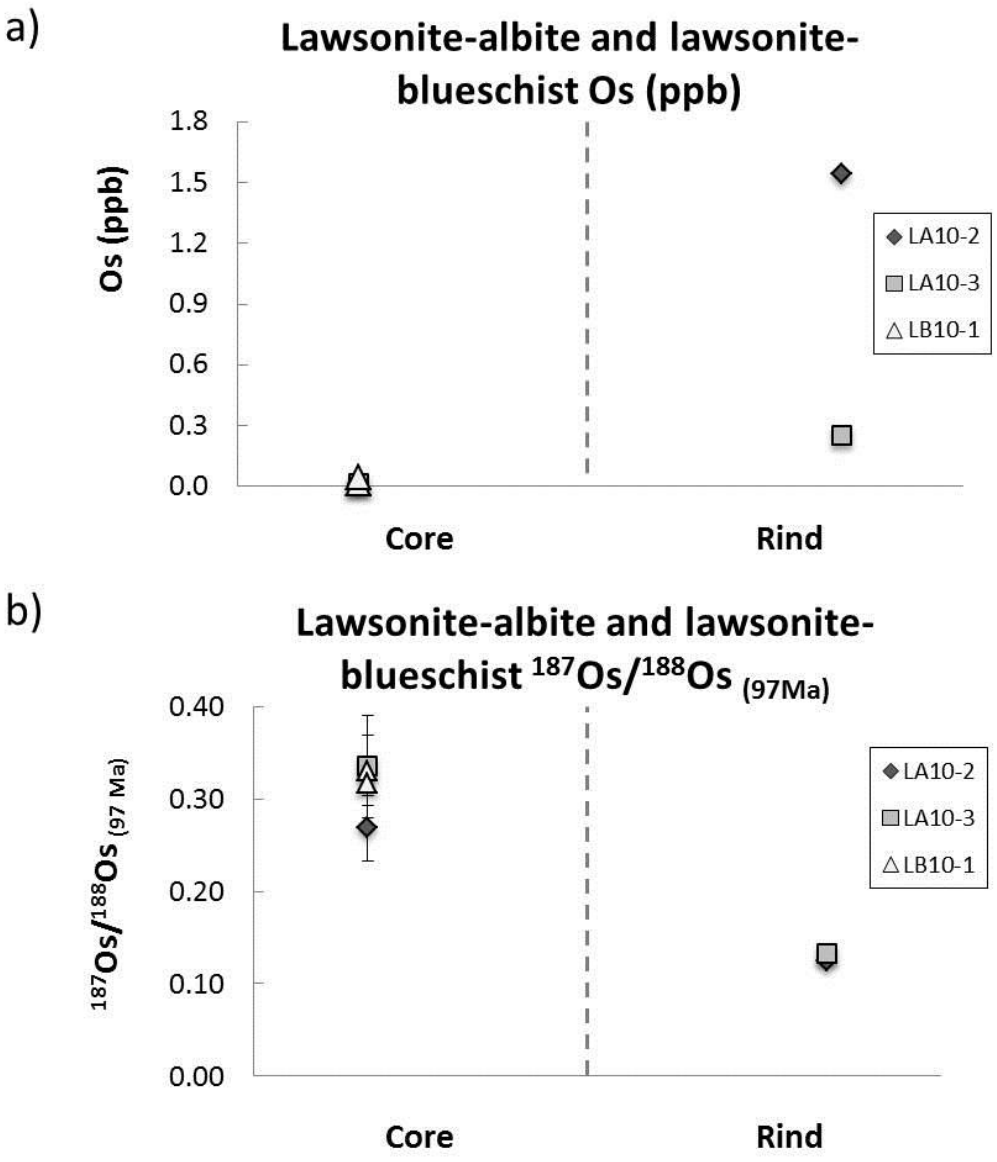

Figure 25: Os concentrations and isotopic data for lawsonite-albite and lawsonite-blueschist samples. a) Os concentrations for lawsonite-albite (LA) and lawsonite-blueschist (LB) core and rind samples. b) Initial $^{187}Os/^{188}Os$ ratios for paired rind and core samples.

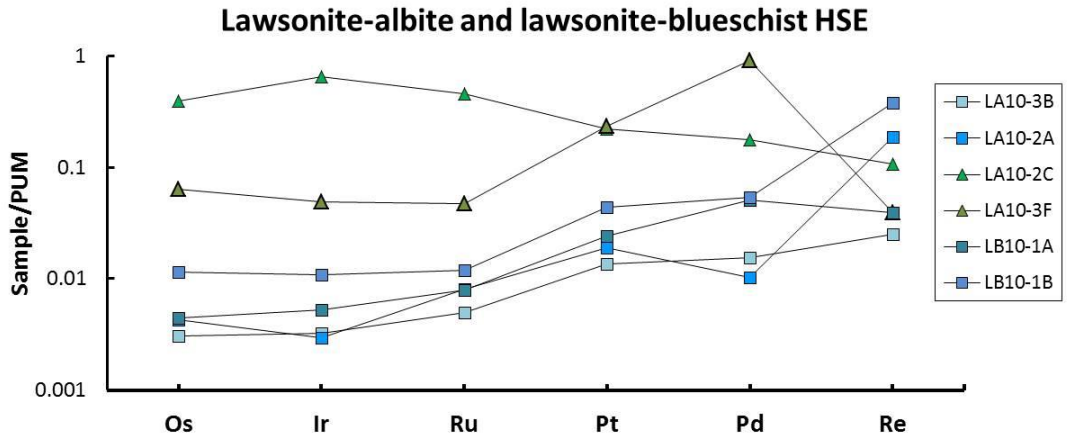

Figure 26: HSE concentrations for lawsonite-albite and lawsonite-blueschist samples normalized to PUM (Becker et al., 2006). Block data are plotted using blue squares. Rind data are plotted using green triangles.

8.2 Attic-Cycladic Complex

8.2.1 Lia Beach traverse

Highly siderophile element data for the Attic-Cycladic complex traverse can be found in Table 13. Osmium concentrations are considerably higher (5.13 ppb) in the serpentinite than the metasomatized zones of the traverse (Fig. 27a). Chlorite-schist blackwall Os concentrations (0.011 to 0.031 ppb) are lower than both the adjacent serpentinite and metasomatic reaction zone. Variable Os concentrations in zones in the meta-tuffite and metasomatic reaction zones range from 1.16 to 0.165 ppb, 1.73 to 1.02 ppb, and 1.71 to 0.232 ppb, respectively. As with Os concentrations, Re, Ir, Pt, Pd, and Ru concentrations are generally lower in the chlorite-schist blackwall, relative to the other zones (Fig. 29). The serpentinite also has elevated Ru and Ir concentrations, relative to the other zones.

Initial $^{187}Os/^{188}Os$ ratios for the serpentinite range from 0.1274 to 0.1228 (Fig. 27b). Zone IV ratios span the largest range of any zone, from 0.7956 to 0.1658. Zones III, II, and I initial $^{187}Os/^{188}Os$ ratios range from 0.2076 to 0.2397, 0.1519 to 0.1661, and from 0.1736 to 0.3231, respectively.

8.2.2 Stavros traverse

Osmium concentration is highest in the serpentinite (2.14 ppb). The adjacent chlorite-schist blackwall zone (Zone D) has an Os concentration of 0.016 ppb (Fig. 28a). The eclogite block and metasomatic reaction zones (zones A, B, and C) all have high Re/Os ratios; therefore, common Os is a better estimate of the Os concentration of these samples. Common Os was calculated assuming a mantle Os isotopic composition of 0.1270. All HSE concentrations for the serpentinite fall around PUM values (Fig.30). Chlorite-schist blackwall concentrations for Ir, Ru, and Pd overlap with the core, while the concentration of Pt drops relative to other zones.

The serpentinite initial $^{187}Os/^{188}Os$ ratio is 0.1242. The chlorite-schist blackwall initial $^{187}Os/^{188}Os$ ratio is 0.2865 (Fig. 28b). The eclogite block and metasomatic reaction zones all have extremely radiogenic Os isotopic compositions, ranging from 10.47 to 14.95. The errors on the core ratios are considerable (55% 2σ) due to the low concentrations of Os (<0.005 ppb).

Table 13: HSE concentrations, $^{187}Os/^{188}Os$, $^{187}Re/^{188}Os$, and $^{187}Os/^{188}Os_{(45Ma)}$ for Syros samples.

Sample	Zone	Sample wt (g)	Re (ppb)	Os (ppb)	Common Os (ppb)	$^{187}Os/^{188}Os$	2σ	$^{187}Re/^{188}Os$	$^{187}Os/^{188}Os_{(45\ Ma)}$	2σ	Pd (ppb)	Pt (ppb)	Ru (ppb)	Ir (ppb)
Lia Beach traverse														
PSIII A7	I	1.49	0.047	0.232		0.3239	0.0032	0.9966	0.3231	0.0034	4.71	2.72	0.961	0.256
duplicate		1.50	0.044	0.301		0.1920	0.0007	0.7070	0.1914	0.0007	n.d.	n.d	n.d.	n.d.
PSIII A6	I	0.50	0.432	1.48		0.1747	0.0005	1.420	0.1736	0.0006	0.599	0.274	0.060	0.023
PSIII A4.2	II	1.45	0.123	1.71		0.1541	0.0001	0.3488	0.1539	0.0001	8.32	4.37	2.12	0.343
duplicate		1.56	0.111	1.73		0.1522	0.0001	0.3106	0.1519	0.0001	n.d.	n.d.	n.d.	n.d.
PSIII A3	II	1.49	0.093	1.02		0.1665	0.0001	0.4391	0.1661	0.0001	0.168	0.270	0.026	0.005
PSIII A2.1	III	1.46	0.069	0.171		0.2091	0.0009	1.963	0.2076	0.0009	8.87	12.5	1.65	0.349
duplicate		1.49	0.078	0.165		0.2155	0.0019	2.309	0.2137	0.0019	n.d.	n.d.	n.d.	n.d.
PSI 10.1	III	1.48	0.159	1.16		0.2402	0.0106	0.6703	0.2397	0.0111	0.163	n.d.	0.159	0.006
duplicate		1.48	0.153	0.287		0.2334	0.0209	2.632	0.2315	0.0209	n.d.	n.d.	n.d.	n.d.
PSI11.1	IV	1.51	0.005	0.056		0.7990	0.0068	0.4455	0.7956	0.0068	0.145	0.433	0.051	0.015
PSII 12.0	IV	1.49	0.004	0.026		0.1841	0.0095	0.8186	0.1835	0.0096	0.075	n.d.	0.250	0.007
duplicate		1.42	0.006	0.031		0.1851	0.0061	0.9549	0.1844	0.0061	n.d.	n.d.	n.d.	n.d.
PSII13.2	IV	1.43	0.005	0.011		0.2210	0.0067	2.204	0.2193	0.0069	0.028	0.218	0.048	0.012
PSII14.0	IV	1.52	0.001	0.031		0.1660	0.0029	0.2099	0.1658	0.0029	0.100	0.330	0.040	0.008
PSII15.2	V	1.44	0.002	1.19		0.1275	0.0001	0.0077	0.1274	0.0001	0.612	0.94	3.08	1.16
duplicate		1.43	0.022	1.04		0.1229	0.0001	0.1014	0.1228	0.0001	n.d.	n.d.	n.d.	n.d.
SY552	V	1.55	0.023	5.13		0.1250	0.0001	0.0213	0.1250	0.0001	0.062	16.5	15.21	7.17
Stavros traverse														
SY530	E	1.37	0.038	2.14	2.14	0.1243	0.0001	0.0847	0.1242	0.0001	1.32	8.45	5.64	2.79
SY522-0	D	2.09	0.021	0.016	0.016	0.2912	0.032	6.313	0.2865	0.033	0.007	0.002	0.021	0.002
SY522-10	C	2.31	0.71	n.d.	n.d.	n.d.	n.d.	n.d.	n.d.	n.d.	0.010	0.022	0.002	0.002
SY522-20	C	1.00	1.42	0.003	0.001	19.92	2.24	6623	14.95	8.285	0.073	0.159	0.005	n.d.
SY522-30	C	2.15	1.07	n.d.	n.d.	n.d.	n.d.	n.d.	n.d.	n.d.	0.053	0.024	0.030	0.0001
SY522-40	B	2.11	1.97	0.004	0.002	n.d.	n.d.	n.d.	n.d.	n.d.	0.006	0.004	0.002	b.d.
SY522-80	B	1.06	3.51	0.003	0.001	29.86	2.22	17690	16.59	14.86	0.024	0.078	0.004	0.0002
duplicate		2.24	1.92	0.004	0.002	n.d.	n.d.	n.d.	n.d.	n.d.	0.006	0.054	0.001	0.0003
SY522-160	A	1.11	1.50	0.002	0.001	16.72	0.46	8329	10.47	2.149	0.001	0.129	0.004	n.d.

n.d. = no data; b.d. = below detection limit.

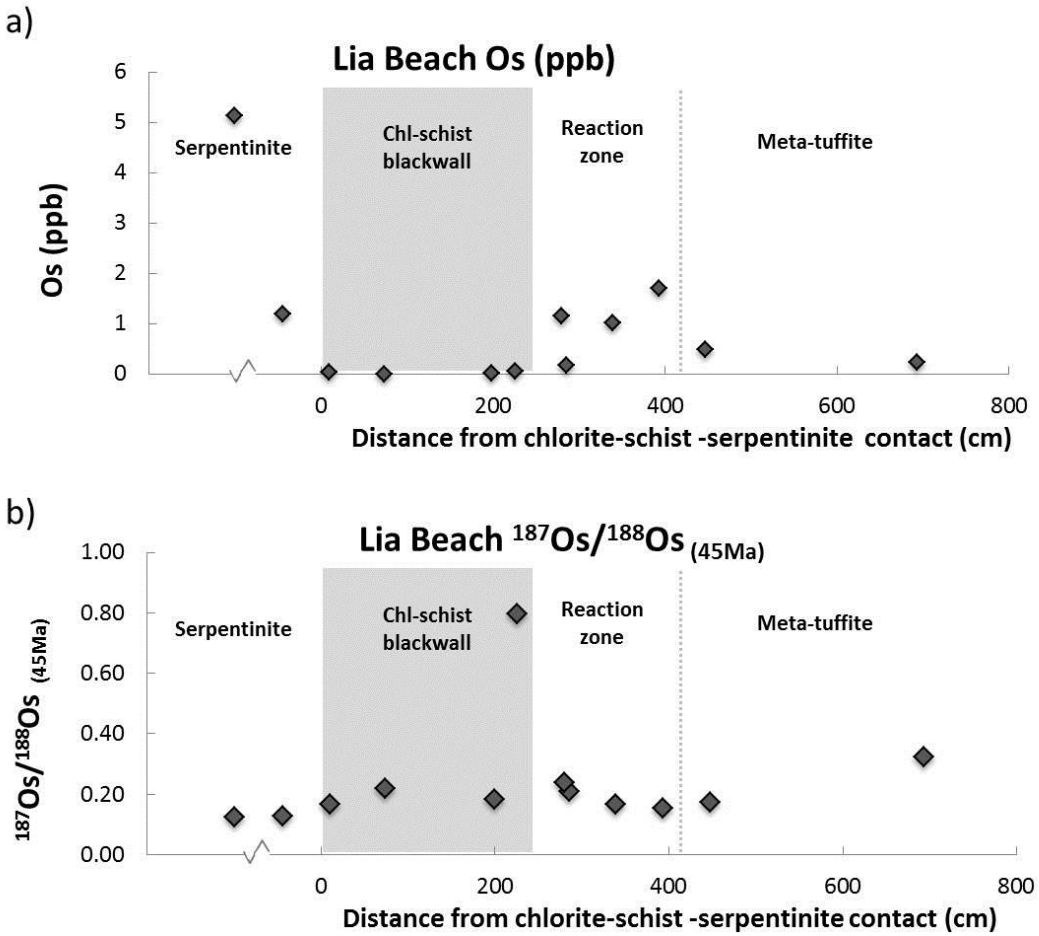

Figure 27: Lia Beach Os concentrations and isotopic data. a) Os (ppb) vs. distance from the chlorite schist-serpentinite contact for the Lia Beach traverse. Os concentrations are lowest in the chlorite-schist blackwall. b) Initial $^{187}Os/^{188}Os$ ratios vs. distance from the chlorite schist-serpentinite contact for the Lia Beach traverse. Distance to serpentinite samples is not plotted to scale.

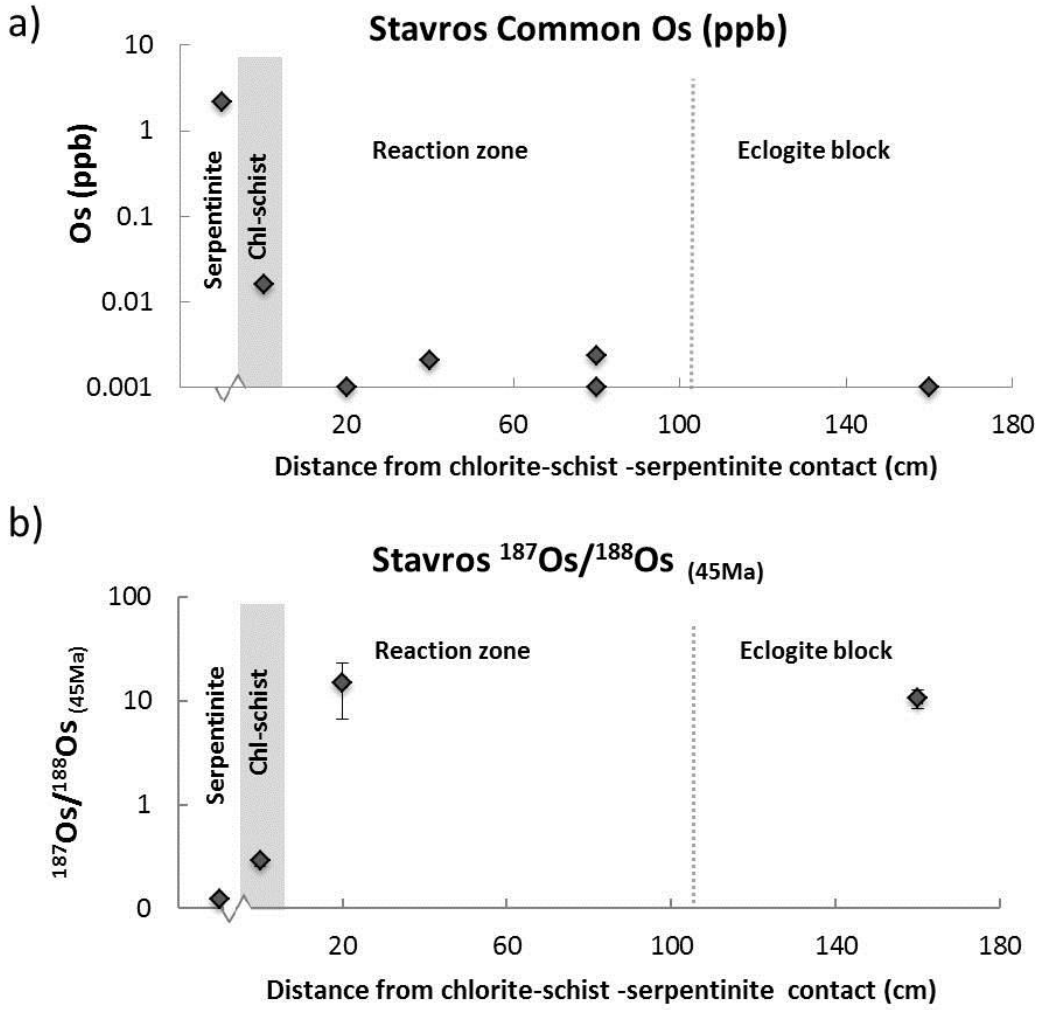

Figure 28: Stavros Os concentrations and isotopic data. a) Common Os (plotted on a logarithmic scale) vs. distance from the chlorite schist-serpentinite contact for the Stavros traverse. Common Os concentrations are more useful when comparing Os concentrations in highly radiogenic samples, as they exclude radiogenic Os from Os concentration comparisons. b) Initial $^{187}Os/^{188}Os$ ratios (plotted on a logarithmic scale) vs. distance from the chlorite schist-serpentinite contact for the Stavros traverse. The core has extremely radiogenic $^{187}Os/^{188}Os$ ratios. Distance to serpentinite samples is not plotted to scale.

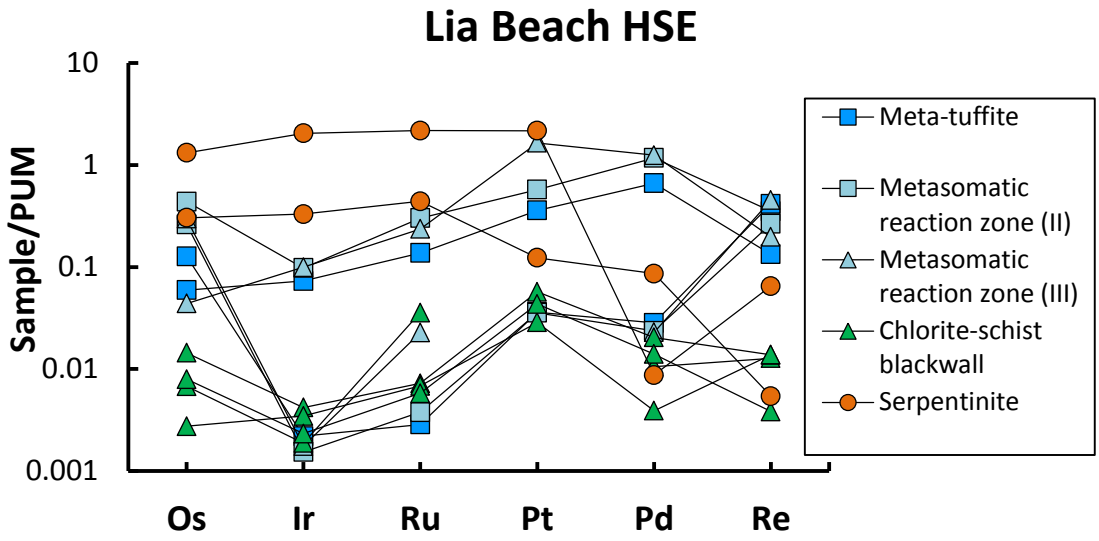

Figure 29: Lia Beach HSE concentrations normalized to PUM.

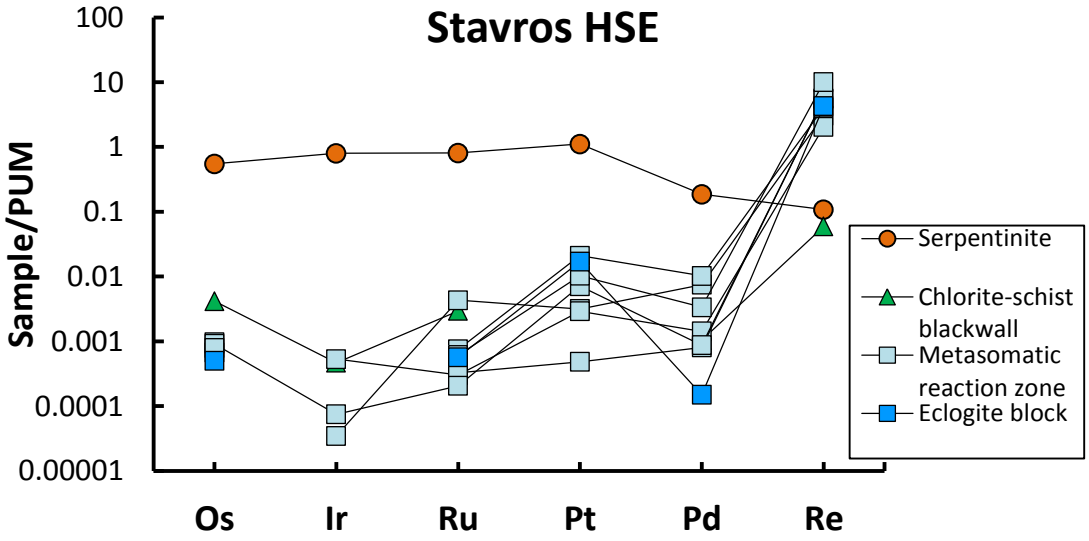

Figure 30: Stavros HSE concentrations normalized to PUM.

Chapter 9: Discussion

9.1 Evidence for mechanical mixing

Certain HSE concentration general patterns emerge from the data. Mafic blocks in all the mélange zones studied have HSE concentrations consistent with MORB. Matrix samples from all locations have HSE concentrations close to peridotite. Most reaction zones have intermediate HSE concentrations.

As previously discussed, HSE, particularly Os, Ir, and Ru, are thought to be relatively fluid-immobile under *P-T* conditions characteristic of subduction mélange zone formation. Therefore, elevated concentrations of elements enriched in peridotite relative to basalt (i.e., Os, Ir, Ru, Ni, and Cr) in reaction rinds suggests mechanical transfer of these elements from peridotite to reaction rind. Mixing of basalt core and peridotitic matrix will create a reaction rind with intermediate HSE concentrations, as shown schematically in Fig. 31.

Moreover, Os, Ir, Ru, Ni, and Cr concentrations will be variable in the reaction zone commensurate with the amount of peridotitic component added. Mixing will also produce the same concentration patterns of immobile elements across the traverse with correlated enrichments in Os, Ir, Ru, Cr, and Ni. Initial $^{187}Os/^{188}Os$ ratios in the reaction zone should also fall between core and matrix and would be variable, with the highest Os concentrations corresponding to the lowest $^{187}Os/^{188}Os$ ratios.

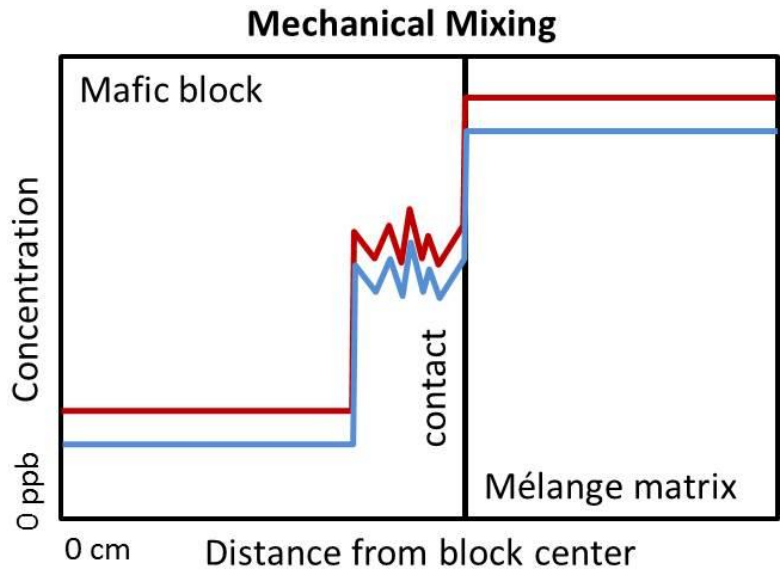

Figure 31: Schematic diagram of traverse concentration profile caused by mechanical mixing (e.g., high Os and Ru concentrations in the mélange matrix mixed with low mafic block Os and Ru concentrations would produce correlated intermediate rind concentrations of Os and Ru.

In addition to intermediate HSE concentrations in the reaction zones, HSE patterns across the Catalina Schist traverses analyzed in this study display other evidence for mechanical mixing: 1) Initial $^{187}Os/^{188}Os$ ratios in the reaction zones are in between measured mafic block and peridotite ratios. 2) HSE concentrations and Os isotopic data are consistent with calculations for mixing between core and peridotite. 3) The irregular patterns of Os, Ir, Ru, Cr, and Ni concentrations across the traverses suggest diffusion did not facilitate the movement of these elements.

The reaction zones in both A10-3 and A12-A4 have intermediate Os concentrations and initial $^{187}Os/^{188}Os$ ratios relative to core and matrix (Fig. 21; 22). The lowest initial $^{187}Os/^{188}Os$ ratio in the rinds corresponds to the highest Os concentrations (i.e., A10-3 [Os] = 1.66 ppb corresponding to $^{187}Os/^{188}Os$ = 0.1336, and A12-A4 [Os] = 2.96 ppb corresponding to $^{187}Os/^{188}Os$ = 0.1314). Lawsonite-

albite and lawsonite-blueschist rinds also have high Os concentrations and low initial $^{187}Os/^{188}Os$ ratios relative to block cores (Fig. 25). These correlations suggest mixing between a low $^{187}Os/^{188}Os$ + Os-, Ir-, Ru-, Ni-, and Cr- rich peridotite and a high $^{187}Os/^{188}Os$ + Os-, Ir-, Ru-, Ni-, and Cr-poor mafic crust.

In order to test the relation between Os concentration and $^{187}Os/^{188}Os$ ratios, mixing curves were calculated for Catalina Schist traverses using peridotite (HSE concentrations from Becker et al., 2006; Cr and Ni concentrations from McDonough and Sun, 1995) as one end member and traverse-specific block core samples as the other end member (Fig. 32). Initial $^{187}Os/^{188}Os$ ratios used for the core end members are 0.3676 for A10-3 samples, and 0.8859 for A12-A4 samples. Rind and mélange matrix samples plot along the mixing line between peridotite and core samples, thus suggesting a mechanically mixed component. Lawsonite-albite and lawsonite-blueschist samples were not plotted due to the limited number of core and rind analysis.

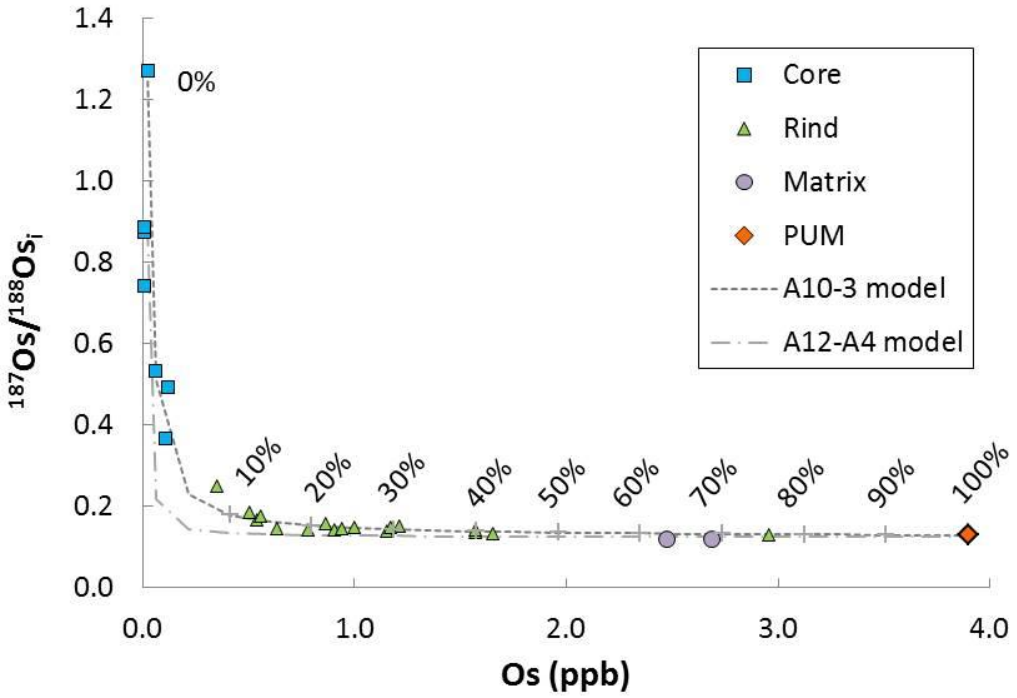

Figure 32: Mixing models of initial $^{187}Os/^{188}Os$ vs. Os (ppb) for the A10-3 and A12-A4 Catalina Schist traverses. The Catalina Schist-traverse rind and matrix samples fall along the model mixing line (dashed line, with % peridotite needed labeled at 10% increments) in between peridotite and core samples. PUM Os concentration and isotopic ratio from Becker et al., 2006).

Additionally, if mechanical mixing produced these reaction rinds, concentrations of immobile elements should correspond to the same percentage of peridotite needed to mix with the core to form that section of the reaction rind. For every rind and mélange matrix sample, mixing percentages for Os, Ir, Ru, and Cr were calculated based on idealized peridotite compositions (Os, Ir, and Ru concentrations from Becker et al., 2006; Cr concentration from McDonough and Sun, 1995) and the highest block concentrations for each traverse (Table 14). For both amphibolite-grade Catalina Schist traverses, the highest percentages of peridotite needed to produce the Os, Ru, and Cr concentrations all correspond to the same samples (A10-3B-R3, and A12-A4-R3). Moreover, when plotting, percent peridotite predicted by Ru and Cr vs. percent peridotite predicted by Os, amphibolite-grade rind

samples plot along the idealized mixing line (Fig. 33). Lawsonite-albite and lawsonite-blueschist samples also plot along the idealized peridotite predicted mixing line (Fig. 33).

The Stavros traverse also has intermediate concentrations of HSE in the chlorite-schist blackwall relative to the eclogite block and serpentinite matrix. Overall the eclogite is considerably depleted in HSE and accompanied by very radiogenic initial Os, similar to block cores on the Catalina Schist. The chlorite-schist and serpentinite samples also plot along the idealized percent peridotite predicted mixing line (Fig. 33), though more data would better define a mixing trend.

Table 14: Calculated percentage of peridotite needed to produce rind Os isotopic ratios and Os, Ir, Ru and Cr concentrations.

Sample	$^{187}Os/^{188}Os_i$	[Os]	[Ir]	[Ru]	[Cr]
A10-3C-R1	32%	21%	21%	28%	n.d.
A10-3C-R2	36%	28%	28%	18.5%	n.d.
A10-3B-R3	66%	41%	33%	25%	40%
A10-3B-R5	22%	24%	21%	18%	23%
A10-3B-R7	17%	20%	11%	12%	19%
A10-3A-R9	12%	12%	11%	8.7%	16%
A10-3A-R11	28%	14%	10.5%	9.3%	17%
A10-3A-R13	8%	11%	8.8%	6.7%	14%
A10-3A-R15	10%	12%	14%	8.1%	15%
A12-A4-R1	0.7%	9%	6%	6%	6%
A13-A4-R2	5%	31%	26%	28%	15%
A12-A4-R3	66%	76%	50%	65%	23%
duplicate	12%	40%	32%	38%	23%
A12-A4-R4	5.5%	30%	28%	27%	16%
A12-A4-R5	6%	24%	26%	23%	15%
A12-A4-R6	7.5%	40%	33%	34%	14%
A12-A4-R7	7%	20%	27%	21%	12%
6-4-6	100%	63%	61%	72%	100%
6-4-11	100%	69%	60%	73%	100%
LA10-2C	100%	39%	65%	95%	99%
LA10-3F	55%	6%	5%	4%	48%
SY530	100%	55%	n.d.	31%	74%
SY5522-0	1.4%	0%	n.d.	2%	0%

Assumed peridotite concentration [Os] = 3.9 ppb, [Ir] 3.5 ppb, [Ru] = 7.0 ppb (Becker et al., 2006); [Cr] = 2625 ppm (McDonough and Sun, 1995).

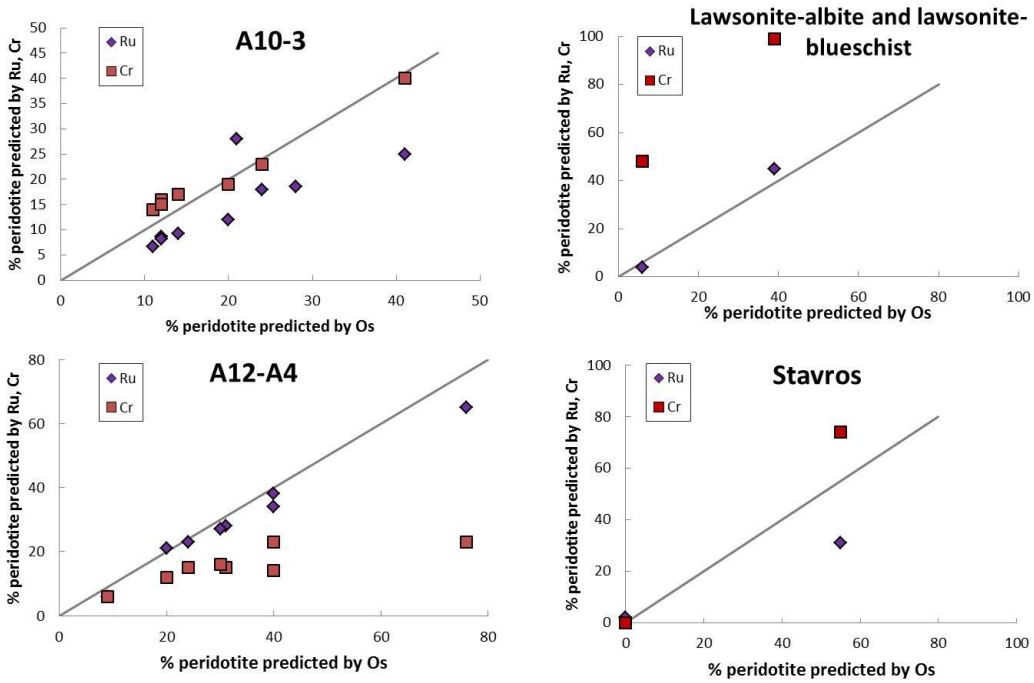

Figure 33: Percent peridotite predicted for Ru and Cr vs. percent peridotite predicted for Os for the Catalina Schist traverse and the Stavros traverse. 1-to-1 ideal prediction lines are plotted in gray.

It is possible that variations in elemental concentrations could simply be a function of volume changes in the reaction zone due to the addition or removal of other elements during reaction zone formation. To eliminate the possible effects of volume change during alteration on concentration data, concentrations are normalized to Zr (Fig. 32), an element that is thought to be essentially immobile during metamorphism (e.g., Bebout and Barton, 2002; Ague 1994; Baumgartner and Olsen, 1995). Normalized trends of Cr, Os, and Ni to Zr retain elevated ratios in the reaction rind relative to the block core, as well as irregular peaks in the rind that co-vary (Fig. 34). Therefore, these trends indicate that mass changes in the reaction rind cannot

solely account for the elevated concentrations of Os, Cr and Ni. A mixing component is still needed to account for concentration changes.

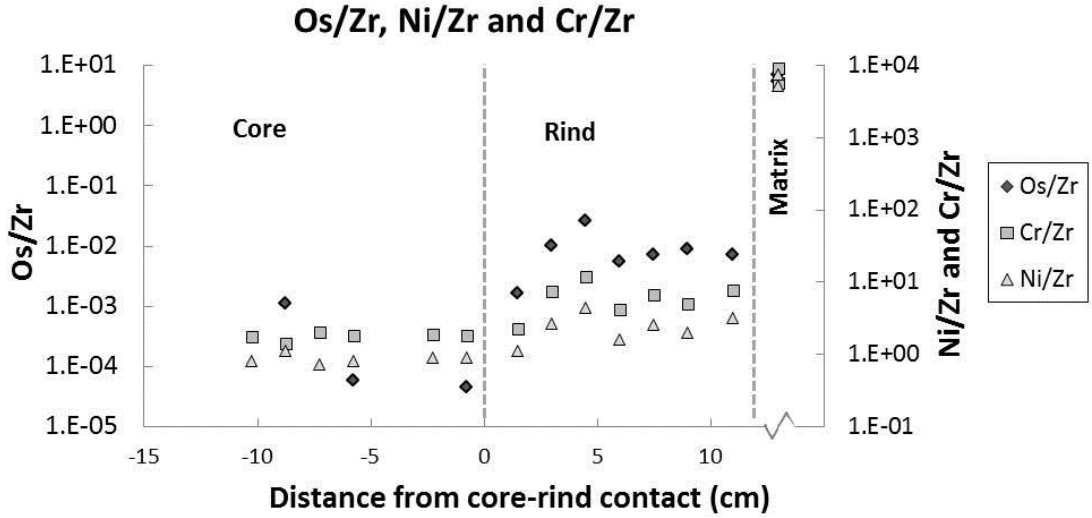

Figure 34: Normalized plots of Cr, Os and Ni to Zr (plotted on a logarithmic scale) vs. distance from the core-rind contact from the A12-A4 traverse. Normalized plots exhibit similar trends to non-normalized plots.

9.2 Evidence for fluid infiltration: A10-3 traverse

In toto, HSE, Cr, and Ni data suggest mechanical mixing is a viable mechanism for reaction zone formation in the Catalina Schist and the Stavros traverse from the Attic-Cycladic complex. However, the three mechanisms possibly attributed to reaction rind formation are not mutually exclusive. Evidence for fluid infiltration is seen texturally as phengite and chlorite after amphibole and garnet pseudomorphs in the A10-3 rind. In addition, the decussate texture of the A10-3 rind suggests static fluid infiltration. The foliation present in all Catalina Schist traverses indicates a

dynamic environment prior to static recrystallization. The fluid mobile elements Ba and K have higher concentrations in rind compared to both block core and mélange matrix. These elevated concentrations of Ba and K can be attributed to the crystallization of phengite, which is the main mineral host of Ba and K in these rinds, as it replaces both garnet and amphibole and is therefore likely due to a late addition of these elements by a fluid.

The Stavros traverse metasomatic reaction zone and block core are not foliated, suggesting a more static environment of formation. The chlorite schist is weakly foliated, suggesting a dynamic environment at some stage of formation. The composition of K_2O decreases steadily from eclogite block to serpentinite. Barium concentrations fluctuate along the traverse, with the highest concentration in the metasomatic reaction zone (Zone C). Therefore, no addition of Ba and K via a sedimentary source is required to explain the fluid-mobile element concentration of the chlorite-schist reaction zone.

9.3 Evidence for the relative timing of mechanical mixing and fluid infiltration

The presence of garnet in both rind and core of the A10-3 traverse may help to constrain the timing of mechanical mixing relative to garnet growth, fluid infiltration and deposition of fluid-mobile elements. Disparate garnet chemical compositions in the rind and core suggests the garnets formed after mechanical mixing produced a chemical change in the rocks, while textural replacement of garnet by hydrous phases (phengite and chlorite) suggests garnet growth occurred before fluid infiltration.

The Mn zoning seen in the core garnets (i.e., higher concentrations of Mn at the centers of garnets) is commonly interpreted to indicate prograde garnet growth

(e.g., Sakai et al., 1985; Grover et al., 1992). The preservation of zoning in core garnets suggests that their compositions reflect the growth of garnet and not a later phenomenon. Differences in garnet chemistry between core and rind garnets provide clues to the timing of garnet formation. Rind garnets contain more MgO (~5 wt%) and less CaO (~7 wt%) than core garnets (~4 wt% MgO, and ~9 wt% CaO), suggesting that the bulk-rock chemistry of the rind was altered relative to the core prior to rind garnet growth. Mineralogically, replacement of garnet with hydrous phases such as phengite and chlorite indicates garnet growth in the rind ended prior to the end of fluid infiltration and the addition of fluid-mobile elements.

9.4 Anomalous traverse profiles

The Lia Beach traverse profile is inconsistent with the profiles seen in the Catalina Schist and the trends one would expect to see if mechanical mixing were a primary mechanism of mélange zone formation. Mixing models of initial $^{187}Os/^{188}Os$ and Os concentration (Fig. 35) show that Os and $^{187}Os/^{188}Os$ do not correlate to a simple mixing trend, as chlorite-schist blackwall Os concentrations fall below the mixing line. Additionally, percent peridotite predicted by Ru and Cr does not correlate well to percent peridotite predicted by Os (Fig. 36). Both mixing plots indicate that mechanical mixing may not be operating to form the chlorite-schist blackwall.

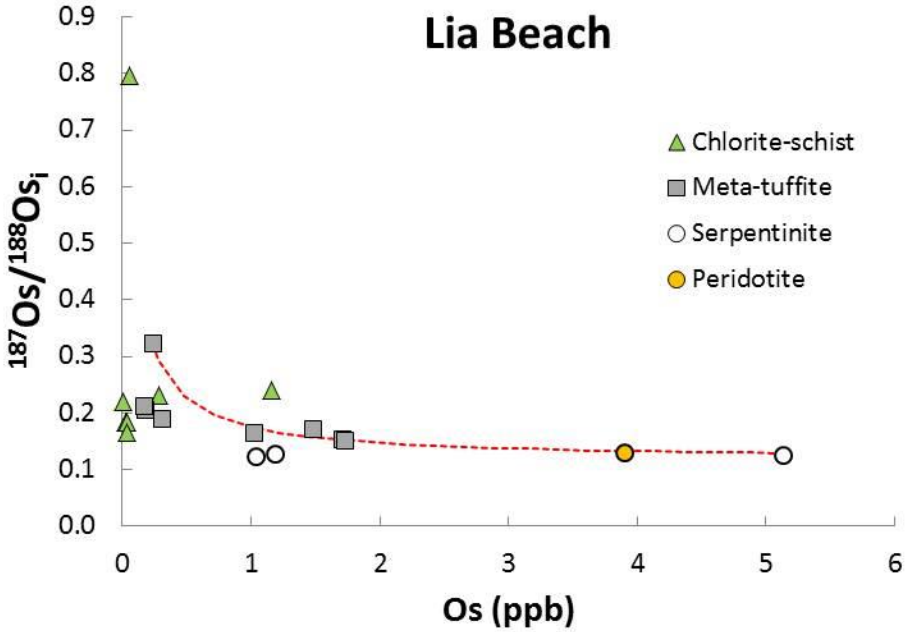

Figure 35: Mixing model of initial $^{187}Os/^{188}Os$ and Os (ppb) for the Lia Beach traverse. An idealized mixing line is plotted in red. Chlorite-schist blackwall samples plot well off the idealized mixing line.

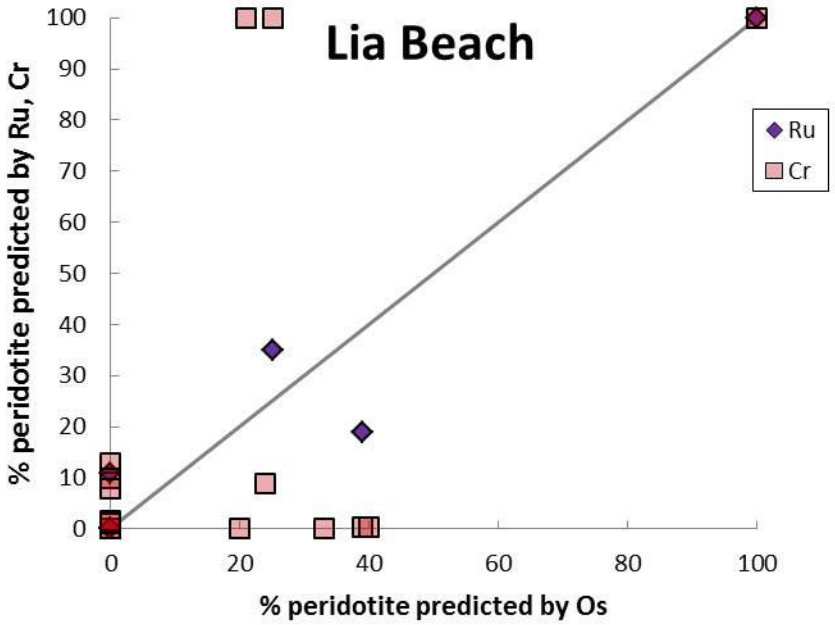

Figure 36: Percent peridotite predicted by Ru and Cr vs. percent peridotite predicted by Os for the Lia Beach traverse. Idealized 1-to-1 percent peridotite predicted line is shown in gray. There does not appear to be a correlation between the percent peridotite predicted by these different elements.

To account for possible volume change effects, concentrations of Re, Os, Cr, and Ni were normalized to Zr (Fig. 37). Ratios of Os/Zr and Re/Zr are still lowest in the blackwall chlorite-schist, whereas Cr/Zr and Ni/Zr exhibit very different trends from Os/Zr and Re/Zr. Miller et al. (2009) attribute the Cr and Ni profile to diffusion. Regardless of mass transfer mechanism, the behavior of HSE across the traverse is different from Cr and Ni.

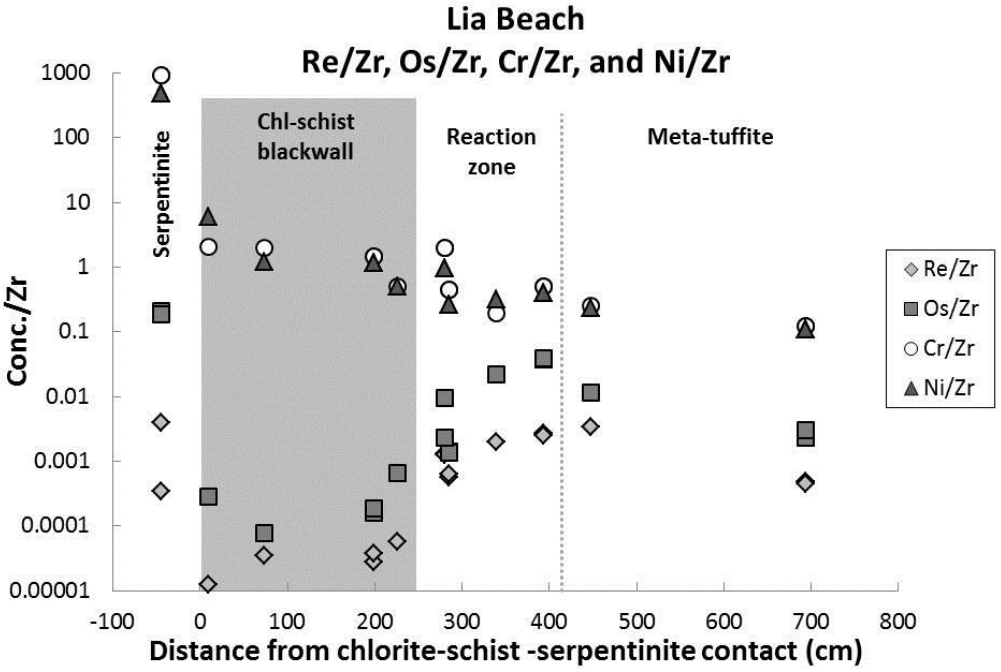

Figure 37: Normalized concentrations of Cr, Ni, Re, and Os to Zr (plotted on a logarithmic scale) for the Lia Beach traverse. Both Re/Zr and Os/Zr are depleted in the chlorite-schist blackwall relative to core and serpentinite. Cr/Zr and Ni/Zr have intermediate ratios in the chlorite-schist blackwall.

The presence of decussate chlorite-after-garnet pseudomorphs (Miller et al., 2009) in the Lia Beach traverse suggests a static environment. However, Miller et al. (2009) also describe lineation in the glaucophane-rich meta-tuffite, chlorite-schist, and serpentine, with increasing intensity of foliation as proximity to the chlorite-schist reaction zone increases. This foliation suggests a dynamic environment and

therefore the possibility of mechanical mixing that may later have been overprinted. This idea is supported by the relative high concentrations of HSE in the metatuffite adjacent to the chlorite schist blackwall. These concentrations are higher than expected for metamorphosed volcanic rocks and in some cases overlap concentrations of the serpentinite matrix. Experimental research (Xiong and Wood, 2000) has suggested HSE may be mobile in high temperature, chlorine-rich fluids. Mechanical mixing signatures may have been partially erased by mobility of HSE in a Cl-rich subduction zone derived fluid.

Chapter 10: Conclusions

Highly siderophile element concentrations in the mafic blocks in the Catalina Schist traverses and the Stavros traverse are consistent with crustal compositions. Highly siderophile element concentrations in serpentinite/matrix are close to peridotite concentrations. The following results all support a mechanical mixing hypothesis for the formation of reaction zones: 1) Os, Ir, Ru, Ni, and Cr have intermediate concentrations in the reaction zones, 2) Reaction zone samples plot along idealized mixing trends between peridotite and basalt, and 3) HSE, Cr, and Ni concentrations co-vary along the traverses.

The addition of the fluid-mobile elements Ba and K also suggests a late fluid infiltration from a source with high Ba and K concentrations. Due to the disparate chemical compositions of core and rind garnets, rind garnets likely grew after mechanical mixing and were subsequently replaced by chlorite and phengite under retrograde metamorphic conditions.

The Lia Beach traverse provides a contrast to the Catalina Schist traverses. Depletion of HSE in the chlorite-schist blackwall zone suggests mechanical mixing may not be the primary mechanism for reaction zone formation in this locality. Chromium and Ni are decoupled from the HSE concentrations, indicating Cr and Ni do not have the same primary mechanism of mass transport. Miller et al. (2009) cites diffusion through an intergranular fluid to explain the Ni and Cr profiles across the traverse. Therefore, Miller et al. (2009) suggest diffusion was an active process creating the Lia Beach chlorite-schist blackwall zone. However, diffusion of HSE would not create the depletion of HSE in the chlorite-schist blackwall. The depletion

of HSE in the chlorite-schist blackwall may instead suggest the transport of the HSE by subduction-derived fluid. This is consistent with the interpretation by Miller et al. (2009) that K was leached by a fluid in the blackwall.

In summary, the results of this study suggest mechanical mixing was an active process in the Catalina Schist formation, as proposed by Bebout and Barton (2002) and Penniston-Dorland et al. (2012b). Therefore, we conclude mechanical mixing may play an identifiable role in the geochemical cycling of HSE in subduction zones. The Lia Beach traverse suggests that HSE may be mobilized in subduction related mélange zones and thus may be more mobile in subduction zone fluids than previously thought. Further work on additional traverses across serpentinite-reaction zone-core contacts in mélange zones will be instrumental in determining the extent of possible HSE mobility via fluid vs. mechanical mixing in subduction mélange zones.

Appendix A: Major element compositions of garnets

Table A-1: Rind Garnet 1 chemical composition (wt %) traverse.

No.	SiO_2	TiO_2	Al_2O_3	FeO	MgO	CaO	MnO	Total
9	38.20	0.06	21.39	25.29	7.01	5.46	1.73	99.14
10	38.04	0.08	21.29	25.30	6.86	5.80	1.73	99.10
11	37.94	0.09	21.31	25.34	6.74	5.85	1.67	98.94
12	38.01	0.10	21.28	25.07	6.88	5.88	1.69	98.90
13	37.93	0.10	21.13	25.25	6.84	5.89	1.69	98.81
14	38.17	0.07	21.22	25.01	6.80	5.89	1.66	98.81
15	38.05	0.10	21.25	25.36	6.81	5.84	1.72	99.13
16	38.33	0.05	21.23	25.11	7.03	5.63	1.69	99.06
17	37.89	0.03	21.25	25.26	7.03	5.41	1.73	98.61
18	37.75	0.05	21.23	25.12	7.15	5.29	1.72	98.32

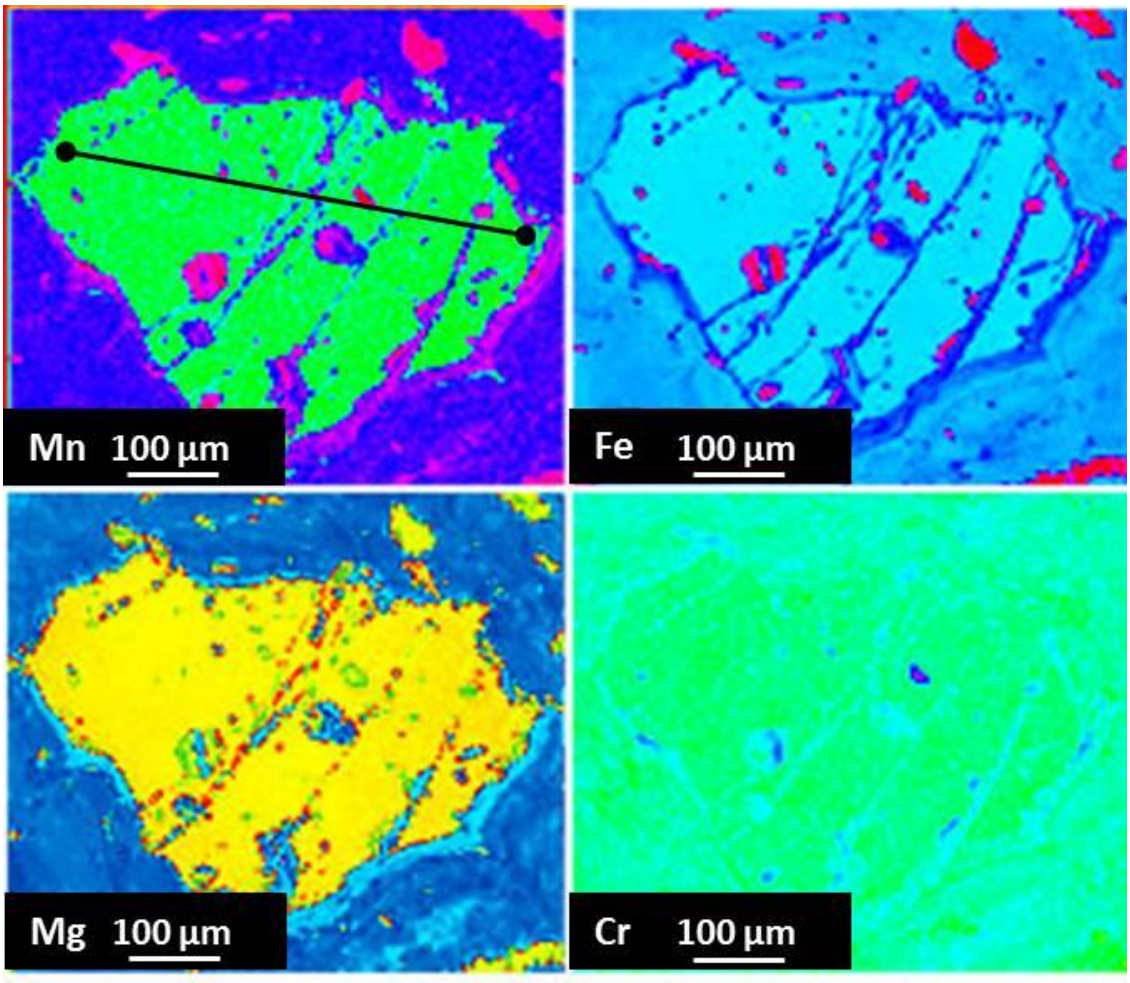

Figure A-1: X-ray map of rind garnet #1 (A10-3 traverse). Black line on Mn map shows EPMA data points.

Table A-2: Rind Garnet 2 chemical composition (wt %) traverse and rim data points.

No.	SiO_2	TiO_2	Al_2O_3	FeO	MgO	CaO	MnO	Total
19	37.46	0.00	21.16	27.51	6.27	2.80	3.36	98.57
20	37.46	0.05	21.24	27.26	6.49	3.27	3.12	98.89
21	37.53	0.07	21.07	27.24	6.43	3.47	3.06	98.88
23	37.69	0.01	21.24	27.39	6.55	3.06	3.19	99.14
24	37.62	0.04	21.14	27.16	6.68	3.34	3.02	99.01
25	37.70	0.12	21.13	27.16	6.73	3.31	2.88	99.03
26	37.76	0.01	21.56	26.73	6.35	3.67	3.16	99.23
27	37.55	0.00	21.28	27.09	5.77	3.33	3.55	98.57
28	37.51	0.01	21.43	27.36	5.64	3.33	3.63	98.92

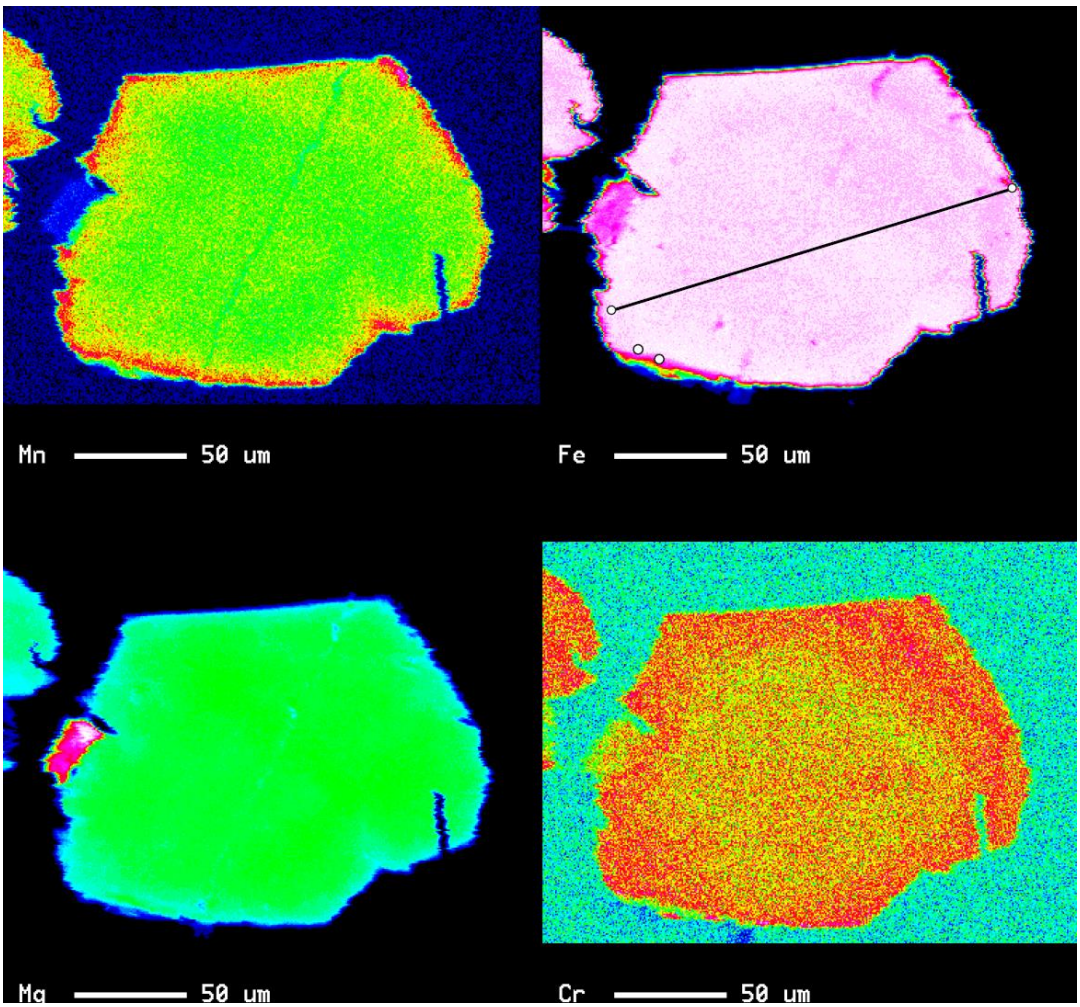

Figure A-2: X-ray map of rind garnet #2 (A10-3 traverse). Black line and points on Fe map show EPMA data points.

Table A-3: Rind Garnet 3 chemical composition (wt %) traverse and rim data points.

No.	SiO_2	TiO_2	Al_2O_3	FeO	MgO	CaO	MnO	Total
29	37.99	0.05	21.62	25.40	7.26	5.48	1.74	99.53
30	38.00	0.07	21.27	25.44	7.25	5.22	1.84	99.10
31	37.78	0.07	21.32	25.33	7.07	5.39	1.87	98.82
32	37.82	0.08	21.18	25.16	6.96	5.44	1.96	98.59
35	37.97	0.04	21.29	25.44	7.20	5.06	2.12	99.12
37	38.14	0.08	21.18	25.58	7.49	4.59	2.12	99.18
38	38.18	0.11	21.13	25.75	7.34	4.52	2.11	99.15
39	37.63	0.09	21.15	26.15	6.52	3.89	2.96	98.37
40	37.56	0.06	21.08	26.03	6.58	4.03	3.08	98.43
41	37.65	0.06	21.26	26.43	6.51	4.04	2.898	98.85

X-ray map for rind garnet 3 in text (Fig.14)

Table A-4: Core Garnet 5 chemical composition (wt %) traverse.

No.	μm	SiO_2	TiO_2	Al_2O_3	FeO	MgO	CaO	MnO	Total
194	0	38.16	0.00	21.79	26.44	7.01	5.10	1.10	99.62
195	71	38.27	0.01	21.80	26.34	7.31	4.98	1.00	99.71
196	142	38.91	0.04	21.69	25.77	6.37	5.78	0.77	99.33
197	213	38.33	0.05	21.72	25.78	6.61	6.75	0.48	99.73
198	284	38.31	0.01	21.80	26.14	6.21	6.99	0.40	99.86
199	355	37.96	0.04	21.70	26.10	5.74	7.60	0.41	99.54
200	426	38.24	0.01	21.62	26.54	5.29	7.65	0.44	99.79
201	497	37.77	0.07	21.58	26.25	5.02	8.28	0.49	99.46
203	639	37.95	0.02	21.64	25.93	4.87	8.52	0.68	99.62
204	710	37.81	0.03	21.67	26.35	5.20	7.80	0.83	99.68
205	781	37.79	0.02	21.62	26.44	5.37	7.44	0.91	99.60
206	852	38.20	0.03	21.57	26.36	5.71	6.95	0.94	99.76
208	994	37.71	0.06	21.37	27.13	5.67	6.13	1.19	99.25
210	1136	37.72	0.01	21.43	27.11	5.68	6.25	1.18	99.40
212	1278	37.94	0.05	21.52	26.95	5.75	6.46	1.24	99.89
213	1349	37.76	0.06	21.38	26.61	5.88	6.52	1.26	99.46

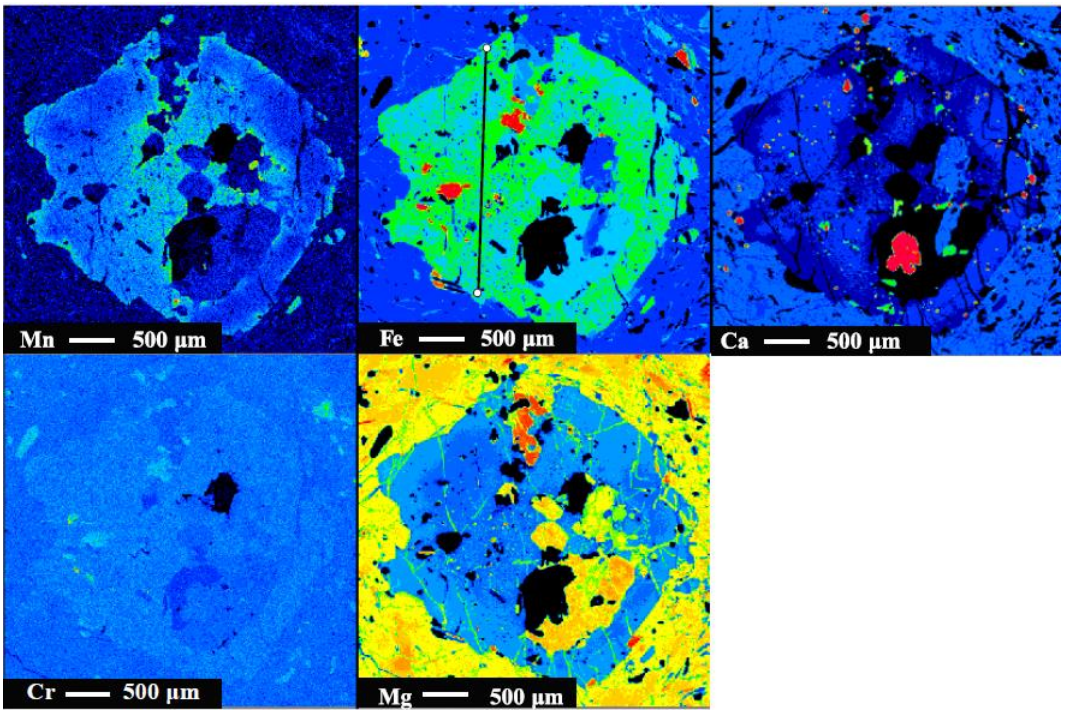

Figure A-3: X-ray map of core garnet #5 (A10-3 traverse). Black line and points on Fe map show EPMA data points.

Table A-5: Core Garnet 8 chemical composition (wt %) traverse and core and rim data points.

No.	µm	SiO_2	TiO_2	Al_2O_3	FeO	MgO	CaO	MnO	Total
223	0	38.01	0.20	21.65	27.58	6.03	5.61	0.90	99.99
224	97	38.16	0.07	21.58	26.91	6.25	6.21	0.72	99.90
225	193	37.85	0.10	21.41	26.24	6.01	7.19	0.59	99.37
226	290	37.90	0.18	21.33	25.51	5.27	8.45	0.58	99.21
227	386	38.03	0.17	21.45	26.03	4.70	8.75	0.70	99.82
228	483	37.94	0.11	21.48	25.56	4.47	9.49	0.72	99.76
231	772	37.51	0.09	21.20	25.35	4.14	9.63	1.02	98.93
232	869	37.79	0.04	21.54	25.67	4.48	9.14	1.08	99.73
233	966	37.84	0.00	21.51	26.88	4.38	8.11	1.20	99.93
238	1448	37.38	0.09	21.12	25.73	4.61	8.00	1.56	98.48
239	1545	37.50	0.00	21.65	26.22	4.69	7.89	1.53	99.47
240	1641	37.31	0.06	21.22	25.82	4.52	8.02	1.56	98.51
241	1738	37.87	0.09	21.36	26.00	4.43	8.31	1.65	99.71
243	1931	37.32	0.16	21.20	25.35	4.56	8.48	1.60	98.66
247	2317	37.75	0.17	21.37	25.19	5.01	8.61	1.19	99.30
248	2414	37.60	0.19	21.50	25.11	5.31	8.52	0.85	99.08
249	2510	37.72	0.11	21.47	25.24	6.02	7.78	0.56	98.90
250	2607	37.96	0.08	21.67	25.73	6.55	6.57	0.45	99.02
251	2703	38.17	0.13	21.55	25.01	6.31	7.63	0.42	99.21

No.	µm	SiO_2	TiO_2	Al_2O_3	FeO	MgO	CaO	MnO	Total
252	2800	37.81	0.01	21.64	26.87	6.20	6.12	0.80	99.45
214	rim	38.15	0.00	21.75	26.64	6.77	5.42	1.02	99.76
215	rim	38.16	0.01	21.82	26.11	6.72	5.97	0.88	99.67
216	rim	38.40	0.02	21.77	26.20	6.52	6.32	0.67	99.91
217	rim	38.05	0.03	21.92	26.35	7.13	5.53	0.86	99.87
218	rim	38.24	0.02	21.75	26.36	6.50	6.20	0.80	99.88
219	core	37.92	0.04	21.57	26.48	5.05	8.12	0.55	99.73
220	core	37.94	0.04	21.64	26.36	4.74	8.53	0.58	99.84
221	core	38.09	0.03	21.80	26.07	4.74	8.58	0.58	99.89
222	core	38.06	0.04	21.58	26.61	4.93	8.27	0.52	100.01

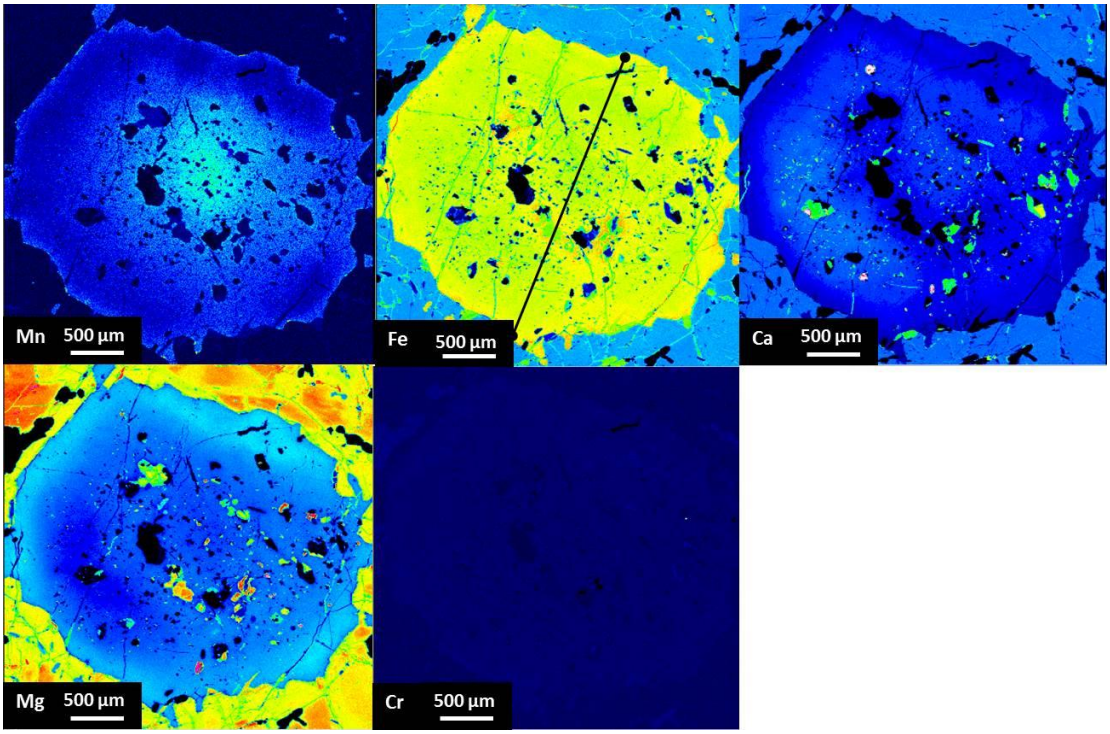

Figure A-4: X-ray map from core garnet #8 (A10-3 traverse). Black line on Fe map shows EPMA data points.

Table A-6: Core Garnet 9 chemical composition (wt %) traverse and core and rim data points.

No.	µm	SiO_2	TiO_2	Al_2O_3	FeO	MgO	CaO	MnO	Total
42	0	38.24	0.07	21.53	26.92	5.79	6.71	0.70	99.97
43	38	38.52	0.07	21.65	25.40	6.65	7.25	0.32	99.87
44	77	38.37	0.12	21.45	24.80	6.20	8.46	0.27	99.69
45	115	38.35	0.10	21.52	24.56	6.03	8.63	0.26	99.46
46	154	38.06	0.17	21.31	24.59	5.38	9.31	0.42	99.24
47	192	37.90	0.17	21.20	24.86	5.28	8.87	0.48	98.76

No.	μm	SiO_2	TiO_2	Al_2O_3	FeO	MgO	CaO	MnO	Total
48	231	37.95	0.17	21.27	25.46	5.63	8.26	0.47	99.21
49	269	37.88	0.21	21.24	24.85	4.74	9.90	0.53	99.34
50	308	37.71	0.07	21.29	25.49	4.07	10.16	0.69	99.47
51	346	37.71	0.13	21.21	25.28	3.44	10.82	0.77	99.37
52	385	37.66	0.13	21.12	25.29	3.30	11.09	0.83	99.42
53	423	37.55	0.13	21.29	25.43	3.14	11.02	0.88	99.44
54	462	37.33	0.06	21.24	26.73	2.78	10.29	0.99	99.43
55	500	37.61	0.12	21.29	25.17	3.06	11.38	0.97	99.60
56	538	37.31	0.20	21.07	24.82	3.21	10.97	1.00	98.57
57	577	37.48	0.16	21.14	25.00	3.39	11.09	1.08	99.34
58	615	37.30	0.15	21.01	25.61	3.64	9.96	1.08	98.77
60	692	37.61	0.12	21.19	25.65	3.83	9.95	1.14	99.50
61	731	37.64	0.09	21.12	25.63	3.83	9.97	1.06	99.34
62	769	37.50	0.05	20.98	26.32	3.81	9.24	1.12	99.02
63	808	37.55	0.09	21.10	26.28	3.79	9.27	1.15	99.23
65	885	37.59	0.16	21.10	24.80	3.48	10.85	1.20	99.18
66	923	37.65	0.14	21.06	24.54	3.23	11.29	1.29	99.21
67	962	37.48	0.15	21.07	25.10	3.31	10.91	1.17	99.18
68	1000	37.49	0.16	21.14	24.84	3.16	11.18	1.14	99.11
69	1038	37.49	0.15	21.27	24.73	3.11	11.58	1.09	99.42
71	1115	39.14	0.20	21.51	24.52	4.07	10.31	0.88	100.64
72	1154	37.87	0.11	21.42	24.73	3.85	10.98	0.84	99.81
73	1192	37.75	0.10	21.41	24.81	4.16	10.49	0.79	99.49
74	1231	37.67	0.23	21.16	24.86	4.72	9.89	0.61	99.14
75	1269	37.61	0.19	21.12	24.62	5.31	9.39	0.45	98.69
76	1308	38.03	0.16	21.53	25.45	5.86	8.21	0.39	99.63
77	1346	38.20	0.14	21.49	24.79	5.78	8.78	0.35	99.54
78	1385	38.14	0.25	21.46	23.92	5.79	9.71	0.33	99.61
79	1423	38.05	0.16	21.53	23.76	6.05	8.97	0.30	98.83
80	1462	38.16	0.04	21.59	25.52	6.42	7.63	0.32	99.68
81	1500	37.99	0.04	21.62	26.58	5.66	7.16	0.71	99.77
82	core	37.79	0.13	21.23	24.96	3.75	10.52	1.19	99.56
83	core	37.97	0.17	21.27	24.59	3.74	10.92	1.15	99.80
84	core	37.65	0.13	21.08	25.28	3.87	10.07	1.14	99.22
85	core	37.55	0.12	21.11	25.55	3.83	9.78	1.18	99.12
86	core	37.50	0.14	21.13	25.46	3.86	10.00	1.11	99.20
87	rim	37.84	0.04	21.50	26.57	5.96	6.66	0.65	99.22
88	rim	37.92	0.03	21.56	26.39	6.08	6.73	0.48	99.18
89	rim	37.89	0.04	21.53	26.69	5.99	6.57	0.64	99.33
90	rim	37.91	0.05	21.32	26.62	5.63	6.68	0.72	98.93
91	rim	37.97	0.02	21.28	26.69	6.05	6.50	0.64	99.15

X-ray map for core garnet 9 in text (Fig. 15)

Bibliography

Ague, J.J., 1994. Mass transfer during Barovian metamorphism of pelites, south-central Connecticut: I. Evidence for changes in composition and volume. *American Journal of Science*, **294**, 989–1057.

Altherr, R., Schliestedt,M., Okrusch, M., Seidel, E., Kreuzer, H., Harre, W., Lenz, H., Wendt, I., Wagner, G.A. (1979): Geochronology of High-Pressure Rocks on Sifnos (Cyclades, Greece). *Contributions to Mineralogy and Petrology*, **70**, 245–255.

Alves, S., Schiano, P., Allegre, C.J., 1999, Rhenium-osmium isotopic investigation of Java subduction zone lavas, *Earth and Planetary Science Letters*, **168**, 65–77.

Alves, S., Schiano, P., Capmas, F., Allegre, C.J., 2002. Osmium isotope binary mixing arrays in arc volcanism. *Earth and Planetary Science Letters*, **198,** 355–369.

Andriessen, P., Boelrijk, N., Hebeba, E., Priem, N., Verdurmen, E., Vershure, R. 1979. Dating the events of metamorphism and granitic magmatism in the alpine orogen of Naxos (Cyclades, Greece). *Contributions to Mineralogy and Petrology*, **69**, 215–225.

Anczkiewicz, R., Platt, J.P., Thirlwall, M.F., Wakabayashi, J., 2004. Franciscan subduction off to a slow start: evidence from high-precision Lu-Hf garnet ages on high gradeblocks. *Earth and Planetary Science Letters*. **225**, 147–161.

Baumgartner, L.P., Olsen, S.N., 1995. A least-squares approach to mass transport calculations using the isocon method. *Economic Geology*. **90**, 1261–1270.

Beane, R.J. and Liou, J.G., 2005. Metasomatism in Serpentinite Mélange Rocks from the High-Pressure Maksyutov Complex, Southern Ural Mountains, Russia. *International Geology Review*, **47**, 24–40.

Bebout, G.E., and Barton, M.D., 1989. Fluid-flow and metasomatism in a subduction zone hydrothermal system – Catalina-Schist Terrane, California, *Geology*, **17**, 976–980.

Bebout, G.E., and Barton, M.D., 2002, Tectonic and metasomatic mixing in a high-T, subduction-zone mélange – insights into the geochemical evolution of the slab-mantle interface, *Chemical Geology*, **187**, 79–106.

Becker, H., Horan, M.F., Walker, R.J., Gao, S., Lorand, J.-P., Rudnick, R.L., 2006, Highly siderophile element composition of the Earth's primitive upper mantle: Constraints from new data on peridotite massifs and xenoliths, *Geochimica et Cosmochimica Acta*, **70**, 4528–4550.

Birck, J.L., Barman, M.R., Capmas, F., 1997 Re–Os isotopic measurements at the femtomole level in natural samples. *Geostandards Newsletter*, **21**, 19–27.

Blake, M.C., Bonneau, M., Geyssant, J., Kienast, J.R., Lepvrier, C., Maluski, H., Papanikolaou, D. 1981. A geological reconnaissance of the Cyclacic blueschist belt, Greece. *Geological Society of America Bulletin*, **92**, 247–254.

Borg, L. E., Brandon, A.D., Clynne, M.A., Walker, R.J., 2000. Re–Os isotopic systematics of primitive lavas from the Lassen region of the Cascade arc, California. *Earth and Planetary Science Letters*, **177**, 301–317.

Brandon, A.D., Creaser, R.A., Shirey, S.B., and Carlson, R.W., 1996, Osmium recycling in subduction zones, *Science*, **272**, 861–864.

Cohen, A.S., Waters, F.J., 1996. Separation of osmium from geological materials by solvent extraction for analysis by thermal ionization mass spectrometry. *Analytica Chimica Acta*, **332**, 269–275.

Dale, C.W., Luguet, A., Macpherson, CG., Pearson, D.G.,Hickey-Vargas, R., 2008. Extreme platinum-group element fractionation and variable Os isotope compositions in Philippine Sea Plate basalts: tracing mantle source heterogeneity. *Chemical Geology.* **248**, 213–238.

Dixon J.E., 1968. The metamorphic rocks of Syros, Greece. Ph.D. thesis, St. John's College, Cambridge.

Dürr S, Altherr R, Keller J, Okrusch M, Seidel E., 1978. The median Aegean crystalline belt: stratigraphy, structure, metamorphism, magmatism. In: Closs H, Roeder DH, Schmidt K (eds.) Alps, Apennines, Hellenides, *Inter-Union Commission on Geodynamics, Scientific Report*, **38**, 455–477.

Giaramita, M.J., and Sorensen, S.S., 1994. Primary fluids in low-temperature eclogites: evidence from two subduction complexes (Dominican Republic, and California, USA). *Contributions to Mineralogy and Petrology*, **117**, 279–292.

Grove, M., and Bebout, G.E., 1995, Cretaceous tectonic evolution of coastal southern California: insights from the Catalina Schist, *Tectonics*, **14**, 1290–1308.

Grove, M., Bebout, G.E., Jacobson, C.E., Barth, A.P., Kimbrough, D.L., King, R.L., Zou, H., Lovera, O.M., Mahoney, B.J., and Gehrels, G.E., 2008, The Catalina Schist: Evidence for middle Cretaceous subduction erosion of southwestern North America, *Geological Society of America Special* Paper, **436**, 335–361.

Grover, T.W., Rice, J.M., and Carey, J.M., 1992. Petrology of aluminous schist in the Boehls Butte region of northern Idaho: Phase equilibria and P-T evolution. *American Journal of Science*, **292**, 474–507.

Howarth, R., 1998. Improved estimators of uncertainty in proportions, point-counting, and pass-fail test reults. *American Journal of Science*, **298**, 594–607.

Keiter, M., Piepjohn, K., Ballhaus, C., Lagos, M., and Bode, M., 2004, Structural development of high-pressure metamorphic rocks on Syros island (Cyclades, Greece), *Journal of Structural Geology*, **26**, 1433–1445.

King, R.L., Bebout, G.E., Grove, M., Moriguti, T., and Nakamura, E., 2007, Boron and lead isotope signatures of subduction-zone mélange formation: Hybridization and fractionation along the slab-mantle interface beneath volcanic arcs, *Chemical Geology*, **239**, 305–322.

Kretz, R., 1983. Symbols of rock-forming minerals. *American Mineralogist, **68**, 277–279.*

Marschall, H.R., Ludwig, T., Altherr, R., Kalt, A., and Tonarini, S., 2006. Syros metasomatic tourmaline: Evidence for very high-δ11B fluids in subduction zones. *Journal of Petrology*, **47**, 1915–1942.

Marschall, H.R. and Schumacher, J.C., 2012. Arc magmas sourced from mélange diapirs in subduction zones. *Nature Geoscience*, **5**, 862–867.

McDonough, W.F. and Sun, S.S., 1995. The Composition of the Earth. *Chemical Geology*, **120**, 223–253.

Meisel and Moser, 2004. Reference materials for geochemical PGE analysis: new analytical data for Ru, Rh, Pd, Os, Ir, Pt and Re by isotope dilution ICP-MS in 11 geological reference materials. *Chemical Geology*, **208**, 319–338.

Miller, D. P., Marschall, H.R., and Schumacher, J.C., 2009, Metasomatic formation and petrology of blueschist-facies hybrid rocks from Syros (Greece), Implications for reactions at the slab-mantle interface, *Lithos*, **107**, 53–67.

Morris, J.D., Ryan, J.G., 2003. Subduction zone processes and implications for changing composition of the upper and lower mantle. In: Carlson, R. (Ed.), Treatise on Geochemistry, 2, The Mantle and Core. Elsevier, New York, 451–470.

Moore, D. E., 1984. Metamorphic history of a high-grade blueschist exotic block from the Franciscan Complex, California. *Journal of Petrology*, **25**, 126–150.

Okrusch, M. and Bröcker, M., 1990. Eclogites associated with high-grade blueschists in the Cyclades archipelago, Greece: a review, *European Journal of Mineralogy*, **2**, 451–478.

Penniston-Dorland, S.,C, Bebout, G.E., Pogge von Strandmann, P., Elliott, T., Sorensen, S.S., 2012a. Lithium and its isotopes as tracers of subduction zone fluids and metasomatic processes: Evidence from the Catalina Schist, California, USA. *Geochimica et Cosmochimica Acta*, **77**, 530–545.

Penniston-Dorland, S.,C, Walker, R.J., Pitcher, L., Sorensen, S.S., 2012b. Mantle–crust interactions in a paleosubduction zone: Evidence from highly siderophile element systematics of eclogite and related rocks. *Earth and Planetary Science Letters*, **319–320**, 295–306.

Penniston-Dorland, S.C., Bebout, G., Gorman, J. K., Piccoli, P., and Walker, R.J., in prep. Reaction rind formation in the Catalina Schist: Evidence from petrology and geochemistry.

Philippon, M., Brun, J.P., and Gueydan, F., 2011. Tectonics of the Syros blueschists (Cyclades, Greece): From subduction to Aegean extension, *Tectonics*, **30**, TC4001.

Plank, T., Langmuir, C.H., 1993. Tracing trace elements from sediment input to volcanic output at subduction zones. *Nature*, **362**, 739–743.

Puchtel, I. S. and Humayun M., 2005. Highly siderophile element geochemistry of 187Os-enriched 2.8 Ga Kostomuksha komatiites, Basaltic Shield. *Geochimica et Cosmochimica Acta*, **69**, 1607–1618.

Rehkämper, M., Halliday, A.N.,1997. Development and application of new ion exchange techniques for the separation of the platinum group and other siderophile elements from geological samples. *Talanta* **44**, 663–672.

Ridley, J., 1984a, Evidence of a temperature-dependent 'blueschist' to 'eclogite' transformation in high-pressure metamorphism of metabasic rocks. *Journal of Petrology*, **25**, 852–870.

Rosenbaum, G., Avigad, D., Sánchez-Gómez, M., 2002, Coaxial flattening at deep levels of orogenic belts: evidence from blueschists and eclogites on Syros and Sifnos (Cyclades, Greece). *Journal of Structural Geology*, **24**, 1451–1462.

Sakai, C., Banno, S., Toriumi, M., and Higashino, T., 1958. Growth history of garnet in politic schists of the Sanbagawa metamorphic terrain in central Shikoku. *Lithos*, **18**, 81–95.

Schulte, R.F., Schilling, M., Anma, R., Farquhar, J., Horan, M.F., Komiya, T., Piccoli, P., Pitcher, L., and Walker, R.J., 2009, Chemical and chronologic complexity in the convecting upper mantle: Evidence from the Taitao ophiolite, southern Chile, *Geochimica et Cosmochimica Acta*, **73**, 5793–5819.

Seck, H.A., Kötz, J., Okrusch, M., Seidel, E., Stosch, H.-G., 1996, Geochemistry of a meta-ophiolite suite: An association of metagabbros, eclogites and glaucophanites on the island of Syros, Greece. *European Journal of Mineralogy*, **8**, 607–623.

Shirey, S.B., and Walker, R.J., 1995. Carius tube digestion for low-blank rhenium-osmium analysis. *Analytical Chemistry*, **67**, 2136–2141.

Shirey, S.B., and Walker, R.J., 1998.The Re-Os isotope system in cosmochemistry and high-temperature geochemisty. *Annual Review of Earth and Planetary Sciences*, **26**, 423–500.

Sorensen, S. S., 1986, Petrologic and geochemical comparison of the blueschist and greenschist units of the Catalina Schist terrane, southern California, *Geological Society of America, Memoir*, **164**, 59–75.

Sorensen, S.S., 1988. Petrology of amphibolite-facies mafic and ultramafic rocks from the Catalina Schist, Southern California; metasomatism and migmatization in a subduction zone metamorphic setting. *Journal of Metamorphic Geology*. **6**, 405–435.

Sorensen, S.S., and Barton, M.D., 1987, Metasomatism and partial melting in a subduction complex: Catalina Schist, southern California, *Geology*, **15**, 115–118.

Sorensen, S.S., and Grossman, J.N., 1989, Enrichment of trace elements in garnet amphibolites from a paleo-subduction zone: Catalina Schist, southern California, *Geochimica et Cosmochimica Acta*, **53**, 3155–3178.

Trotet, F., Vidal, O., and Jolivet, L., 2001, Exhumation of Syros and Sifnos metamorphic rocks (Cyclades, Greece). New constraints on the P-T paths, *European Journal of Mineralogy*, **13**, 901–920.

Tsujimori, A. and Itaya, T., 1999. Blueschist-facies metamorphism during Paleozoic orogeny in southwestern Japan: {hengite K-Ar ages of blueschist-facies tectonic blocks in a serpentinite mélange beneath early Paleozoic Oeyama ophiolite. *Island Arc*, **8**, 190-205.

Volkova, N.I., Frenkel, A.E., Budanov, V.I., Lepezin, G.G. 2004. *Journal of Asian Earth Sciences*. **23** 745-759.

Widom, E., Kepezhinskas, P., Defant, M., 2003. The nature of metasomatism in the subarc mantle wedge: evidence from Re-Os isotopes in Kamchatka peridotite xenoliths. *Chemical Geology*, **196**, 283–306.

Wijbrans, J.R., Schliestedt, M., York, D. 1990. Single grain argon laserprobe dating of phengites from the blueschist to greenschist transition on Sifnos (Cyclades, Greece). *Contributions to Mineralogy and Petrology*, **104**, 582–593.

Xiong, Y. and Wood, S.A., 2000. Experimental quantification of hydrothermal solubility of platinum-group elements with special reference to porphyry copper environments. *Mineralogy and Petrology*, **68**, 1-28.

Zack T; Moraes R; Kronz A., 2004, Temperature dependence of Zr in rutile: empirical calibration of a rutile thermometer, *Mineralogy and Petrology*, **148**, 471–488.